Resonance fluorescence of self-assembled quantum dots

Ted Silva Santana

Thesis submitted for the degree of Doctor of Philosophy

Heriot-Watt University
School of Engineering and Physical Sciences
Institute of Photonics and Quantum Sciences

August of 2016

Abstract

Resonance fluorescence from solid state devices have been motivated by the capability to obtain a bright source of antibunched and indistinguishable photons from a semiconductor chip. Such a photon source would be a strong candidate for applications in the quantum information field. In this thesis, an experimental setup to obtain high signal to noise resonance fluorescence from a single quantum dot is first presented. I then discuss the photon statistics, power spectrum, second-order correlation function and two-photon interference of the stream of resonance fluorescence. Particular emphasis is placed on a throughout investigation of spectral fluctuations caused by charge noise and Overhauser field generated by fluctuating nuclear spins in the quantum dot. In each case, it is found that noise can be overcome to generate single photons that exhibit high visibility two-photon interference. Finally, an interference effect caused by the interaction of a quantum dot and a nearby metal surface is presented. Preliminary analysis yields quantitative agreement with the data.

Keywords: resonance fluorescence, quantum dot, spectral fluctuations

In memoriam Rafael Matos Santos

Acknowledgement

I would like to dedicate this thesis to my parents, brothers, my wife Daianne Santana, my daughter Sofia de Oliveira Santana and to my many other members of my family who, with a lot of affection, supported me to reach this stage of my life. To Professor Brian D. Gerardot for supporting my professional development which allowed me to perform this work. To all member of the Quantum Photonics Laboratory for their friendship, offering a good work environment. To all staff in the School of the Engineering and Physical Sciences at the Heriot-Watt University for the constant support.

ACADEMIC REGISTRY
Research Thesis Submission

Name*:*	Ted Silva Santana		
School/PGI:	School of Engineering and Physical Sciences		
Version: *(i.e. First, Resubmission, Final)*		Degree Sought (Award **and** Subject area)	Doctor of Philosophy

Declaration

In accordance with the appropriate regulations I hereby submit my thesis and I declare that:

1) the thesis embodies the results of my own work and has been composed by myself
2) where appropriate, I have made acknowledgement of the work of others and have made reference to work carried out in collaboration with other persons
3) the thesis is the correct version of the thesis for submission and is the same version as any electronic versions submitted*.
4) my thesis for the award referred to, deposited in the Heriot-Watt University Library, should be made available for loan or photocopying and be available via the Institutional Repository, subject to such conditions as the Librarian may require
5) I understand that as a student of the University I am required to abide by the Regulations of the University and to conform to its discipline.

* *Please note that it is the responsibility of the candidate to ensure that the correct version of the thesis is submitted.*

Signature of Candidate*:*		Date:	

Submission

Submitted By *(name in capitals):*	
Signature of Individual Submitting:	
Date Submitted:	

For Completion in the Student Service Centre (SSC)

Received in the SSC by *(name in capitals):*			
Method of Submission *(Handed in to SSC; posted through internal/external mail):*			
*E-thesis Submitted (**mandatory for final theses)***			
Signature:		Date:	

Contents

List of Figures

Chapter 1

Introduction

Nowadays, most information processing is based on the charge flux in electronic devices. In the search for alternatives, the principles of quantum mechanics have been exploited to propose new ways to process information. Here, the classical bits (basic information unit) would be replaced by two states of a quantum system. These would be called quantum bits or qubits. The main advantage of the qubits over the classical bits is that information can be stored in a superposition of the two quantum states instead of only one of the states as in classical information processing. However, the most interesting situation happens when two qubits interact with each other and the quantum state of the system can be anyone describing the mixture of the two qubits. Some quantum algorithms have demonstrated that this feature could be used to accelerate the processing rate of some information tasks [1, 2]. One example is the factorisation of a large number, which takes a long time to perform with today's computers and for this reason is the basis for information encryption. This has motivated research and proposals in which quantum systems would be ideal. Among these proposals, the most promising is the seminal work of Loss and DiVincenzo [3], who proposed to use the spin degree of freedom in semiconductor quantum dots, whose decoherence time is relatively large, allowing many manipulations before the information deterioration. Fortunately, such a system can interact with light, making optics based systems interesting for this purpose.

A quantum dot (QD) is a nanometric region shaped like an island and composed of a semiconductor embedded in another semiconductor of larger band gap. They exhibit characteristics in both transport and optical spectroscopy which indicate that the charge carriers are confined in the three dimensions. Electrons and holes (lack of an electron in the valence band) in QDs can occupy only a specific set of states with discrete energy levels, as an atom. Because of these similarities, the QDs are also called artificial atoms [4, 5], and

in principal allow experiments similar to ones performed in atomic physics but in a fully controlled solid state environment.

In this work a single QD transition is studied using the resonance fluorescence technique [6], which relies on the resonant excitation of the optical transition. This yields a main experimental obstacle: the distinction between the light emitted by the QD and the laser light reflected by the sample surface. In the next chapter, the experimental setup will be fully described, including the self-assembled QD samples and the dark-field microscope used to achieve high signal to noise resonance fluorescence (RF) signal. The steps towards the optimal version of the microscope is also discussed, as well as the non-resonant photoluminescence technique used to find the QDs both spectrally and spatially, and the measurement of the Stark coefficient, which quantifies the dependence of the energy shift of the QD transition on the bias voltage applied to the device, using resonance fluorescence.

The third chapter is dedicated to the analysis of the two-level system (TLS), which is a good approximation for the neutral exciton (X^0) and negatively charged exciton (X^{1-}) transitions of the QD in the absence of magnetic field. Here I present the photon statistics, power spectrum of the QD emission, second-order correlation function and the Hong-Ou-Mandel (HOM) interference under weak, moderate and strong charge noise regimes. Charge noise is a consequence of the interaction between the charge carriers in the QD and the time-dependent charge density in the QD environment.

In the fourth chapter, the optical properties of the four-level system formed by the X^{1-} transition under an external magnetic field in the Faraday geometry are investigated, as well as the consequences of the random magnetic field resulted from the set nuclear spin (Overhauser field) on the power spectrum and second-order correlation of the QD emission.

The fifth chapter is dedicated to the discussion of the interaction between the QD and the gold mirror of the planar-cavity antenna (PCA) samples. It starts from the discussion of the experimental results, then, preliminary analysis is presented.

Chapter 2

Experimental methods

In this chapter, I will present the experimental techniques used to perform the research in this thesis. First, I will describe the overall experimental setup that enables ultra-stable RF of a single QD for an unlimited time. I will then describe the dark-field microscope used to obtain RF with the scattered laser light suppressed by a factor greater than 10^7. This enables very high (> 1000) signal to background ratios. Next, I will present the analytical components: the spectrometer, Fabry-Perot interferometer (FPI), Hanbury Brown and Twiss (HBT), and HOM interferometers as well as the timing electronics. Finally, I will describe the charge-tunable QD sample designs [7]. These samples were grown by the application of the molecular beam epitaxy technique [5, 8, 9, 10, 11]. Three samples were investigated during the course of this thesis, which are refereed to as: 1) the bulk sample, 2) the 'noisy' planar cavity antenna (PCA) sample, and 3) the 'clean' PCA sample. The PCA provides an increased collection efficiency, ~ 10 times greater than the bulk sample [12]. Sample 1 was grown by Prof. Gerardot in Prof. Petroff's lab at University of California, Santa Barbara. Sample 2 was grown in the University of Sheffield by Dr. Edmund Clarke's group and Sample 3 in the Korea Institute of of Science and Technology by Dr. Song's group. The PCA processing and fabrication was performed by Yong Ma in Prof. Gerardot's lab at Heriot-Watt University. The main contribution of the author for the experimental setup was the construction of the microscope head placed on the cryostat [Fig. 2.1].

The dark-field confocal microscope relies on the polarisation of the light emitted by the QD in order to suppress the reasonable amount of light reflected by the GaAs sample surface [6, 13] by a factor greater than 10^7.

Experimental setup

Collecting resonantly scattered photons from a single quantum dot is an important step towards the use of QDs for quantum network with applications in quantum communication [14] and for spin-based qubit initialisation, manipulation and read-out [15, 16, 17, 18]. The challenge for the experimental realisation is to distinguish between the photons scattered from the QD and the photons reflected from the sample surface, since they have the same energy. In this work, we exploit the polarisation to differentiate photons from these two different sources.

The complete experimental setup is described in this section, starting from the primary source of photons until the detector, which is the final destination of the resonantly scattered photons, following the optical path [Fig. 2.1].

On an optical table, 50% of the excitation laser beam from a tunable diode laser is coupled into a single-mode fibre (SMF) using an aspheric lens of numerical aperture (NA) equal to 0.15 and focal distance equal to 18.40 mm and sent to a wavemeter, where its wavelength is recorded and stabilised through a proportional-integral-derivative (PID) system in the laser controller. The other 50% of the light interacts with a continuously variable neutral density (ND) filter wheel for power calibration and with a quarter-wave plate (QWP) and a half-wave plate (HWP) for polarisation control in free-space. This is then coupled into a SMF by another aspheric lens of NA equal to 0.15. The laser is coupled into the single-mode fibre by adjusting its position using a xy translation mount (Thorlabs/ST1XY-D) and all the lenses in the microscope were mounted in a z-axis translation mount (Thorlabs/SM1Z) in order to place it in an optimum position. The details of all the parts used in the microscope can be found in [Appendix A]. The fibre takes the laser signal to the excitation arm of the microscope head placed on a cryostat platform. In the excitation arm, the light is collimated and passed through a linear polariser (LP). The linearly polarised light is reflected to the sample by a 5 mm thick and uncoated glass plate (TUGP) beam splitter with reflectance of $\sim 4\%$ per surface. This downward travelling beam is transmitted through an anti-reflection (AR) coated optical window. The power of the radiation transmitted by the beam splitter is measured by a photodiode (PD). Before reaching the sample, the light is focused by another aspheric lens with NA equal to 0.68 and focal distance equal to 2.75 mm [Fig. 2.1]. The sample is placed on an xy-scanner, which is on the top of a stack of nano drives which gives the freedom to move the sample in three dimensions. The optical

window is the interface between the microscope head, used for excitation and collection, and the sample tube, which is evacuated and then filled with 20 mbar of He gas.

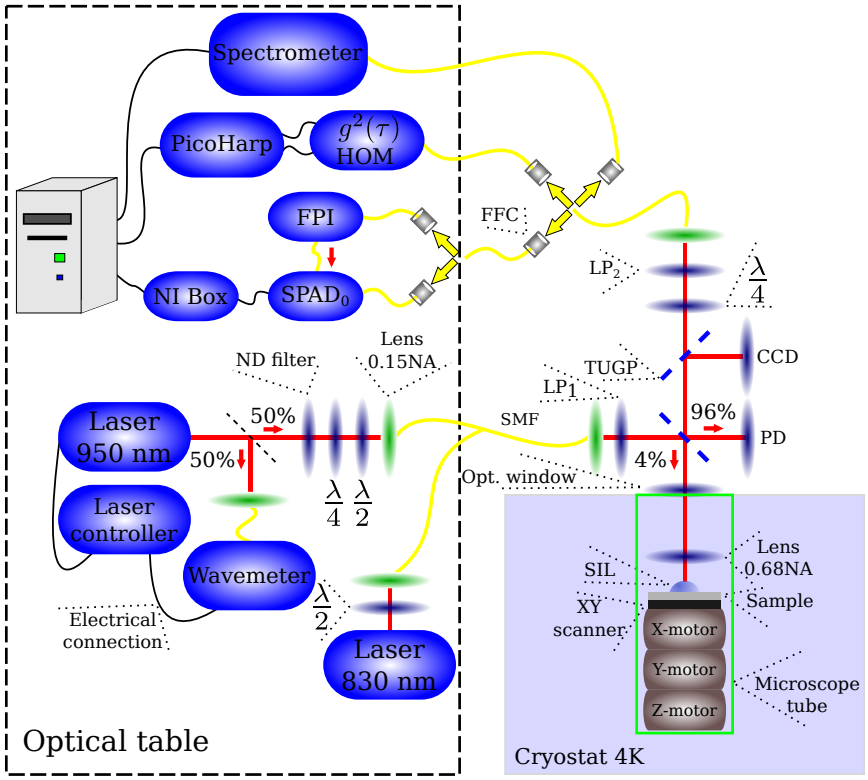

Figure 2.1: **Sketch of the experimental setup**. On an optical table, 50% of the excitation laser beam from a 950 nm laser is coupled into a SMF using an aspheric lens and sent to a wavemeter, where its wavelength is recorded and stabilised through a PID system in the laser controller. The other 50% of the light interacts with a ND filter wheel for power calibration and with a QWP and a HWP for polarisation control in free-space. This is then coupled into a SMF by another lens, which takes the laser signal to the excitation arm of the microscope head placed on a cryostat platform. In the excitation arm, the light is collimated, passed through a LP and reflected to the sample by a TUGP beam splitter. This downward travelling beam is transmitted through an AR coated optical window and starts travelling inside the sample tube. The power of the radiation transmitted by the beam splitter is measured by a PD. Before reaching the sample, the light is focused by another aspheric lens. The sample is placed on an xy-scanner, which is on the top of a stack of nano drives which gives the freedom to move the sample in three dimensions. For non-resonant photoluminescence experiments, a second diode laser with wavelength of about 830 nm was also coupled into the system.

To be able to perform non-resonant photoluminescence experiments, a second diode laser with wavelength of about 830 nm was also coupled into the system. The output beam from this laser interacts with a HWP and then is coupled into a SMF, from where it follows the same path as the resonant laser beam until reaching the first mating sleeve (FFC) taking the signal and remaining background to the spectrometer. The results of this experiment is presented in [Sec. 2.3].

The circularly (linearly) polarised light emitted by the negatively-charged X^{1-} (neutral exciton X^0) transition of the QDs in the sample and some amount of reflected laser - which will be called background light from now on - are collected by the same lens used to focus the excitation laser beam to the sample [6, 13]. The QDs signal and the background light are $\sim 96\%$ transmitted by each surface of two glass-plate beam splitters and the signal reflected by the second (upper) beam splitter is captured by a charge-coupled device (CCD) image sensor for alignment purposes. After crossing both beam splitters the signal and background light reach the collection arm and interact with a QWP in order to correct for any distortion that the linearly polarised excitation laser beam suffered by interacting with these optical elements. The scattered laser light is the suppressed by another LP (LP2) set to be orthogonal to LP1 in the excitation arm. Just after LP2 the light is coupled into another single-mode fibre, which is also very important for the background suppression because of the spatial mode of the background light, described as the "Maltese cross", which is originated from the interaction between the excitation laser with the curved surface of the lens with high NA [19]. While the background light is suppressed by the a factor $> 10^7$, the signal from the QDs is suppressed only by a factor of two because of its circular polarisation (X^{1-} case) or linear polarisation rotated by 45 degrees if the transition is X^0. After the background suppression, the signal and any remaining amount of background light is sent to the spectrometer, single-photon avalanche diode (SPAD), FPI, HOM interferometer for two-photon interference or HBT interferometer for $g^2(\tau)$, depending on the kind of measurement desired [Fig. 2.1].

Beam splitter analysis

Before reaching the final and optimal version of the microscope described above, some beam splitters were checked in order to find the best optical element for background light suppression. The best three elements were a polarising beam splitter cube (PBSC), a long pass beam splitter (LPBS) and a thick uncoated glass plate (TUGP). The configuration LP/QWP/LP was also checked just for comparison with the other elements.

The input laser (top arrow in [Fig. 2.2]) interacts with a LP adjusted to give maximal suppression and with a QWP to correct for any distortion in the linear polarisation before reaching the PBSC (left side in [Fig. 2.2]) or the second LP (right side in [Fig. 2.2]) in the case of a non-polarising beam splitter. The output from the PBSC or LP is monitored by a CCD camera and the suppressed radiation is shown in [Fig. 2.3].

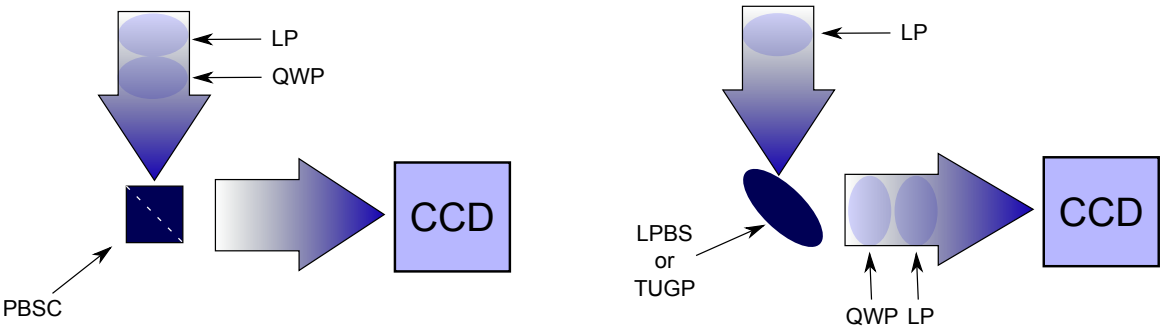

Figure 2.2: **Configuration of the optical elements to check the background light suppression.** The light from the LP interacts with a QWP to correct any polarisation distortion caused by the interaction of the light with the optical elements before it reaches beam splitter. The light is then suppressed by the PBSC (left) or a second LP (right) and the resulting radiation is monitored by a CCD camera.

As it is noticeable in [Fig. 2.3], the PBSC tested was found to be very efficient in one region of the reflected spot. However, the rest of the spot showed poor cancellation due to wavefront distortion across the face of the beam splitter. By adjusting the QWP to correct for wavefront distortion at a different portion of the PBSC, the regions of good or poor cancellation could be interchanged. The maximum extinction ratio observed with this optical element was $\sim 10^4$. A Similar result is observed for the LPBS, but it is better than the PBSC in the marginal regions of the laser beam. So, the beam splitter for the background suppression was the TUGP, which allowed an almost uniform and very efficient suppression of the linearly polarised laser giving an extinction ratio $> 10^7$, which is comparable to what we observed for the LP/QWP/LP configuration (without any optical element) [Fig. 2.3 - fourth panel].

For the LP/QWP/LP, different from what is depicted in [Fig. 2.2], was measured with the laser input, optical elements and output to CCD in the same line.

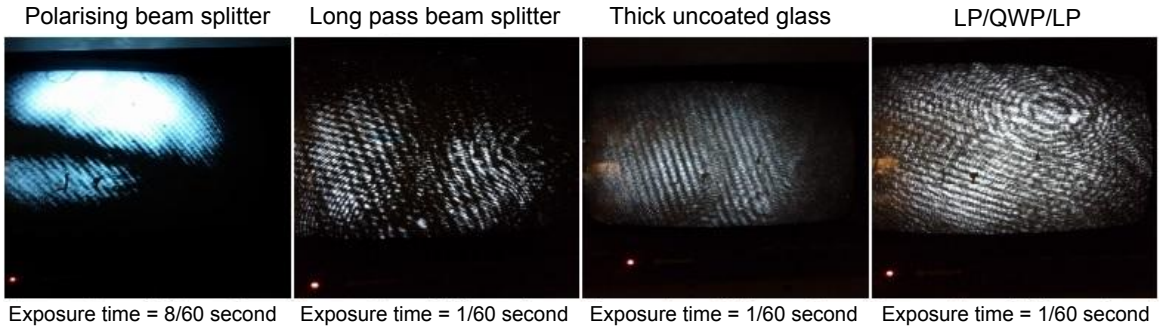

Figure 2.3: **Background light suppression.** Linearly polarised laser suppression for different beam splitters (PBSC, LPBS, TUGP) and without a beam splitter (on the right side) monitored with a sensitive CCD camera.

Charge-tunable quantum dot samples

The possibility of controlling the number of electrons in nano-structures using an external bias voltage gave rise to the chance of experimental investigation of Coulomb interaction in devices where the contribution of the confinement energy to the total energy of the system is small [20, 21, 22] and comparable or greater [23, 24, 25, 26, 27]. The high precision control on the number of electrons trapped in the nano-structure also enabled the study of spin dynamics, which is a natural candidate for a unit of quantum information [15, 16, 17, 18, 28, 29].

When the applied voltage is large and negative, the level structure of the QD is far from resonance with the Fermi sea and the QD remains empty. As the voltage is moved to positive, the QD gets closer to resonance with the Fermi sea and the probability of one electron to tunnel into the QD also increases. On resonance, with one electron trapped into the QD, the energy of the QD changes and the second electron needs a higher voltage to tunnel into the QD to compensate the energy of the first electron trapped [Fig. 2.4].

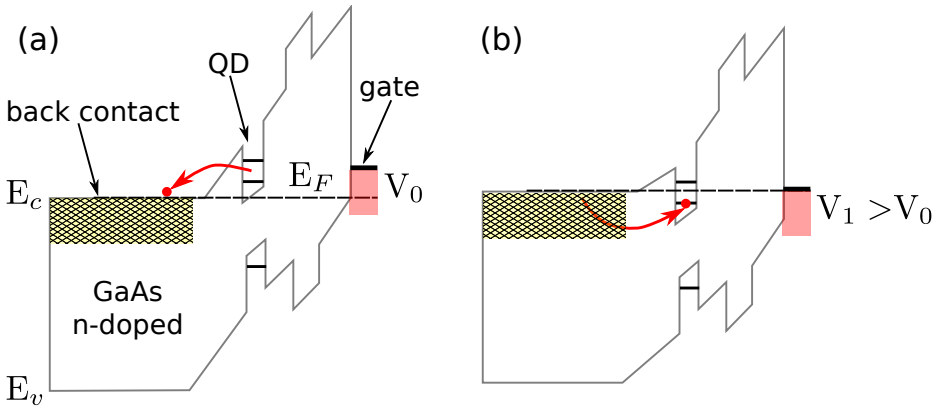

Figure 2.4: **Energy diagram of a charge-tunable QD.** The detuning between the QD energy and the Fermi sea (E_F) can be controlled through the gate voltage (V_0), and if they are far (close) from resonance, the probability of the electron to tunnel into the QD is small (big), as can be observed in (a) and (b), respectively.

Bulk sample

The charge-tunable quantum dot sample named "bulk sample" or simply Sample 1 in this work is composed by a GaAs buffer, an n-doped back contact, a GaAs tunnel barrier, an InAs QD layer covered by a capping layer, a superlattice and a Schottky gate which is a semitransparent layer of NiCr on the top surface of the sample [Fig. 2.5]. The details of the thickness of the layers can be checked in [Tab. 2.1]. The back-contact is an Ohmic contact to a heavily Si doped ($n^+ = 4 \times 10^{18}$ cm^{-3}) layer. The Ohmic contact is achieved

by diffusing a small amount of In from the sample surface supplying an Ohmic contact with resistance of about 1 kΩ [7]. The probability of the electron to tunnel through the tunnel barrier to a QD depends directly on the energy difference between the Fermi energy for the back contact and the level energy to be occupied in the QD. The energy levels of the QD can be changed by applying a voltage between the Schottky gate and the back contact, exploring the confined Stark effect [30]. The superlattice prevents current flow through the device. A glass hemispherical solid-immersion lens (SIL) is attached on top of the sample to increase the effective NA [31, 32, 33, 34, 35, 36, 37] [Fig. 2.5].

layer	size (nm)	material
buffer	80	GaAs
back contact	20	n^+ GaAs
tunnel barrier	25	GaAs
QDs		InAs
capping layer	30	GaAs
blocking barrier	20×(3/2)	(AlAs/GaAs)
cap	6.3	GaAs

Table 2.1: **Description of the layers composing the bulk sample.**

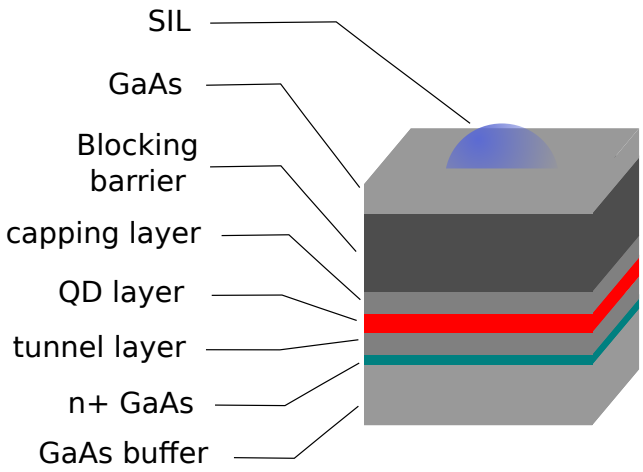

Figure 2.5: **Bulk sample structure.** The bulk sample is composed by (bottom to up): GaAs buffer layer, n-doped GaAs layer, GaAs tunnel barrier, InAs QD layer, GaAs capping layer, AlAs/GaAs blocking barrier, GaAs cap and the Si SIL.

Planar cavity antenna sample

The main difference between the PCA sample and the bulk sample is in the collection efficiency. Finite-difference time-domain (FDTD) simulations performed by Dr. Yong Ma [Fig. 2.7] showed that the estimated collection efficiency for the PCA sample is $\sim$ 27%, while it is only $\sim$ 2% for the bulk sample for an objective lens of NA equal to 0.68 [12].

The planar cavity antenna (PCA) samples are fabricated from a bulk sample and consist of a quantum dot layer embedded at the antinode of a low-Q, broadband cavity formed by a Au mirror and the GaAs/SIL interface. Although the optical properties of the device are modified compared to the bulk sample, the electronic device is identical to the bulk sample and the same deterministic state charging is achieved.

The fabrication process consists of depositing and annealing AuGeNi in order to make the ohmic contacts with the n-doped layer, depositing a gold layer which will act as a mirror and Schottky contact, flipping it on a host surface containing epoxy glue and wet etching the GaAs substrate and the $Al_{0.65}Ga_{0.35}As$ layer. Then the Au layer is made accessible by photolithography and wet etching [12] [Fig. 2.6].

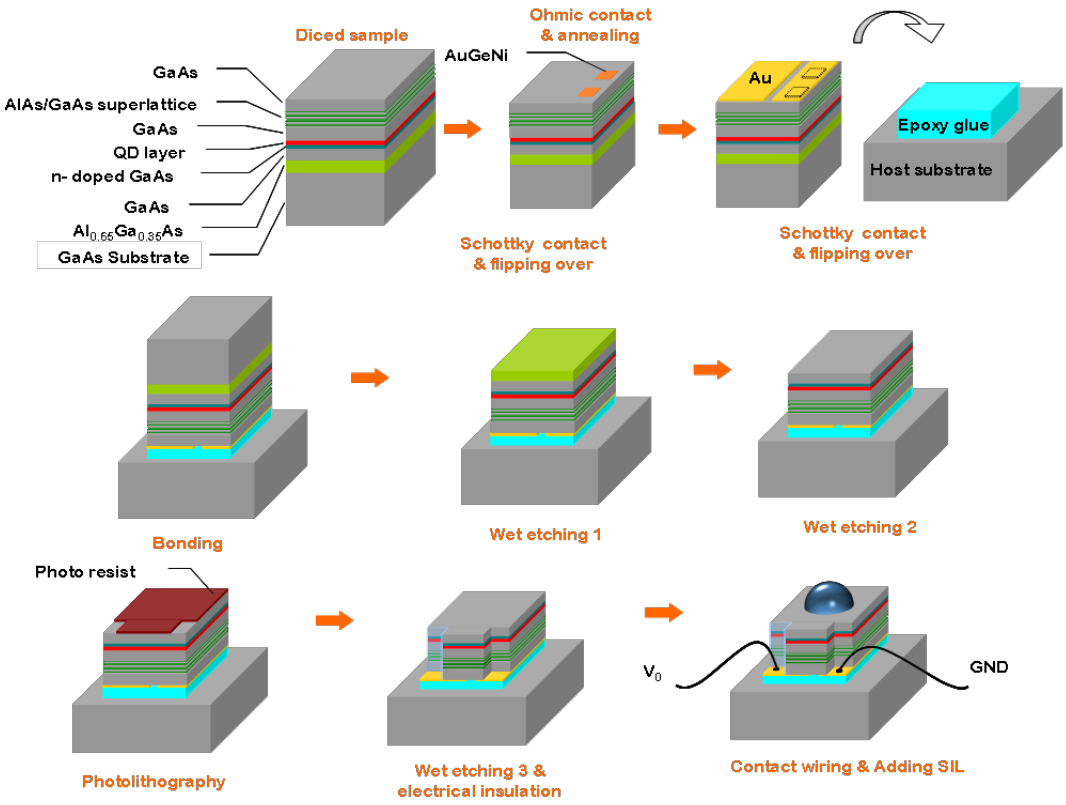

Figure 2.6: **Fabrication steps from bulk sample to PCA sample (figure supplied by Dr. Yong Ma).** From the diced sample, the fabrication steps are (a) deposit 100 nm of AuGeNi and anneal the sample at 400°C to create an ohmic contact with the n-doped layer; (b) deposit 150 nm Au layer as Schottky contact and back reflecting mirror, leaving a 500 μm insulation gap between the ohmic contact and Schottky contact; (c) flip the sample and transfer it to a host substrate using an epoxy glue and compression; (d) selectively etch the bonded sample to remove GaAs substrate and AlGaAs sacrificial layer of the QD sample in sequence; (e) selectively etch the access areas for both contacts wiring; (f) wire both contacts using silver paint.

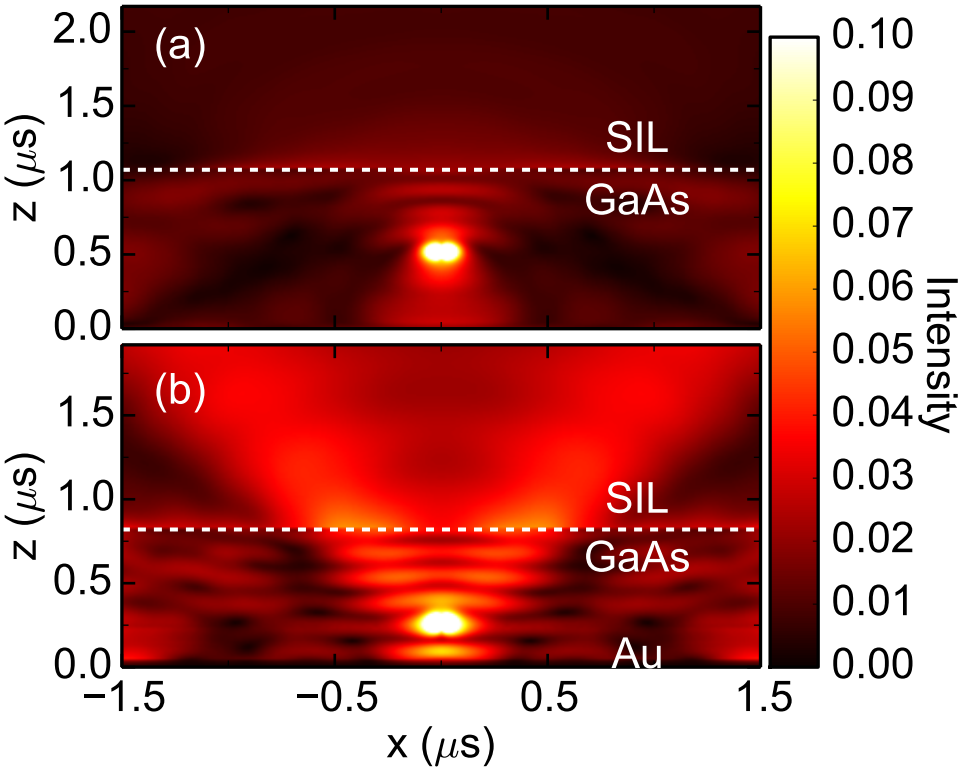

Figure 2.7: **FDTD simulations (figure supplied by Dr. Yong Ma).** FDTD simulation of the electric field distribution for a QD embedded in (a) bulk GaAs for emission wavelength of 937 nm (b) GaAs membrane with Au back reflector for emission wavelength of 937 nm using geometric parameters from the optimized structure of our design.

Photoluminescence

Photoluminescence (PL) is the emission of light by matter after the absorption of higher energy light. Using a laser with an energy larger than the band-gap, electrons and holes relax into the QD via a non-radiative process and then recombine in a radiative process.

In this experiment, the excitation was performed by using a diode laser with λ equal to 830 nm and the light emitted by the QDs, with λ usually between 920 nm and 980 nm, were collected by the collection arm of the microscope and sent to a spectrometer [Appendix A] through an optical fibre. The PL acquired as a function of the bias voltage makes clear the change in the energy of the optical transition due to the presence of electron(s) in the QD [Fig. 2.8].

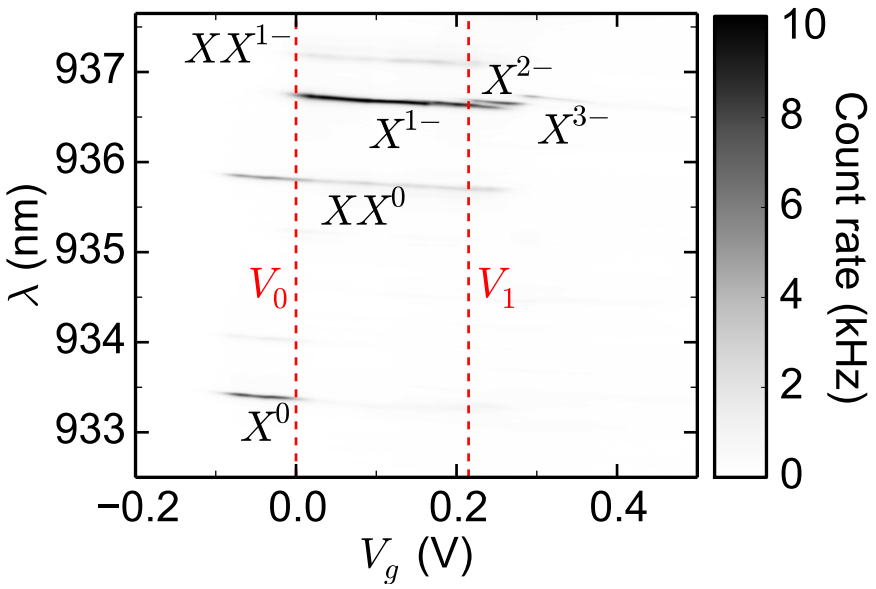

Figure 2.8: **Photoluminescence map of a charge-tunable device.** The number of Xs in the symbol indicates how many electron-hole pairs are involved in the optical transition and the index on the top of X indicates the number of electrons in the initial state. The two gate voltages $V_0 = 0$ V and $V_1 = 0.215$ V are about the voltages for the transitions from X^0 to X^{1-} and from X^{1-} to X^{2-}, respectively.

In this work, a PL map measurement always precedes the experiments based on the resonance fluorescence because it helps to choose a spectrally isolated and bright QD and most importantly, it indicates the wavelength range and the bias voltage range of each optical transition that can be excited resonantly.

Stark coefficient measurement

Before starting the photon statistics measurements we need to obtain the Stark coefficient, which indicates what is the energy shift for a given ΔV_g. The Stark coefficient can be extracted from a set of detuning spectra along the plateau of the QD transition, in this case the X^{1-} transition [Fig. 2.8].

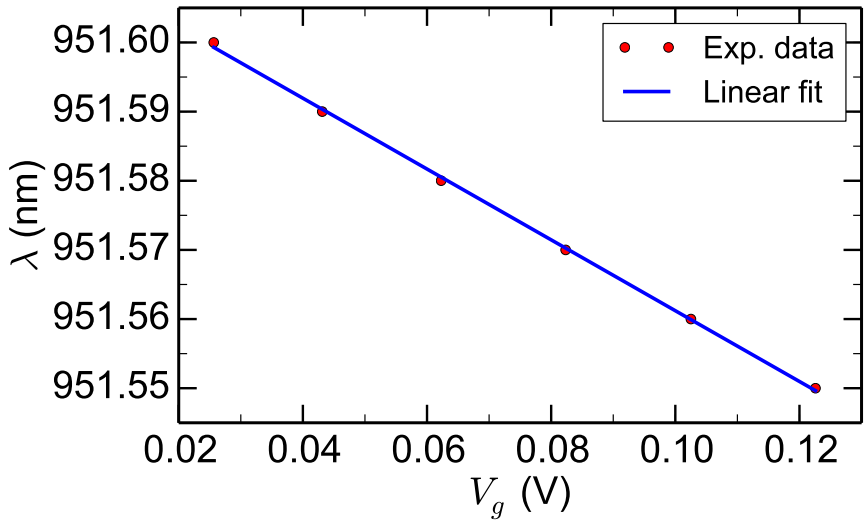

Figure 2.9: **Linear dependence of the resonant laser wavelength on the bias voltage.** The red dots correspond to experimental data and the blue solid line is a linear function fit. From the fit we extracted a Stark coefficient equal to 701.28 μeV/V.

The detuning spectra is measured by setting the wavelength constant somewhere on the plateau and then sweeping the bias voltage with a resolution of 1 mV. Consequently, this sweeps the transition energy of the QD across the resonance of the driving field. The photon count rate is recorded using a SPAD. The resonant bias voltage corresponds to the position of the Lorentzian curve. By acquiring detuning spectra for different laser wavelengths we can track the dependence of the transition energy on the bias voltage, which is a direct measurement of the Stark coefficient [Fig. 2.9].

Second-order correlation function: setup scheme

For the second-order correlation measurement, the background-free RF signal from the collection arm is coupled into the input of a $50\% - 50\%$ fibre splitter, which has the two outputs connected to two SPADs with dead time ~ 24 ns, timing resolution ~ 0.5 ns and dark counts ~ 30 Hz [Appendix A]. When these SPADs are clicked, they send electrical signals to the channels of a time-correlated single photon counting (TCSPC) module supplied by PicoQuant [Appendix A], where it is connected through Bayonet Neill–Concelman (BNC) connectors [Fig. 2.10].

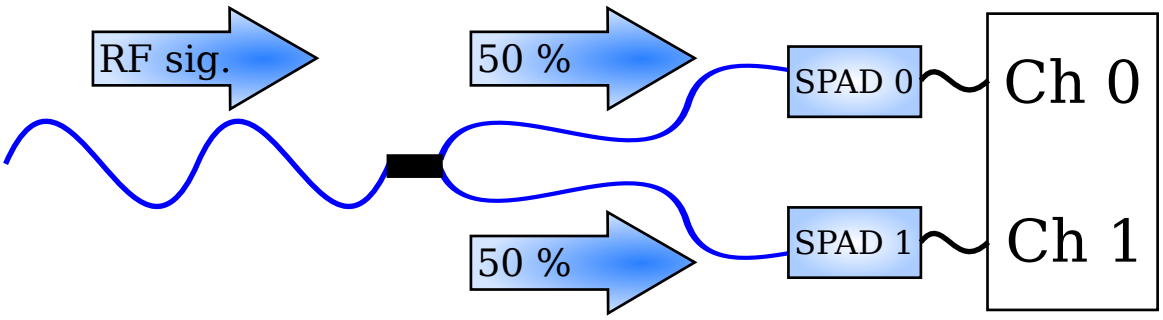

Figure 2.10: **Equipment scheme for the $g^{(2)}(\tau)$ measurement.** The background-free RF signal from the collection arm is coupled into the input of the $50\% - 50\%$ fibre splitter. The outputs are connected to detectors, that send electrical pulses to the channels of a TCSPC. The TCSPC computes the delay time of signals between the two channels and send this data to a computer which calculates a histogram of the delay time, corresponding to the second-order correlation function.

To compute the intensity correlation between the two outputs, the first channel triggers a clock and the second channel stops the clock and then one value of τ is obtained. This process is repeated many times and a histogram, corresponding to the second-order correlation function, is generated.

Two-photon interference: setup scheme

In this section, the experimental setup used to measure the two-photon interference is described departing from the optical fibre of the collection arm [Fig. 2.1].

The RF signal from the single QD is separated using a $50\% - 50\%$ single-mode fibre splitter and reaches the two inputs of the HOM setup. One manual fibre polarisation controller (MFPC) [Appendix A] in each path is used to individually tune the polarisation orthogonal or parallel to each other using the intensity of the signal through a linear polariser as reference (red path in [Fig. 2.11]). In one of the paths, there is an optical delay $\Delta\tau$ which was implemented using a long optical fibre. The two paths end in a $50\% - 50\%$ beam splitter coupled to the SMF, where the HOM interference happens [Sec. 3.5]. After the beam splitter, the photons are driven to the SPADs, which have their electrical output signals taken to TCSPC channels, as in the second-order correlation measurement [Sec. 2.5]. Before the second channel of the TCSPC module an electrical delay τ_c is introduced to move the dips away from zero [Fig. 2.11].

Once the signal reaches the TCSPC, it builds a histogram of the delay between the arrival times of the photons in each channel, again, similar to the second-order correlation measurement [Sec. 2.5].

Two other dips are also expected at $\tau_c \pm \Delta\tau$ along with the HOM dip due to the optical delay between the two paths. The depth of these dips should be identical for a balanced beam splitter [38, 39].

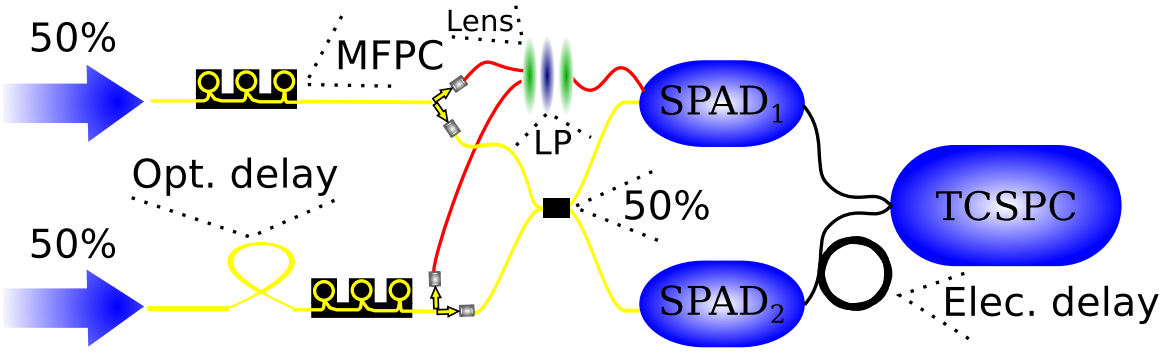

Figure 2.11: **HOM setup.** The separated RF signal reaches the two inputs of the HOM setup. In one of the paths, there is a MFPC used to tune the polarisation orthogonal or parallel to the second path, where an optical delay was implemented using a long optical fibre. The two paths end in a 50% beam splitter coupled to the SMF, where the HOM interference happens. After the 50% beam splitter the photons are driven to the SPADs, which have their electrical output signals taken to the TCSPC module. Before the second channel of the TCSPC an electrical delay is introduced to move the dips away from zero. Two other dips are expected due to the optical delay between the two paths to the beam splitter, with their relative depth depending on the balance of the beam splitter.

Chapter 3

The standard two-level system

The two-level system is the canonical example of a quantum bit and many realizations have been experimentally explored, including spin-based systems [40, 41], nuclear magnetic resonance (NMR) [42, 43] and in quantum optics [44, 45, 46]. The systems in quantum optics experiments typically have more than two states, but the experimental results can still be explained using the semi-classical formulation of the optical Bloch equations [47] by exploiting the selection rules or neglecting an excited transition that is well detuned from other states.

In this chapter, the photon counting statistics, based on the optical Bloch equations, the power spectrum and the second-order correlation of the resonance fluorescence photons will be discussed, along with the effects of spectral fluctuations on the photon emission.

Photon counting statistics

We consider a two-level system composed of the ground state $|g\rangle$ and the excited state $|e\rangle$ coupled by a near resonance electromagnetic (EM) driving field with power low enough that the rotating-wave approximation is valid [48], and the Hamiltonian is given by

$$H = -\frac{\Delta}{2}\sigma_z + \frac{\Omega}{2}(\sigma_- + \sigma_+) \,, \tag{3.1}$$

where Δ is the detuning between the driving field and the transition, Ω is the Rabi energy, σ_z is the Pauli Matrix defined as $|g\rangle\langle g| - |e\rangle\langle e|$, $\sigma_- = |g\rangle\langle e|$, and $\sigma_+ = |e\rangle\langle g|$.

The Rabi energy can be interpreted as the coupling energy between the optical transition and the EM driving field. It relates to the experiment through the excitation power, which is proportional to $|\Omega|^2$.

Using the Lindblad superoperator to describe the radiative decay from the excited state

to the ground state and the pure dephasing we have

$$L\rho(\sigma_-) = \frac{\Gamma}{2}\left(2\sigma_-\rho\sigma_+ - \sigma_+\sigma_-\rho - \rho\sigma_+\sigma_-\right) \tag{3.2}$$

$$L\rho(\sigma_z) = \frac{\gamma}{2}\left(\sigma_z\rho\sigma_z - \rho\right) , \tag{3.3}$$

where Γ is the radiative decay rate and γ is the exciton pure dephasing rate.

Then, we have that the master equation is

$$\dot{\rho} = -\frac{i}{\hbar}[H,\rho] + L\rho(\sigma_-) + L\rho(\sigma_z) , \tag{3.4}$$

leading to the optical Bloch equations

$$\dot{\rho}_{gg} = \frac{\Omega}{\hbar}\mathrm{Im}[\rho_{eg}] + \Gamma\rho_{ee} \tag{3.5}$$

$$\dot{\rho}_{ee} = -\frac{\Omega}{\hbar}\mathrm{Im}[\rho_{eg}] - \Gamma\rho_{ee} \tag{3.6}$$

$$\dot{\rho}_{ge} = \frac{i}{\hbar}[\Delta\rho_{ge} - \frac{\Omega}{2}\left(\rho_{ee} - \rho_{gg}\right)] - \left(\frac{\Gamma}{2} + \gamma\right)\rho_{ge} \tag{3.7}$$

$$\dot{\rho}_{eg} = -\frac{i}{\hbar}[\Delta\rho_{eg} - \frac{\Omega}{2}\left(\rho_{ee} - \rho_{gg}\right)] - \left(\frac{\Gamma}{2} + \gamma\right)\rho_{eg} . \tag{3.8}$$

The steady state solution can be obtained by making the density matrix constant, i.e, $\dot{\rho} = 0$, from where we get

$$\rho_{ee} = \frac{\Omega^2\phi}{2\Gamma(\Delta^2 + \phi\Omega^2/\Gamma + \hbar^2\phi^2)} \tag{3.9}$$

$$\rho_{gg} = 1 - \rho_{ee} \tag{3.10}$$

$$\rho_{ge} = \frac{-\Omega(\Delta - i\hbar\phi)}{2(\Delta^2 + \phi\Omega^2/\Gamma + \hbar^2\phi^2)} \tag{3.11}$$

$$\rho_{eg} = \rho_{ge}^* , \tag{3.12}$$

where $\phi = \Gamma/2 + \gamma$.

The average number of photons $\langle n\rangle$ is given by the multiplication of the probability of being in the excited state ρ_{ee}, the radiative decay rate Γ and the detection efficiency η, so

$$\langle n\rangle = \frac{\eta\Omega^2\phi}{2(\Delta^2 + \phi\Omega^2/\Gamma + \hbar^2\phi^2)} . \tag{3.13}$$

If the driving field is on resonance with the QD transition energy, the expected number of photons is

$$\langle n\rangle = \frac{\eta\Gamma}{2}\frac{\Omega^2}{(\Omega^2 + \Omega_{sat}^2)} , \tag{3.14}$$

where Ω_{sat} is the saturation Rabi energy [49] defined as

$$\Omega_{sat} = \hbar\sqrt{\phi\Gamma} . \tag{3.15}$$

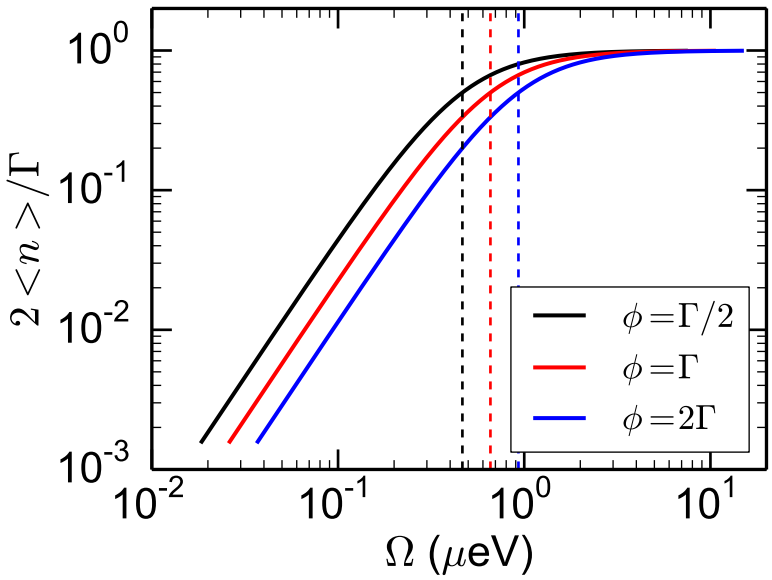

Figure 3.1: **Saturation curve.** Normalized number of photons scattered as a function of Rabi energy with decay rate equal to 1 GHz, $\Delta = 0$ and perfect detection. The vertical lines represents the saturation Rabi energy for each dephasing rate.

The saturation curves for different dephasing rates are shown in [Fig. 3.1].

From [Eq. 3.13] we have that the width of the Lorentzian peak as a function of detuning Δ, which we will call detuning spectrum from now on, depends on the Rabi energy Ω, becoming broader as Ω increases. This phenomenon is known as power broadening [50]. The width of the Lorentzian L is then given by

$$L = 2\sqrt{\frac{\phi(\Omega^2 + \hbar^2\phi\Gamma)}{\Gamma}}\,, \tag{3.16}$$

and for low Rabi energies it becomes

$$L = 2\hbar\phi\,, \tag{3.17}$$

and in the absence of dephasing ($\phi = \Gamma/2$) the width of the detuning spectrum is $\hbar\Gamma$, as can be observed in [Fig. 3.2].

It is also well known that a TLS such as a QD can scatter a photon elastically (Rayleigh scattering) or inelastically. In the first case the photons have the frequency and coherence of the driving field [51, 52, 53] and just small population of the excited state is required. Along with tiny population of the excited state, the phase of the TLS is changed when a laser photon is scattered elastically [54]. In the second case the photons have the frequency and coherence dependent on the QD properties since there is energy exchange between the field and the QD. The average number of elastically scattered photons are given by [44]:

$$\langle n_{el}\rangle \;=\; \eta\Gamma\langle\sigma_+\rangle\langle\sigma_-\rangle \tag{3.18}$$

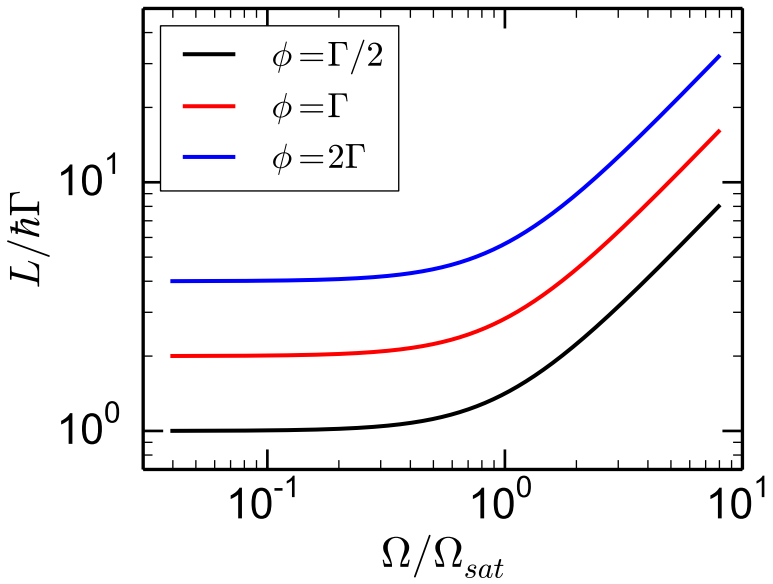

Figure 3.2: **Width of the detuning spectrum.** For low Rabi energies, the width of the detuning spectrum depends only on the decay rate and dephasing rate. As the Rabi energy increases to larger than the saturation Rabi energy, the linewidth broadens due to power broadening.

$$\langle n_{el} \rangle = \eta\Gamma \left|\rho_{ge}\right|^2 \tag{3.19}$$

$$\langle n_{el} \rangle = \frac{\eta\Gamma\Omega^2(\Delta^2 + \hbar^2\phi^2)}{4(\Delta^2 + \phi\Omega^2/\Gamma + \hbar^2\phi^2)^2} \,, \tag{3.20}$$

and the fraction of photons which are inelastically scattered can be calculated directly from $\langle n_{inel} \rangle = \langle n \rangle - \langle n_{el} \rangle$ giving

$$\langle n_{inel} \rangle = \frac{\eta\Omega^2[\Delta^2(2\phi - \Gamma) + \hbar^2\phi^2(2\phi + \Gamma) + 2\phi^2\Omega^2/\Gamma]}{4(\Delta^2 + \phi\Omega^2/\Gamma + \hbar^2\phi^2)^2} \,. \tag{3.21}$$

The contribution of the elastically and inelastically scattered photons in the detuning spectrum can be observed in [Fig. 3.3], where the decay rate was kept constant and the dephasing rate equal to zero.

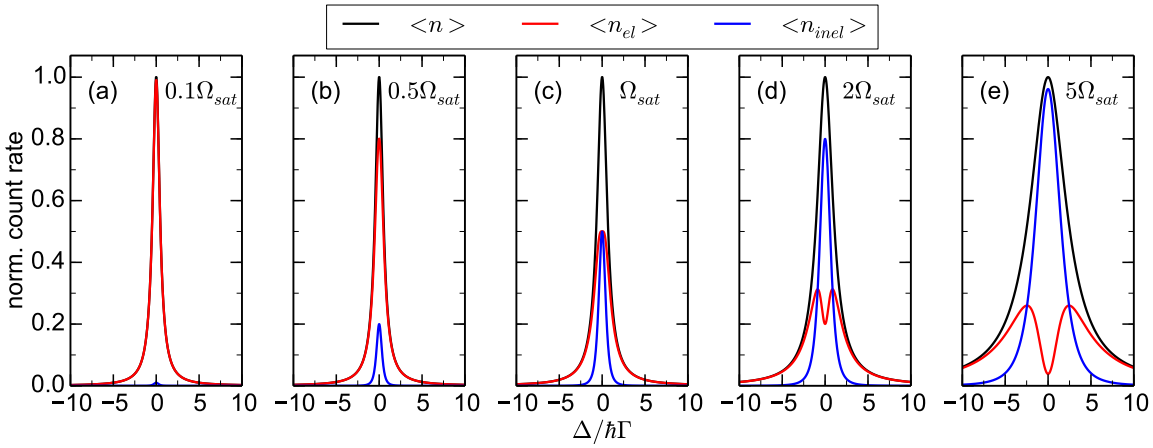

Figure 3.3: **Detuning spectrum.** The contribution of the elastically (red line) and inelastically (blue line) scattered photons to the total number of photons (black line) depends on the Rabi energy and it is mostly elastic when $\Omega < \Omega_{sat}$ (a-b) and mostly inelastic when $\Omega > \Omega_{sat}$ (d-e) for $\Delta \sim 0$.

The photon counting statistics can be used to extract important information about the QD like the radiative decay rate Γ and the pure dephasing rate ϕ using [Eqs. 3.13, 3.20 and 3.21] but to measure the precise number of the photons scattered by the QD may be challenging because of fluctuations caused by interactions between the QD and its environment elements (nuclei spin and surrounding charge carriers) and experimental noise [55, 56, 57, 58, 59, 60]. To overcome this problem we use the ratio between the total number of photons and the elastically scattered photons, given by

$$\frac{\langle n_{el}\rangle}{\langle n\rangle} = \frac{\Gamma}{2\phi}\frac{(\Delta^2+\hbar^2\phi^2)}{(\Delta^2+\phi\Omega^2/\Gamma+\hbar^2\phi^2)}\,, \tag{3.22}$$

which is still dependent of the decay rate and the dephasing rate. For small Rabi energies

$$\frac{\langle n_{el}\rangle}{\langle n\rangle} = \frac{\Gamma}{2\phi}\,, \tag{3.23}$$

as we can see in [Fig. 3.4]

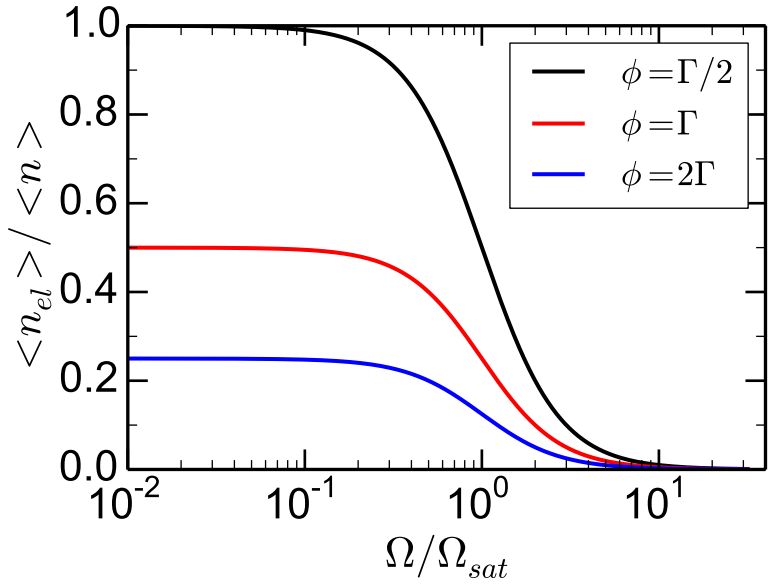

Figure 3.4: **Ratio between the amount of elastically scattered photons and the total number of photons.** The ratio $\langle n_{el}\rangle/\langle n\rangle$ depends strongly on the dephasing and in the low Rabi energy regime ($\Omega \ll \Omega_{sat}$) it can give a direct measurement of the dephasing rate if the decay rate is known.

Photon counting statistics under spectral fluctuations

This section is dedicated to the discussion of the consequences of the spectral fluctuations, caused by charge noise and spin noise, on the photons emitted by the QD.

Charge noise is present under both incoherent [61, 62, 63] and coherent [27, 51, 55, 56, 64, 57] excitation. The origins of the charge traps that host the fluctuations can vary depending on the sample; potential sources include nearby surface states in processed photonic structures [65, 66, 67], traps created at heterostructure interfaces [55], impurities from intentional dopants [27], and residual background dopant impurities [64, 68]. Charge noise is often identified as an origin of increased ensemble dephasing and decreased two-photon interference visibility [63, 69, 70, 71].

In self-assembled QDs, the surface between the superlattice and the capping layer has some defects able to trap charges, which we believe to be the main source of charge noise in Sample 1 with weak spectral fluctuations [55]. The charges interact with the QD via the Stark effect shifting its transition energy and detuning it from the driving field, causing spectral fluctuations [55, 56, 57]. For Sample 2, the main source of charge noise likely originates from a very high impurity/defect density that is caused by the molecular beam epitaxy chamber. It has been demonstrated that it is possible to stabilize the QD RF signal under charge noise using a fraction of photons in a feedback loop [58, 59].

Another source of spectral fluctuations is the interaction between the electron spin and Overhauser field, originating from nuclear spins [56, 72, 73, 74, 75, 76, 77]. The Overhauser field imposes spectral fluctuations through the Zeeman splitting, which is expected to be on the order of 0.8 μeV for Sample 1 [77]. The interaction between the Overhauser field and the electron spin is discussed in more detail in [Sec. 4.2].

For the inclusion of the spectral fluctuations in the TLS model, the detuning needs to be separated into two parts: one tunable detuning Δ due to the applied bias voltage V_g and another detuning δ caused by the noise. It is considered that the noise has a normal distribution, which is a good approximation for long measurement times [57]. Here the dephasing caused by the fluctuation of the eigenenergies due to noise is not considered because it is much slower than other incoherent processes, as we can conclude from experimental results also presented in this thesis.

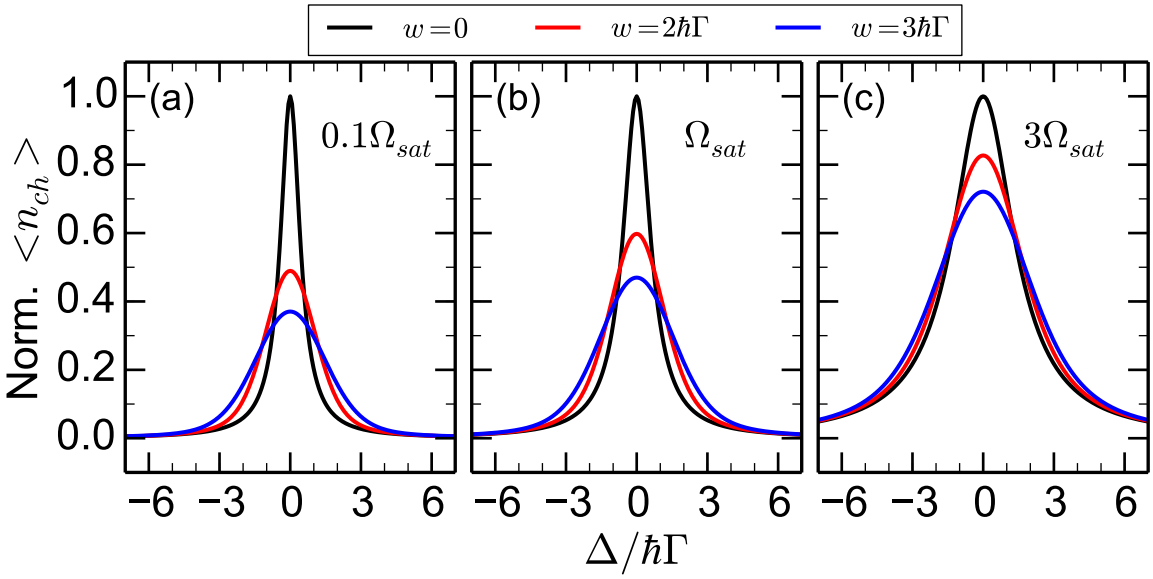

Figure 3.5: **Detuning spectrum under charge noise for $\phi = \Gamma/2$.** The spectral fluctuations have strong influence on the detuning spectrum when the width of the noise distribution is larger than the width of the detuning spectrum (a). The influence of the charge noise diminishes as the linewidth of the detuning spectrum increases due to power broadening (b-c).

The noise was included in the photon counting statistics by numerically integrating the expected number of photons [Eqs. 3.13, 3.20, 3.21] over the normal distribution of the detuning:

$$\langle n_{ch} \rangle = \frac{1}{\sqrt{2\pi\sigma^2}} \int_{-\infty}^{+\infty} e^{-\delta^2/2\sigma^2} \langle n \rangle d\delta \,, \tag{3.24}$$

where σ is related to the width of the normal distribution w by

$$w = 2\sigma\sqrt{2\ln 2} \,. \tag{3.25}$$

The effect of the charge noise on the detuning spectrum depends on how the width of the noise distribution compares with the width of the detuning spectrum. For high values of $w/\hbar\Gamma$, the charge noise strongly diminishes the number of photons scattered by the TLS, and its linewidth increases as a consequence of the spectral fluctuations. As the Rabi frequency is increased, the linewidth of the detuning spectrum also increases due to the power broadening, and consequently, the spectral fluctuations have smaller effect on it [Fig. 3.5].

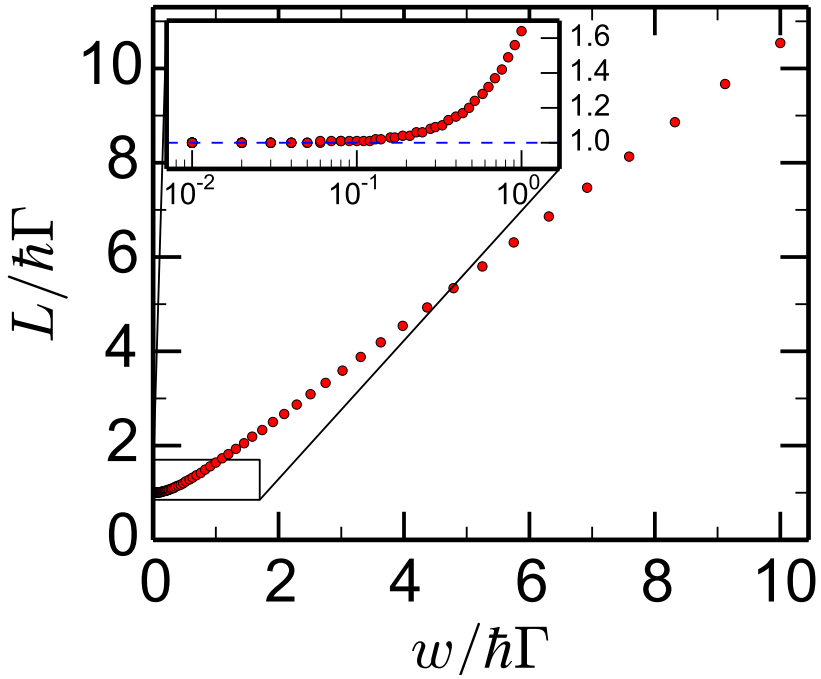

Figure 3.6: **Effect of the charge noise on the linewidth of the detuning spectrum.** For small values of w, the detuning spectrum is the same as expected for an ideal TLS (zoomed inset). As w increases, the width of the detuning spectrum increases linearly with w.

The dependence of the detuning spectrum linewidth on the charge noise distribution for $\Omega = 0.1\Omega_{sat}$ is analysed in [Fig. 3.6], where it is possible to observe that, for small values of $w/\hbar\Gamma$, the charge noise has no effective influence on the photon emission by the TLS and its linewidth equals $\hbar\Gamma$ for $\phi = \Gamma/2$ (see zoomed inset). As $w/\hbar\Gamma$ increases, the spectral fluctuations start broadening the detuning spectrum, which has its width depending linearly on the width of the noise distribution.

The ratio between the coherently scattered photons and total number of photons is also affected by the charge noise, and its value can be calculated as

$$\frac{\langle n_{ch,el}\rangle}{\langle n_{ch}\rangle} = \frac{\int_{-\infty}^{+\infty} e^{-\delta^2/2\sigma^2}\langle n_{el}\rangle d\delta}{\int_{-\infty}^{+\infty} e^{-\delta^2/2\sigma^2}\langle n\rangle d\delta} \,. \tag{3.26}$$

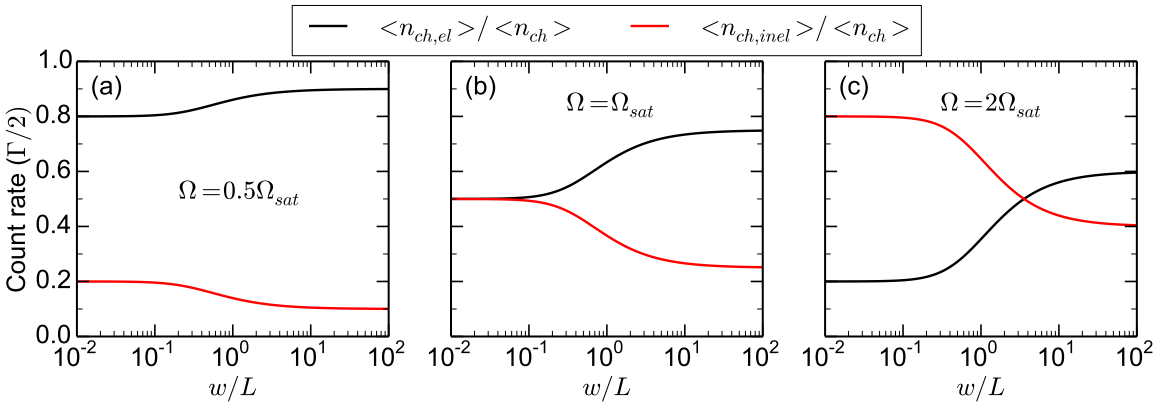

Figure 3.7: **Effect of charge noise on the fraction of elastically and inelastically scattered photons for $\Delta = 0$ μeV.** The ratio $\langle n_{ch,el}\rangle/\langle n_{ch}\rangle$ ($\langle n_{ch,inel}\rangle/\langle n_{ch}\rangle$) always tends to increase (decrease).

The consequences of the charge noise on the number of elastically and inelastically scattered photons can be observed in [Fig. 3.7] for three different regimes, which are below saturation, at saturation and above saturation. When w is comparable or greater than Ω the total number of photons always tends to decrease, but the ratio described in [Eq. 3.26] tends to increase with charge noise. This can be predicted by analysing the different situations displayed in [Fig. 3.3]. For $\Omega \leq \Omega_{sat}$ the number of inelastically scattered photons decreases faster than the quantity of elastically scattered photons. For $\Omega > \Omega_{sat}$ we have that $\langle n_{el}\rangle$ increases with detuning until reaching

$$\langle n_{el}\rangle = \frac{\Gamma^2}{16\phi} \tag{3.27}$$

at

$$\delta = \pm\sqrt{\frac{\phi\Omega^2}{\Gamma} - \hbar^2\phi^2} \tag{3.28}$$

for $\Delta = 0$ μeV. On the same point we have

$$\langle n_{inel}\rangle = \frac{\Gamma}{16\phi}(4\phi - \Gamma)\,, \tag{3.29}$$

and, consequently

$$\langle n\rangle = \frac{\Gamma}{4}\,. \tag{3.30}$$

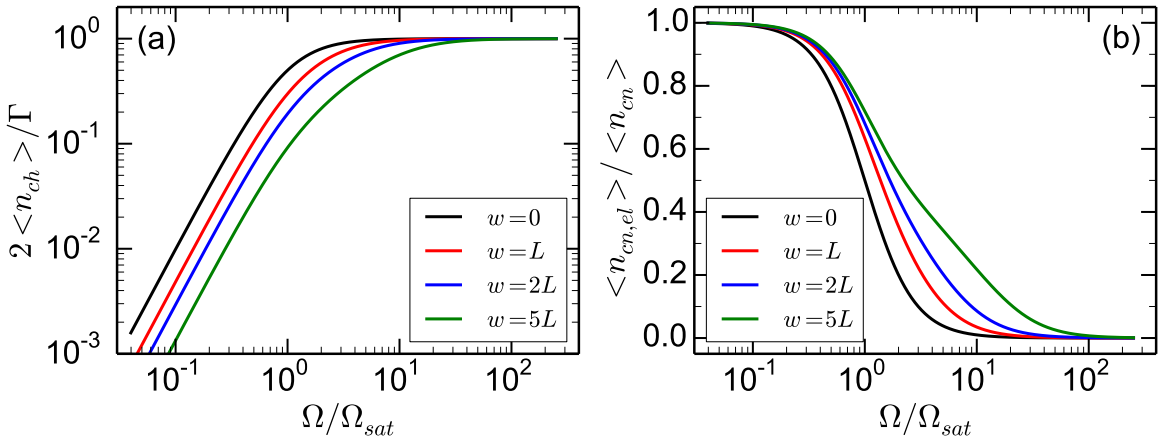

Figure 3.8: **Effect of charge noise in the photon counting statistics.** Saturation curve (a) and the ratio $\langle n_{ch,el}\rangle/\langle n_{ch}\rangle$ (b) under charge noise with the width of the normal distribution w in terms of the width of the detuning spectrum L. The other parameters are $\phi = \Gamma/2 = 0.5$ GHz.

For high Rabi energies - much greater than the detuning caused by the charge noise - the charge noise is irrelevant for the expected number of photons. This happens because the width of the detuning spectrum [Fig. 3.2] is huge - due to power broadening - when compared to the width of the normal distribution used to describes the noise. As the Rabi energy is decreased the detuning becomes more important and we can see a clear difference in the expected number of photons [Fig. 3.8 (a)].

The ratio $\langle n_{ch,el}\rangle/\langle n_{ch}\rangle$ as a function of the Rabi energy, from which important information can be extracted as discussed in [Sec. 3.1], is also expected to be sensitive to charge noise. For moderate Rabi energies, where the amount of coherent and incoherent photons are comparable, the detuning increases the ratio significantly [Fig. 3.8 (b)].

In this section, we have provided a theoretical background to support the analysis of the experimental photon statistics under spectral fluctuations using the resonance fluorescence technique.

Experimental photon counting statistics

In this section we are going to analyse the experimental results on the photon counting statistics acquired from Sample 1 (bulk sample), presenting relatively small spectral fluctuations in the resonance fluorescence experiment, and on Sample 2 ('noisy' PCA sample), with more significant spectral fluctuations. Here, we analyse the detuning spectra, the linewidth power dependence and the saturation curve, which were already discussed in [Sec. 3.1] and [Sec. 3.2], of the X^{1-} transition of the QDs in both samples.

The detuning spectrum, acquired experimentally by tuning the laser wavelength in the middle of the transition plateau and sweeping the bias voltage across the resonance between the QD optical transition and the laser, is a direct measurement of the Lorentzian peak given by [Eq. 3.13].

Results on Sample 1: relatively weak spectral fluctuations

Although the spectral fluctuations presented by this sample are much less severe than for the other devices [Sec. 3.2], they are not expected to vanish. Therefore, the spectral fluctuations must be taken into account and [Eq. 3.24] need to be considered to fit the experimental data. The experimental detuning spectrum for different excitation powers (black dots) and their correspondent fits (solid red lines) can be observed in [Fig. 3.9], where the decay rate $\Gamma = 1.3$ GHz and the saturation power $P_{sat} = 8.8(8)$ nW were extracted by Dr. Ralph Malein using power spectrum measurements, so the only free parameters were the width of the noise distribution and the overall efficiency η, from which the average over the four detuning spectra presented is $0.045(9)\%$. The blue dashed lines are the simulated detuning spectra in the hypothetical case where there are no spectral fluctuations. Using this, it is possible to estimate the number of photons not counted at $\Delta = 0$ μeV due to the spectral fluctuations, which is given by $1 - \langle n_{ch} \rangle / \langle n \rangle$, and were 0.43, 0.40, 0.34 and 0.09 for (a), (b), (c) and (d) in [Fig. 3.9], respectively.

The width of the noise distribution extracted from the fits of many spectra, including the ones presented in [Fig. 3.9], are plotted in [Fig. 3.10]. It is noticeable that there is an increase in the width of the noise distribution when the excitation power is comparable to saturation power. It is known that the average detuning due to the Zeeman splitting caused by the nuclear field is about 0.546 μeV for this QD at $\Delta = 0$ μeV [Sec. 4.2], therefore, we can conclude that the charge noise has a significant contribution to the spectral fluctuations. The poor fitting at the bottom of the detuning spectra in [Fig. 3.9 (a) - (b)] is attributed to the small nuclear spin polarisation and possible dragging effects [78, 79, 80]. For excitation powers above the saturation power, the power broadening dominates and this effect is masked. A more detailed and conclusive investigation about the cause of the phenomenon still needs to be performed. In this thesis, the effects of the charge noise on the RF power spectrum is also discussed in [Sec. 3.3.2], where the increase of the width of the noise distribution with the Rabi frequency is also observed.

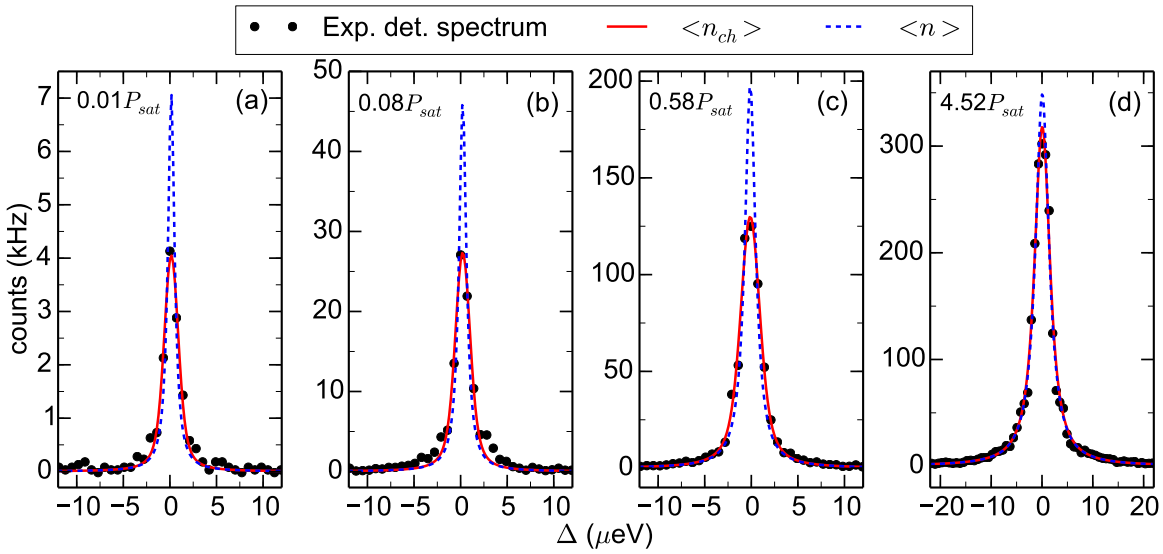

Figure 3.9: **Experimental detuning spectra.** Detuning spectra and their respective theoretical calculations using $\Gamma = 1.3$ GHz, $P_{sat} = 8.79$ nW and $\phi = \Gamma/2$ for different powers: (a) $0.01P_{sat}$, (b) $0.08P_{sat}$, (c) $0.58P_{sat}$, (d) $4.52P_{sat}$. The points represent the experimental data, the solid red lines are the fits of the expected number of photons taking into account the spectral fluctuations, and the dashed blue lines correspond to the simulation of the detuning spectrum without the spectral fluctuations.

As it was discussed previously, the saturation curve and the linewidth of the detuning spectrum as a function of the excitation power can provide important information about the QD, such as saturation parameter, dephasing rate and decay rate. The detuning spectra were measured five times for each value of the excitation power and the integration time was 10 ms per point in the spectrum. The background was calculated by averaging over 10 points far from the resonant peak. From the fit of the saturation curve [Fig. 3.11 (a)] we have that the saturation power is $26(3)$ nW and $\eta\Gamma/2 \sim 3.8(1) \times 10^5$ Hz, from where it is estimated $\eta = 0.06(1)\%$, in good agreement with the overall efficiency estimated from the detuning spectra fits ($\eta = 0.045(9)\%$). The saturation power defined from the saturation curve differs from the one defined from the RF power spectrum because the influence of the detuning causing the spectral fluctuations is stronger on the expected number of photons than on the properties of the RF power spectrum. From the background curve fit we have $BG = 33(14) + 6.5(1)P$, from where we can get the dark counts of the SPAD $BG(0)$.

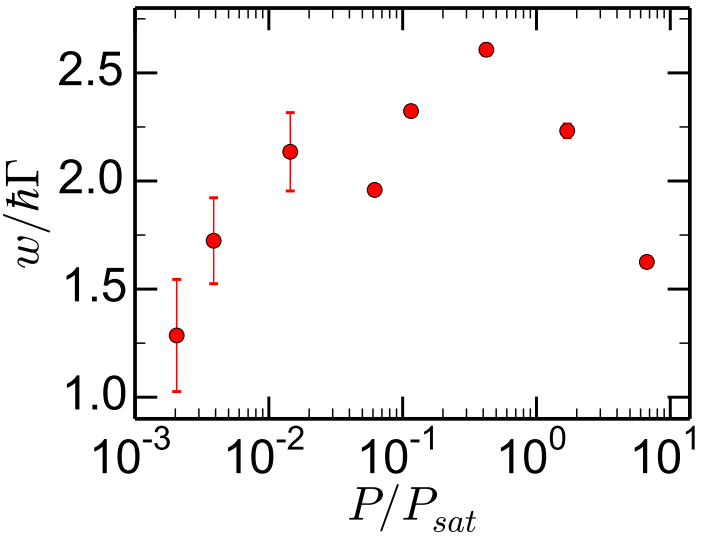

Figure 3.10: **Dependence of the charge noise on the excitation power.** The fits of the detuning spectrum exhibits a dependence of the charge noise distribution on the excitation power.

For the linewidth curve, the data points were obtained from fits of the detuning spectra and the error bars come from the statistics over the five detuning spectra [Fig. 3.11 (b)]. The function used to fit the linewidth as a function of the excitation power was $L = a\sqrt{P + P_{sat}}$ and from the fit $a = 0.334(7)$ μeV/nW$^{1/2}$ and $P_{sat} = 29(4)$ nW, in good agreement with the saturation curve [Fig. 3.11 (a)]. Therefore, the minimal value possible for L is ~ 1.812 μeV, in contrast with the minimal $L = 0.856$ μeV expected in the absence of the spectral fluctuations.

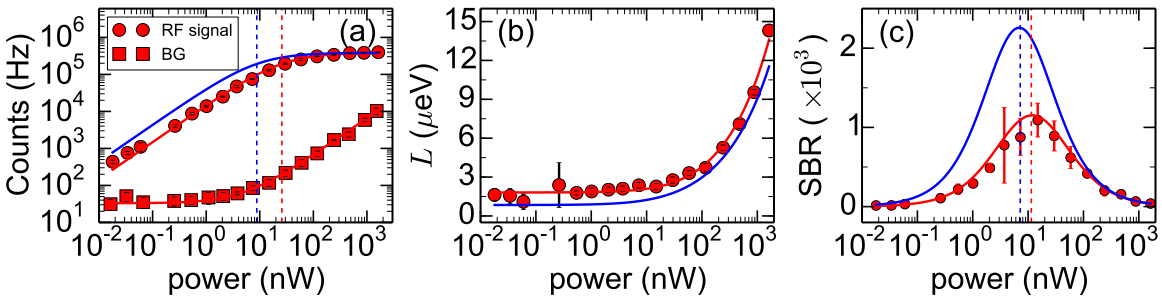

Figure 3.11: **Power sweep measurement.** (a) The saturation curve (circle points) was fitted using [Eq. 3.14]. From the fit, the saturation power (dashed red line) is $26(3)$ nW. The linear fit for the background curve (square points) returned $33(14)+6.5(1)P$. The solid and dashed blue lines represents the saturation curve and the expected saturation power of the system without the spectral fluctuations. (b) The linewidth L of the detuning spectra as a function of the excitation power (red points) was fitted using the function $L = a\sqrt{P + P_{sat}}$, and from the fit $a = 0.334(7)$ μeV/nW$^{1/2}$ and $P_{sat} = 29(4)$ nW. Therefore, the minimal value possible for L is ~ 1.812 μeV The blue line is the simulated linewidth of the detuning spectrum without the spectral fluctuations. (c) Due to the high background suppression caused by LP in the collection arm, a signal to background ratio (SBR) greater than 1000 could be routinely achieved, even with the presence of the spectral fluctuations, and it was stable for an unlimited amount of time. The expected SBR curve in the absence of spectral fluctuations is also presented (blue), and the powers corresponding to the maximum SBR for both scenarios are represented by the dashed lines, which as located at 11.432 (7.207) nW for red (blue) line.

The acquisition of this experimental data in good agreement with the theoretical results was only possible because of the high suppression of the background laser, as discussed in [Sec. 2.1] and presented in [Fig. 3.11 (c)]. It is prudent to consider that the microscope alignment where the best RF signal is achieved is not necessarily identical to the alignment where the maximal background suppression is attained because of an imperfect alignment and optical components, but even so, a signal to background ratio greater than 1000 could be achieved [Fig. 3.11 (c)].

From [Eq. 3.13] and writing

$$BG = aP + b\,, \tag{3.31}$$

it is possible to calculate the power where the SBR peak will be located, and this is given by

$$\frac{d}{dP}\left(\frac{\langle n\rangle}{BG}\right)\bigg|_0 = \sqrt{\frac{P_{sat}b}{a}}\,. \tag{3.32}$$

As the spectral fluctuations decrease the effective saturation power, for the same background, the SBR peak without the spectral fluctuations is expected to happen at smaller powers [Fig. 3.11 (c)].

In this section, we have experimentally demonstrated how the spectral fluctuations af-

fect the linewidth and intensity of the QD detuning spectrum, which reflects on the saturation curve. It was shown that, for the low excitation power regimes where most of the photons are elastically scattered, the number of photons collected is only 60% of the expected.

Results on Sample 2: strong spectral fluctuations

The charge fluctuations in the environment of the QD leads to fluctuations in the number of photons scattered by the QD through the Stark shift. Despite the similarity between the samples, apart from the gold mirror, Sample 2 shows much stronger flickering in the RF signal [Fig. 3.12 (a)]. While the Lorentzian spectra of the QD in the bulk sample (Sample 1) have a minimal linewidth of $1.70(9)$ μeV [Sec. 3.2.1], the QD in the PCA sample can scatter photons in a range of about 10 μeV, and even so, the RF signal collected from it is a factor of about 10 higher than for the bulk sample.

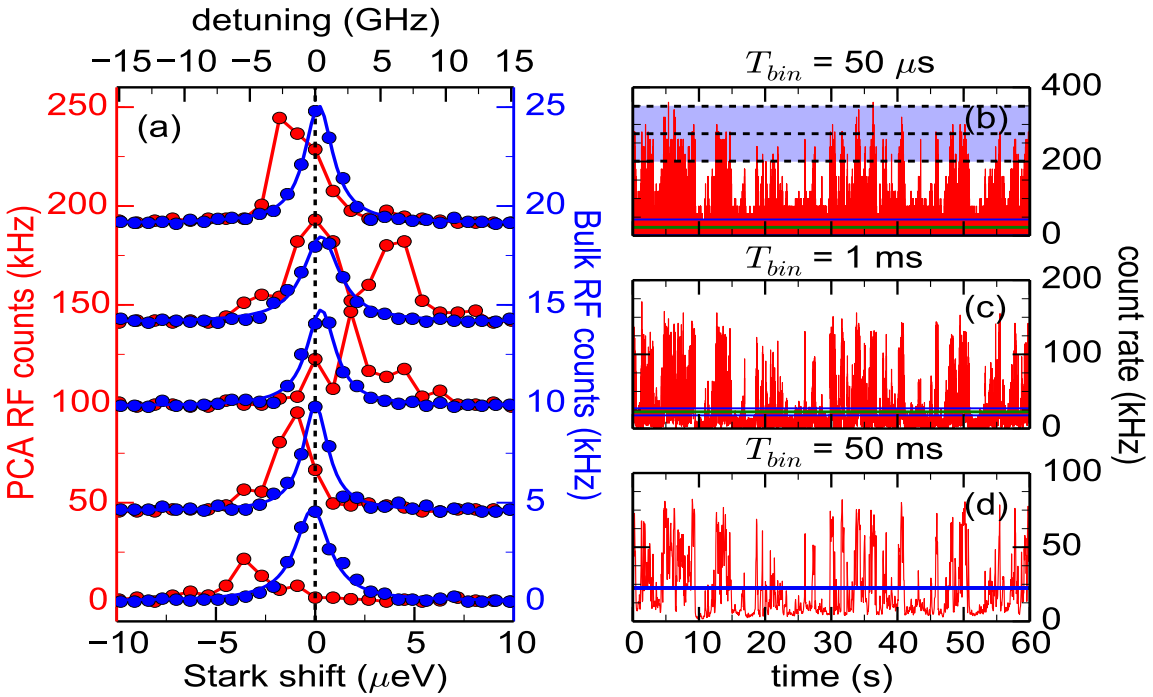

Figure 3.12: **Noise detuning spectrum and time traces for the X^{1-} transition.** (a) RF spectrum for both PCA and bulk sample acquired by exciting the QD at a power lower than the saturation power ($0.03P_{sat}$ for the PCA device and $0.01P_{sat}$ for the bulk sample) and varying the bias voltage applied to the devices. (b-d) Time traces of the RF signal for $T_{bin} = 50$ μs, 1 ms and 50 ms, respectively. These traces were acquired by setting both excitation wavelength and applied bias constant and recording the arrival time of each photon.

It is known that the charge noise dynamics is on the millisecond timescale [56, 58, 59], so if the photon counting is integrated in the sub-millisecond timescale one can resolve the

dynamics of the electric field due to charge fluctuation and eventually measure the number of photons for the case where the detuning between the QD transition energy and the laser energy is zero instead of the averaged signal over resonant and detuned times of the QD-radiation interaction. This feature is demonstrated in [Fig. 3.12 (b-d)], where RF time traces are shown for 50 μs, 1 ms and 50 ms. By changing from the millisecond to the sub-millisecond timescale measurement the maximal recorded RF signal (accounting for shot noise) increases by a factor of ≈ 4.4 [Fig. 3.12 (b)]. Here the shaded blue area corresponds to the level of shot noise in the RF signal for the averaged RF signal (green line).

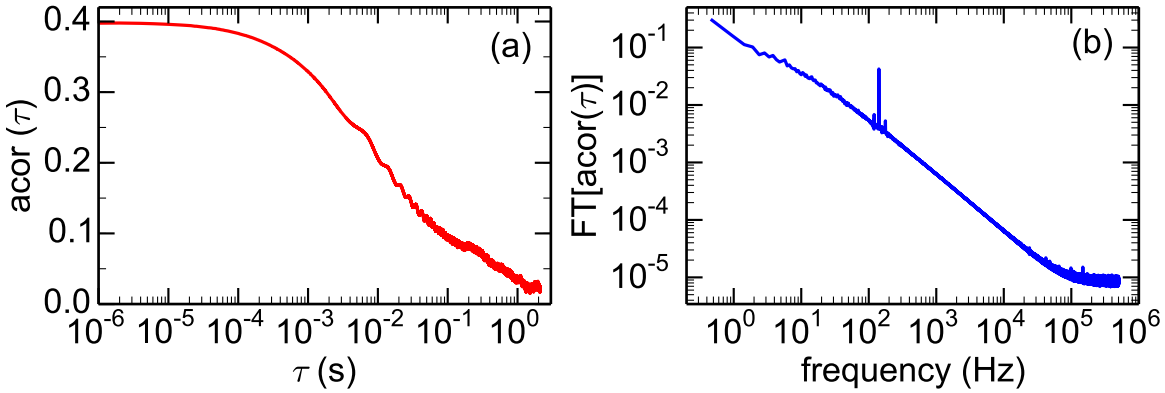

Figure 3.13: **Autocorrelation function and its power spectral density.** (a) The autocorrelation function of the RF time trace with a time bin equal to 1 μs presents a decay which starts at ~ 0.1 ms. The oscillation with small amplitude is probably a consequence of the imperfect system stabilisation. (b) The power spectral density, calculated from the Fourier transform of the autocorrelation function, shows how the noise decreases in the frequency domain. It also presents a sharp peak at 141.121 Hz corresponding to the oscillation seen in (a).

In order to analyse the dynamics of the noise in the system, including mechanical and electrical noise, the autocorrelation function $\mathrm{acor}(\tau)$ can be used, and it is given by

$$\mathrm{acor}(\tau) = \frac{1}{N}\sum_{t}\frac{(x(t)-\langle x\rangle)(x(t+\tau)-\langle x\rangle)}{\langle x(t)-\langle x\rangle\rangle^2} \tag{3.33}$$

where N is the number of points to be considered in the autocorrelation function.

The power spectral density of the autocorrelation function may also reveal some interesting features, like the exact frequency of some sinusoidal behaviour, and it is given by the Fourier transform of the $|\mathrm{acor}(\tau)|$.

The autocorrelation function of the RF time trace reveals that the noise has dynamics on the millisecond timescale [Fig. 3.13 (a)], similar to [56, 58, 59]. The autocorrelation function also presents an oscillatory behaviour with frequency equal to 141.121 Hz, which is probably a consequence of the imperfect stabilisation of the cryostat and/or the microscope

head. In the power spectral density function [Fig. 3.13 (b)] this behaviour is presented in the form of a sharp peak, localising the exact frequency of the sinusoidal curve.

A power dependence of the detuning spectrum was obtained for each sample with an integration time equal to 10 ms [Fig. 3.14], and it is a strong evidence of the difference in efficiency between the two devices, as the QD in the PCA sample saturates at a power 6.3 times smaller than the saturation power of the QD in the bulk sample. This is evidence of improved coupling between the driving field and QD [81]. The difference in the amount of photons collected above the saturation power for each sample expresses the improvement on the overall efficiency of the system η due to the design of the PCA device.

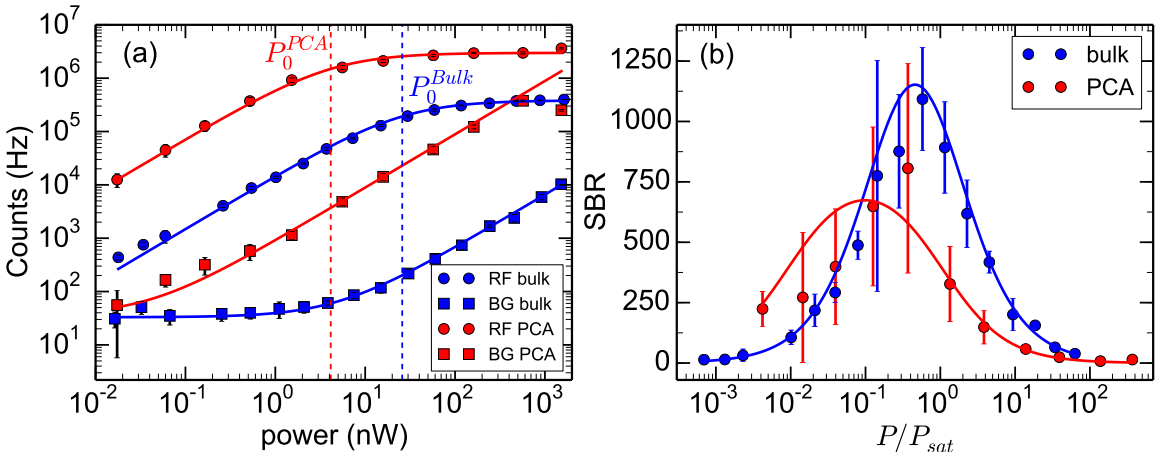

Figure 3.14: **Experimental saturation curve under strong charge noise.** (a) The blue points and curves are identical to the ones presented in [Fig. 3.11 (a)]. The PCA sample saturation curve (red circle points) was fitted using [Eq. 3.13]. From the fit, the saturation power (dashed red line) is $4.1(3)$ nW and $\eta\Gamma/2 = 3.0(1)$ MHz. The linear fit for the background curve (red square points) returned $35(65)+886(10)P$. (b) Comparison between the signal to background ratio for the PCA device (red) and the bulk sample (blue).

Based on the the second-order correlation function measurement, the decay rate Γ is about 1.6 GHz. Then the total efficiency of the system can be calculated from the fit of the saturation curve [Fig. 3.14], giving $\eta = 0.37(1)\%$ which is $8.5(4)$ times higher than the efficiency of the system using the bulk sample, reflecting the difference of photon extraction efficiency between the two samples.

The PCA device emits a non-Gaussian mode that, when aligning the confocal microscope for the best collection of the RF signal may not coincide with the best alignment for the background cancellation, giving a spatial dependence of the laser suppression by the combination of the linear polariser with the single-mode fibre using the long pass beam splitter [Fig. 2.3 (second panel)]. This factor, along with near unity reflectivity of the Au

mirror, can explain why the BG signal for the PCA device has a greater slope than for the bulk sample [Fig. 3.14 (a)].

Although the RF signal from the PCA device is much stronger than from the bulk sample, their signal to background ratios are about the same because of the worse background suppression with the PCA sample.

The estimated efficiency of the coupling into the single-mode fibre is $\eta_{smf} \sim 31.4$ % and the efficiency of the microscope combined with the detector is $\sim 0.86\%$. The main sources of photon loss in the microscope are the LP with an efficiency $\eta_{lp} \sim 43\%$, the beam splitter surfaces with $\eta_{bs} \sim 96\%^4$ and the SPAD with $\eta_{det} \sim 30\%$. Considering all these efficiencies we can calculate the sample efficiency η_{sample}, which is $10.8(4)\%$, resulting in more than 90 million of photons reaching the first lens of the microscope. For the bulk sample, this number is less than 15 million.

Resonance fluorescence power spectrum

The power spectrum of the photons scattered by a two-level system under an EM driving field was first studied by Mollow in [44], who obtained it directly from the first-order correlation function $g^1(\tau)$ which can be defined in the Heisenberg picture for the QD ladder operators as

$$g^1(\tau) = \langle \sigma_+(\tau + t)\sigma_-(t) \rangle \tag{3.34}$$

through

$$S(\omega) \propto 2\mathrm{Re}\left[\int_{-\infty}^{+\infty} g^1(\tau) e^{i\omega\tau} d\tau\right] \tag{3.35}$$

In this work we solve the time-dependent optical Bloch equations [Eq. 3.5-3.8] numerically, from where we calculate the first-order correlation function in the Schrödinger picture

$$g^1(\tau) = \mathrm{Tr}\left[\rho(0)U^\dagger(\tau + t)\sigma_+ U(\tau)\sigma_- U(t)\right] \tag{3.36}$$

$$g^1(\tau) = \mathrm{Tr}\left[\rho(t)U^\dagger(\tau)\sigma_+ U(\tau)\sigma_-\right] \tag{3.37}$$

$$g^1(\tau) = \mathrm{Tr}\left[U(\tau)\sigma_-\rho(t)U^\dagger(\tau)\sigma_+\right] \tag{3.38}$$

where $U(t)$ is the time evolution operator. So, defining a new density matrix as $\rho'(t) = \sigma_-\rho(t)$ and starting on the steady state solution for $\rho(t)$, we can rewrite [Eq. 3.38] as

$$g^1(\tau) = \mathrm{Tr}\left[\rho'(\tau)\sigma_+\right] \tag{3.39}$$

$$g^1(\tau) \;=\; \rho'_{ge}(\tau) \tag{3.40}$$

Then [Eq. 3.40] is used directly in [Eq. 3.35] to obtain the power spectrum of the resonantly scattered photons. For $\phi = 0$, the RF power spectrum for $\Omega \gg \Gamma$ is given by [44]

$$\begin{aligned} S(\omega) \;&=\; 2\pi|\rho_{ge}(\infty)|^2\delta(\omega) + \frac{\rho_{ee}(\infty)\Gamma\Omega^2}{\Omega_{eff}^4}\left\{\frac{\Omega^2/2}{\omega^2+s_0^2}\right. \\ &+\; \left.\left(\frac{3\Omega^2}{8}+\frac{\Delta^2}{4}\right)\left[\frac{1}{(\omega-\Omega_{eff})^2+\sigma^2}+\frac{1}{(\omega+\Omega_{eff})^2+\sigma^2}\right]\right\}\,, \end{aligned} \tag{3.41}$$

where

$$\Omega_{eff} \;=\; \sqrt{\Omega^2+\Delta^2} \tag{3.42}$$

$$s_0 \;=\; -\frac{\Gamma}{2}\left[\frac{\Omega^2+2\Delta^2}{\Omega^2+\Delta^2}\right] \tag{3.43}$$

$$\sigma \;=\; -\Gamma\left[\frac{3\Omega^2/4+\Delta^2/2}{\Omega^2+\Delta^2}\right]\,. \tag{3.44}$$

When the Rabi energy is much lower than the saturation Rabi energy we have the so-called Heitler regime [51, 52, 53] where the photons are mostly elastically scattered and have the same frequency and coherence of the EM driving field [Fig. 3.15 (a)]. As the Rabi energy is increased and crosses the limit of the saturation Rabi energy, the Mollow triplet appears and the side bands are separated from the central peak by the Rabi frequency Ω[1] for the case where $\Omega \gg \Delta + w$, where w is the width of the noise distribution [Fig. 3.15 (c)]. In the same figure, it is also possible to observe the change in the $\langle n_{el}\rangle/\langle n\rangle$, as it was discussed in [Sec. 3.1] and presented in [Fig. 3.4].

The experimental RF power spectrum presented in [Fig. 3.15] was acquired by using the Sample 1 (bulk sample) and a FPI with resolution of 27.5 MHz and free spectral range of 5 GHz [Sec. 2.1]. Here, an external magnetic field equal to 600 mT in the growth direction was applied to recover the TLS behaviour from the X^{1-} transition of the QD, which is destroyed by the Overhauser field [Sec. 4.2].

The low Rabi frequency spectrum was fitted using a single Lorentzian, which returned a width equal to $29(1)$ MHz, in good agreement with the expected resolution of the FPI [Fig. 3.15 (a)]. For an ideal TLS under no spectral fluctuations, some considerable amount of inelastically scattered light is expected at $\omega = 0$ when $\Omega = \Omega_{sat}/2$, but, in the present case, spectral fluctuations are present and especially high for this excitation power [Fig. 3.10],

[1] In this section, for simplification, all the parameters are in frequency units.

which increases the $\langle n_{el}\rangle/\langle n\rangle$ ratio making the amount of inelastically scattered photons negligible [Fig. 3.8 (b)].

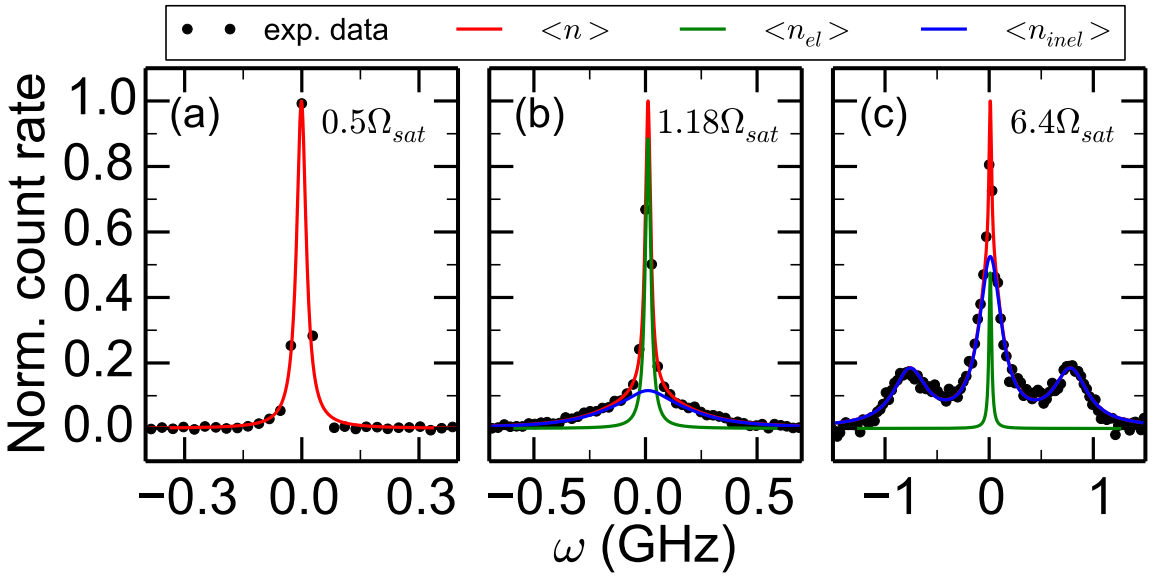

Figure 3.15: **RF power spectrum under small spectral fluctuations (Sample 1) for $\mathbf{\Delta = 0}$ MHz and $\mathbf{B_{ext} = 600}$ mT.** (a) The spectral fluctuations diminish the amount of inelastically scattered photons and at $\Omega = \Omega_{sat}/2$, the RF power spectrum could be fitted using a single Lorentzian, from where the resolution of the FPI could be extracted $(29(1)$ MHz). Above saturation, for (b) $1.18\Omega_{sat}$ (c) $6.4\Omega_{sat}$, the spectral fluctuations become less effective and the QD optical transition behaves like an ideal TLS.

For the cases where $\Omega > \Omega_{sat}$ [Fig. 3.15 (a - b)], the power spectra were fitted using [Eq. 3.41], with the delta function replaced by a normalised Lorentzian peak with width equal to the measured FPI resolution (29.3 MHz). As it was discussed in the previous section [Sec. 3.2], these spectra are expected to be less sensitive to the spectral fluctuations due to their high Rabi frequency relative to the width of the noise distribution. This claim was confirmed with the good agreement between the experimental data and their fits, which returned $\Gamma = 1.63(4)$ GHz.

Since the elastically and inelastically scattered photons can be clearly distinguished in a RF power spectrum measurement, it is possible to extract $\langle n_{el}\rangle/\langle n\rangle$ from a power sweep of RF power spectra. The experimental data (red) accompanied by the simulation of an ideal TLS (blue) is shown in [Fig. 3.16][2], where it can be observed that, for high Rabi frequencies, the experimental data is in good agreement with what is expected from an ideal TLS. But for this particular QD, as the Rabi frequency is decreased, the spectral fluctuations become important and the experimental data deviates from the ideal TLS curve.

[2]Note that this experimental data does not correspond to the one presented in [77]

In this section, the RF power spectrum of an ideal TLS was discussed and the experimental data acquired using the bulk sample (Sample 1) was presented. This sample presents relatively small spectral fluctuations for some excitation powers and, under a modest external magnetic field, it offers the best match to an ideal TLS among all the other samples when using the X^{1-} transition.

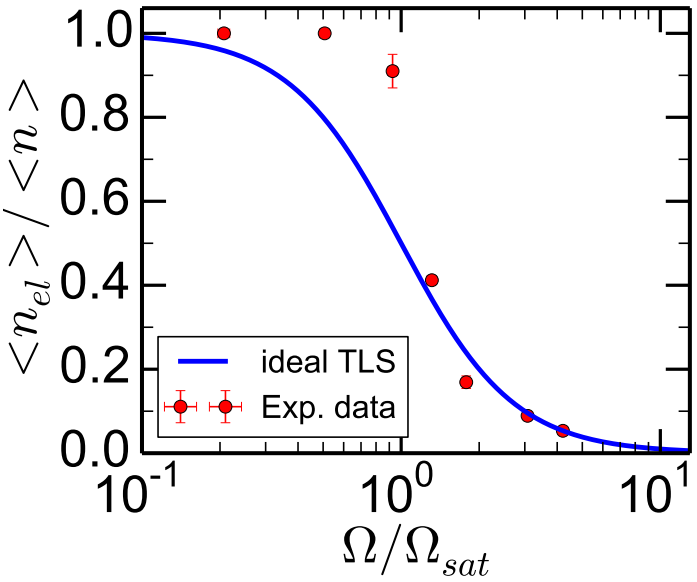

Figure 3.16: $\langle n_{el}\rangle/\langle n\rangle$ **ratio extracted from the RF power spectrum (Sample 1).** For high Rabi frequencies, the TLS behaviour is recovered and there is an agreement between the TLS simulation and the data points. As the excitation power is decreased, the spectral fluctuations become important and the experimental data deviates from the ideal TLS.

Noisy resonance fluorescence spectrum

The spectrum of the resonantly scattered photons is also severely affected by charge noise. Beyond the change in the number of elastic and inelastic photons, there are also changes in the shape of the Mollow triplet like the modest increase in the width of the inelastic central peak and a more pronounced increase in the width of the side bands. There is also a change in the intensity of the side bands relative to the intensity of the inelastic central peak and a considerable modification in the position of the side bands, as we can conclude from [Fig. 3.17], where just the inelastic fraction of the RF spectrum is shown since only the intensity of the elastic fraction is expected to change because its frequency and coherence depend only on the driving field.

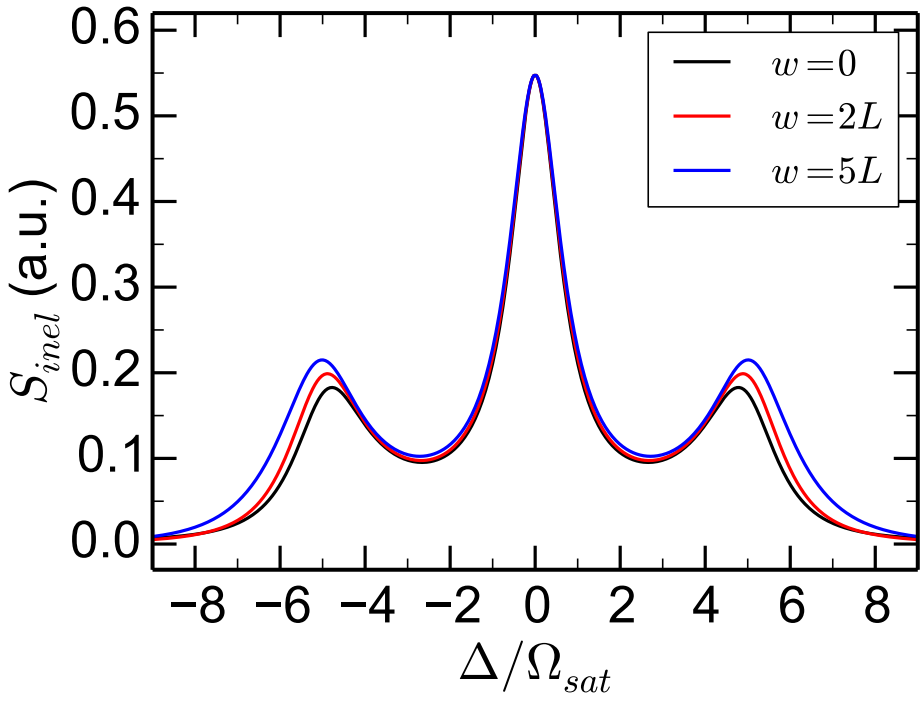

Figure 3.17: **Incoherent fraction of the RF spectrum in the presence of charge noise.** The spectra were normalized to make $S(0)$ equal for all of them. No dephasing rate was taken into account and the Rabi energy was $5\Omega_{sat}$.

To describe the dependence of the width of the side band Γ_{side} and the width of the incoherent central peak $\Gamma_{central}$ on the charge noise we fit the spectrum using three lorentzian peaks, from where the error bars were extracted [Fig. 3.18]. The Rabi energy used ($8\Omega_{sat}$) was large enough to make the side bands well separated from the central peak, like in [Fig. 3.17].

The detuning caused by charge noise affects the width of the incoherent central peak first, which explains why the ratio $\Gamma_{side}/\Gamma_{central}$ (black points in [Fig. 3.18]) goes below the ideal 1.5 (indicated by the black dashed line) for a small range of w. Then the curve for $\Gamma_{central}$ saturates while Γ_{side} continues increasing, taking the ratio far from the ideal case.

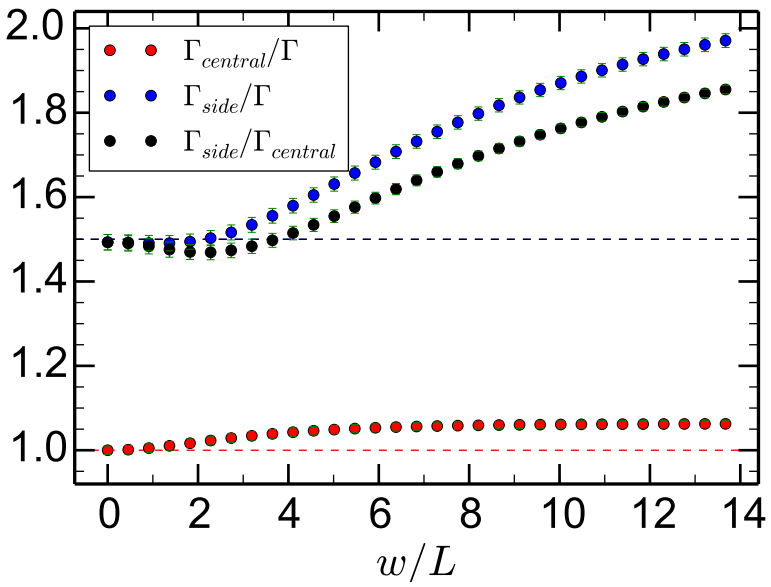

Figure 3.18: **Width of the side band and incoherent central peak as a function of the charge noise distribution.** Both Γ_{side} (blue line) and $\Gamma_{central}$ (red line) increase with the width of the normal distribution of the charge noise. The black (red) dashed line indicates the ideal case for the ratio $\Gamma_{side}/\Gamma_{central}$ ($\Gamma_{central}/\Gamma$).

Along with the broadening, the side bands also undergo a shift in their positions due to the detuning imposed by the charge noise. This shift, defined as $(\Omega_{eff} - \Omega)/2\pi\hbar$ where the effective Rabi energy Ω_{eff} indicates the new position of the side bands, is always positive and has a steep slope until the width of the normal distribution w reaches about 10 times the width of the detuning distribution L (not considering power broadening). After this, the shift continues increasing, but in a more modest rate [Fig. 3.19 (a)].

Under strong charge noise the broadening of the side bands is also accompanied by a decrease in their intensity compared to the elastic peak, which makes the Mollow triplet much less visible [Fig. 3.19 (b)]. The intensity of the incoherent central peak is also strongly affected.

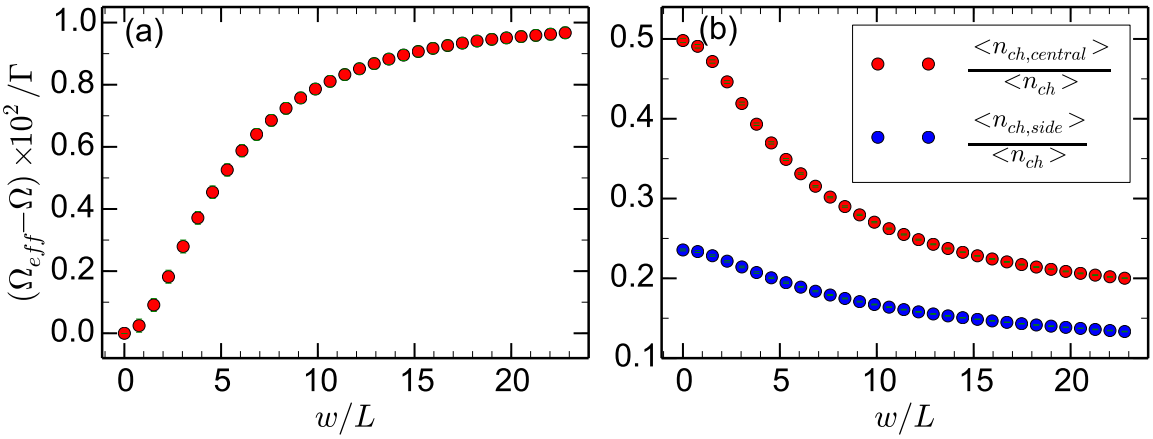

Figure 3.19: **Effects of charge noise on the side band position and on the intensities of the incoherent central peak and side bands.** The side band shift (a) and the loss of intensity (b) caused by the charge noise for a Rabi energy equal to $8\Omega_{sat}$, the decay rate was 1 GHz and the dephasing rate was equal to zero.

Experimental RF spectrum of the noisy planar cavity antenna sample

Strong charge noise regime (Sample 2)

In this experiment we investigated the RF spectrum of the photons scattered from X^{1-} optical transition of a QD in the noisy PCA device, which has a relatively high intrinsic charge noise. For these measurements, a FPI with a resolution of 27 MHz and free spectral range equal to 5 GHz was used. A magnetic field equal to 1 Tesla in the Faraday geometry was applied to decrease the effects of the nuclear field on the QD transitions by decreasing the Raman scattering rate [Sec. 4.2]. The RF spectrum for Rabi frequencies equal to $0.45\Omega_{sat}$, $1.01\Omega_{sat}$, $2.31\Omega_{sat}$, $7.41\Omega_{sat}$ and $8.89\Omega_{sat}$ are shown in [Fig. 3.20 (a-e)] where $\Omega_{sat} = 0.135$ MHz, with $\Gamma = 1.195$ GHz based on the second-order correlation measurement. When $\Omega < \Omega_{sat}$ a higher contribution of elastically scattered photons is expected (solid green line), so the charge noise has a minor effect. But when $\Omega > \Omega_{sat}$ the Mollow triplet appears along with some considerable number of elastically scattered photons - as predicted in [Sec. 3.2] - composing a Lorentzian peak with width equal to the resolution of the FPI.

From the measurement of the RF spectrum for different powers we can obtain the experimental ratio $< n_{ch,el} > / < n_{ch} >$ and trace the dependence of the charge noise distribution on the power. For this, the numerical methods discussed in [Sec. 3.2] and [Sec. 3.3.1] are used and the results can be observed in [Fig. 3.21].

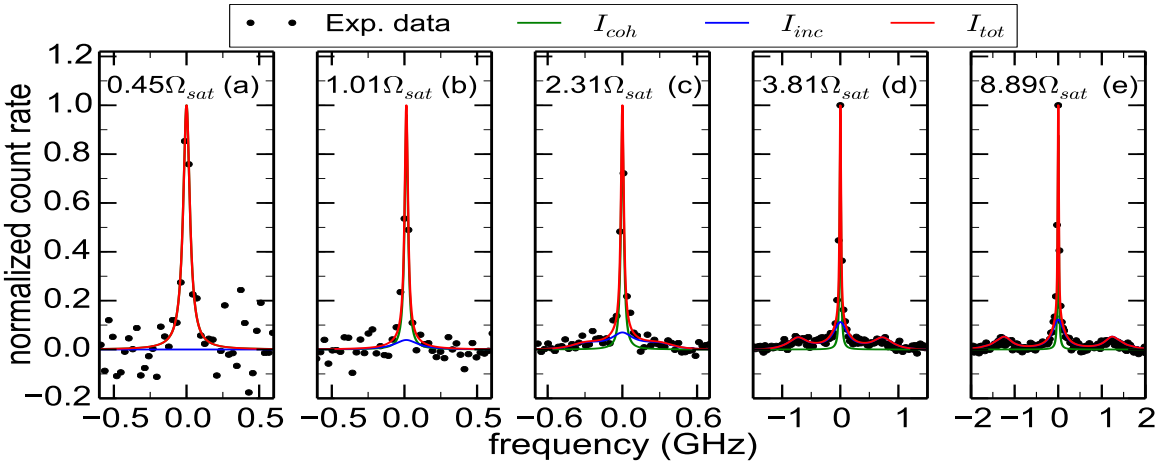

Figure 3.20: **RF power spectrum under strong charge noise at different Rabi frequencies.** The experimental RF spectra were measured using a FPI and fitted with the model presented in [Sec. 3.3.1]. (a)-(b) The charge noise can be neglected when in the low power regimes because most of the photons are elastically scattered. (c)-(e) At high powers there is still a considerable quantity of elastically scattered photons due to the strong charge noise.

As it was expected, the experimental ratio - red points in [Fig. 3.21 (a)] - presented a deviation from the curve for the ideal TLS (black solid line) due to charge noise. The blue solid line is a fit for the experimental data where the charge noise is taken into account, using [Eq. 3.26] with a constant w, from where we obtain $w = 2.4(7)$ μeV. This function seems to fit the data well, although from the fits of the individual power spectra it is known that the width w changes linearly with power for the range measured [Fig. 3.21 (b)] as $w(\Omega) = 0.3(2) + 6.2(3)\Omega$ (blue solid line).

Because the RF power measurement is acquired under a constant bias voltage, when the detuning due to charge noise and Overhauser field is much greater than the width of the detuning spectrum L, the RF signal becomes too small to be measured, hence, the fits for the RF power spectrum may return a noise distribution with width smaller than expected, especially for Rabi frequencies where the power broadening is not significant. This may also explain why the width of the detectable noise distribution increases linearly with the Rabi frequency.

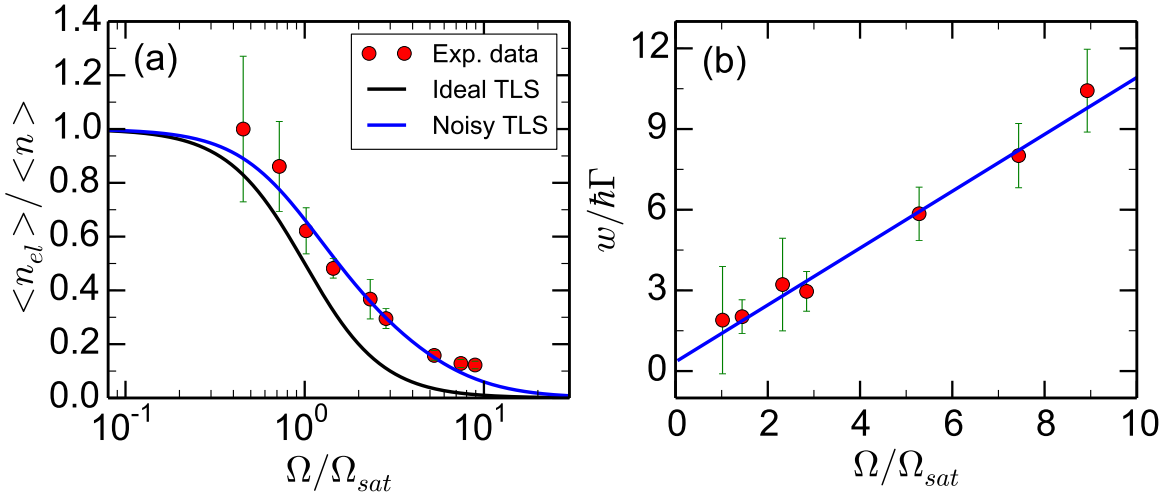

Figure 3.21: $\langle \mathbf{n_{ch,el}}/\langle \mathbf{n} \rangle \rangle$ **under charge noise and the dependence of the width of the charge noise distribution on the Rabi energy.** (a) The experimental data (red points) are fitted with [Eq. 3.26] for a constant σ (blue solid line). The curve for the TLS under spectral fluctuations is compared with the curve for an ideal TLS (black solid line). (b) The width of the noise distribution presents a linear dependence on the Rabi frequency, but this mechanism is still not understood.

Moderate charge noise regime (Sample 3)

Similar measurements were also performed using another PCA device with less intrinsic sources of charge noise. In this case the RF spectrum is closer to the ideal, but a significant amount of elastically scattered photons can still be observed along with the Mollow triplet at $\Omega = 7.4\Omega_{sat}$ [Fig. 3.22 (a)].

In this sample (Sample 3), a linear dependence of the width of the noise distribution is also observed. For low Rabi frequencies the width w is similar to the previous sample discussed, but the slope of the linear function is smaller for this case, i.e., the increment on w is $5(1)$ smaller for the same $d\Omega$ when compared to the previous device (Sample 2). For this sample we have $w(\Omega) = 2.4(4) + 1.4(4)\Omega$ where w is in μeV and Ω is in GHz.

This intriguing dependence of the noise distribution can also be observed in the detuning spectrum and, although it is challenging to quantify the noise from these spectra because it requires a fast bias voltage sweep and a higher extraction efficiency, it can be analysed over a larger range of excitation power.

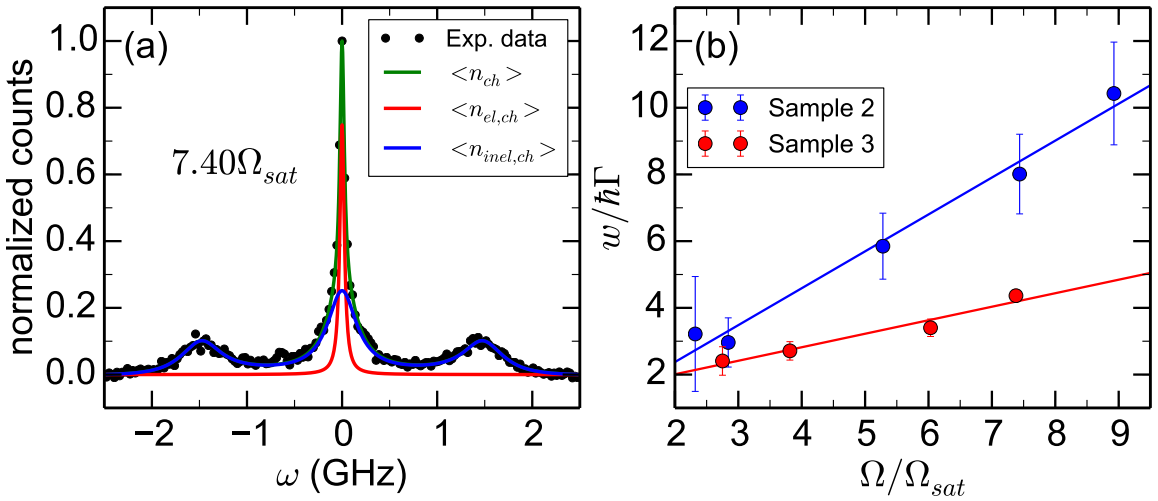

Figure 3.22: **RF spectrum and charge noise dependence on the Rabi frequency for a PCA device with weak charge noise.** (a) For this QD it was measured $\Gamma = 1.75$ GHz from the width of the inelastic central peak. (b) The width of the charge noise distribution presents a linear dependence on the Rabi frequency and its function is $w(\Omega) = 2.4(4) + 1.4(4)\Omega$ for Sample 3, which has a slope $5(1)$ smaller than the QD in Sample 2.

For very low Rabi frequencies, the energy of the QD varies with time and the Lorentzian peak appears in some random position [Fig. 3.23 (a)] or it does not appear depending on the speed of the measurement, as the attempt number 3 in [Fig. 3.23 (a)]. As the Rabi frequency is slightly increased the QD gets suddenly stable and the detuning spectrum is now a reproducible Lorentzian peak [Fig. 3.23 (b)]. If we keep increasing the Rabi frequency, then it gets noisy again, but now instead of a single Lorentzian peak at some random position it is observed a bunch of Lorentzian peaks in a single bias voltage sweep [Fig. 3.23 (c)]. For very high Rabi frequencies where the power broadening is significant the width of the detuning spectrum becomes greater than the width of the noise distribution and then detuning spectrum become a single broad Lorentzian [Fig. 3.23 (d)]. This feature could be observed in all the samples cited in this thesis with the only difference among them being the intensity of the noise. The negative energy shift which happens at high Rabi frequency [Fig. 3.23 (d)] is also a mystery. For other QDs in the sample, the shift energy can be positive.

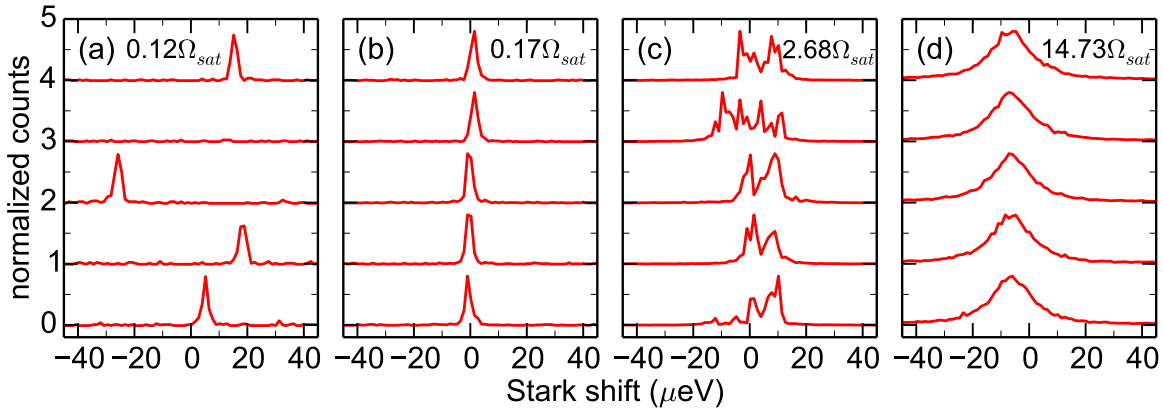

Figure 3.23: **Power dependence of the spectral fluctuations in the X^{1-} transition through the detuning spectrum.** The noise profile changes with the excitation power. (a) At $0.12\Omega_{sat}$ the detuning spectrum is a single Lorentzian at some random position over time. (b) At $0.17\Omega_{sat}$ the detuning spectrum becomes stable. (c) At $2.68\Omega_{sat}$ the noise is back and a bunch of Lorentzian spectra can be observed in a single bias voltage sweep. (d) At $14.73\Omega_{sat}$ the power broadening is dominant over the noise detuning.

Second-order correlation function

The photon emission from a quantum two-level system happens only when there is some probability for the QD to be in the excited state, as was described in [Sec. 3.1]. However, every time a photon is emitted the QD decays to the ground state and needs to be re-excited to emit the next photon. These processes require time, so it is impossible for the QD to radiate two photons simultaneously, resulting in photon antibunching in the second-order correlation function $g^{(2)}(\tau)$, which is related to the probability of counting two photons with a time delay τ between them. A single photon source [46, 82, 83, 84] is crucial for quantum information science [85]. This is an exclusive property of quantum systems, consequently Maxwell's equations cannot be used to describe it.

To probe this feature of quantum systems we investigate the second-order correlation function [38]

$$g^2(\tau) = 1 - e^{-(\phi+\Gamma)\tau/2}\left(\cos(\nu\tau) + \frac{(\phi+\Gamma)}{2\nu}\sin(\nu\tau)\right) \tag{3.45}$$

with

$$\nu = \sqrt{\left(\frac{\Omega}{\hbar}\right)^2 - \left(\frac{\Gamma-\phi}{2}\right)^2}\,. \tag{3.46}$$

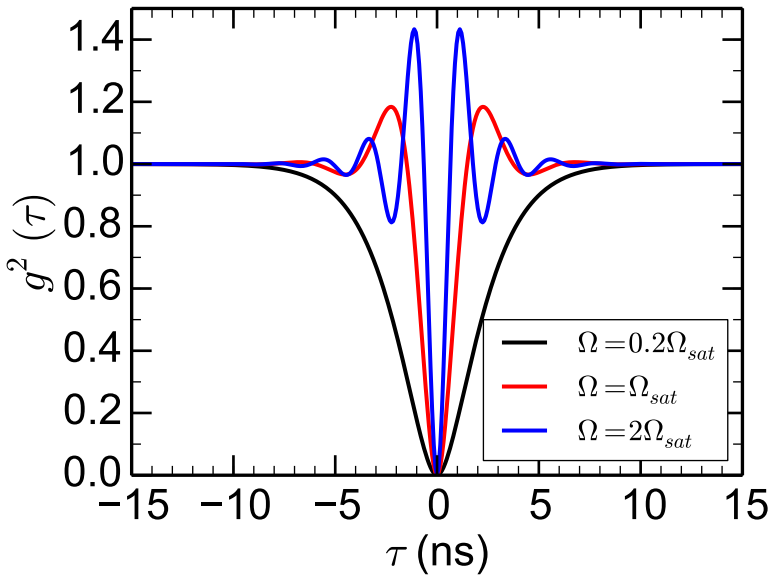

Figure 3.24: **Second-order correlation function for $\Delta = 0$ and $\phi = \Gamma/2$.** $g^2(\tau)$ with $\Gamma = 1$ GHz and (a) $\Omega = 0.2\Omega_{sat}$ (b) $\Omega = \Omega_{sat}$ (c) $\Omega = 2\Omega_{sat}$.

The second-order correlation function can be understood as the probability of counting two photons with a time interval τ between them and, as we can see in [Eq. 3.45], the probability of counting two photons simultaneously is equal to zero ($g^2(0) = 0$), confirming that a radiative TLS is a single-photon source.

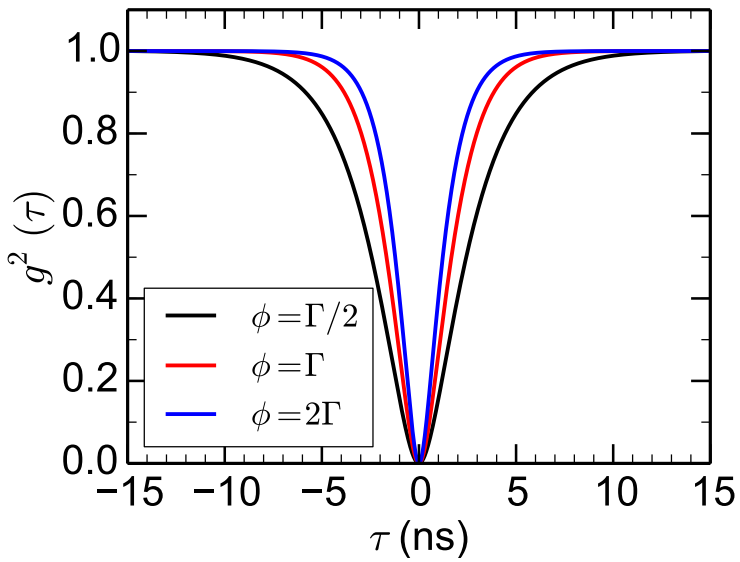

Figure 3.25: **Effect of dephasing rate in $g^{(2)}(\tau)$ in the Heitler regime.** Second-order correlation function in the Heitler regime with $\Omega = 0.2\Omega_{sat}$, $\Gamma = 1$ GHz and $\Delta = 0$ μeV.

When

$$\Omega^2 > \left(\frac{\hbar(\Gamma - \phi)}{2}\right)^2 \tag{3.47}$$

the Rabi oscillations can be observed (blue line in [Fig. 3.24]). If the Rabi energy is much

lower than the decay rate, then

$$\nu \approx \frac{i(\Gamma - \phi)}{2} \tag{3.48}$$

and $g^2(\tau)$ will depend only on the decay rate and dephasing rate, and the consequence of having a dephasing rate different from zero in the Heitler regime can be observed in [Fig. 3.25].

Numerical calculations of $g^2(\tau)$ were also performed by applying the same method as for $g^1(\tau)$ in the beginning of [Sec. 3.3]. In this case, the detuning could also be included and its consequences can be observed in [Fig. 3.26]. From the optical Bloch equations [Eq. 3.5 - 3.8], we can observe that a non-zero detuning Δ produces an oscillating term in the coherence element ρ_{eg}, even in the Heitler regime. This oscillation also appears in the population element ρ_{ee} due to its dependence on $\mathrm{Im}[\rho_{eg}]$, and, consequently, it can be observed in the second-order correlation function along with a change in the slope at $\tau < 1/\Gamma$.

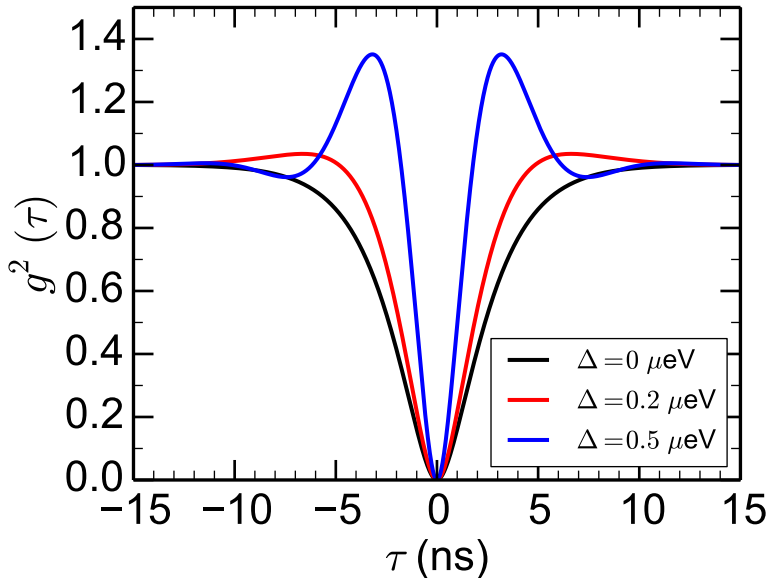

Figure 3.26: **Effect of detuning on $g^{(2)}(\tau)$ in the Heitler regime.** Second-order correlation function in the Heitler regime with $\Omega = 0.2\Omega_{sat}$, $\Gamma = 1$ GHz and $\phi = \Gamma/2$.

Experimental second-order correlation function

The experimental second-order correlation function is obtained from the histogram of the delay time between the arrival time of the photons, which is recorded using a TCSPC module [Sec. 2.5].

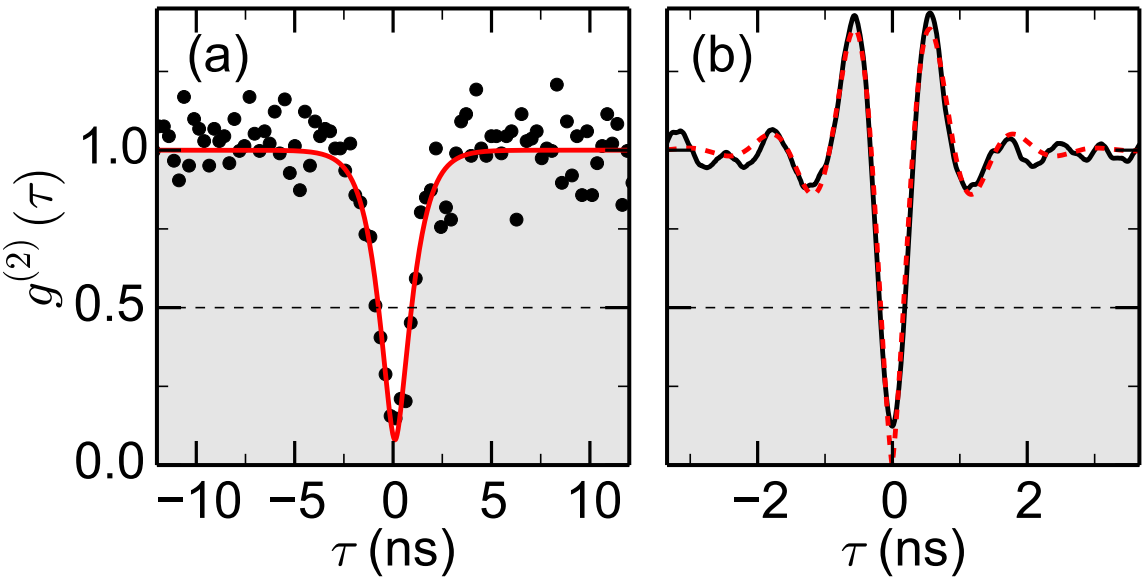

Figure 3.27: **Experimental second-order correlation function of the X^{1-} transition.** (a) The experimental data (black points) was acquired at $P = 0.06P_{sat}$ in Sample 1 and it was fitted using [Eq. 3.49] with a background term multiplied to the exponential term to compensate for the experimental limitations (red solid line). The fit returned $g^{(2)}(0) = 0.08(5)$ and $\Gamma = 2.7(2)$ GHz. (b) The experimental data obtained from Sample 2 was deconvolved with a Gaussian curve with width equal to the timing resolution of the detectors. This data was acquired at high excitation power, consequently the Rabi oscillations are visible. The fit (dashed red line) using [Eq. 3.50] returned $\Omega/\Omega_{sat} = 3.31(5)$ GHz and $\Gamma = 2.17(3)$ GHz.

The $g^{(2)}(\tau)$ function presented in [Fig. 3.27 (a)] was computed from the emission of a QD in the bulk sample (Sample 1) at $P = 0.06P_{sat}$ (black points) and it was fitted using

$$g^{(2)}(\tau) = 1 + Be^{-\Gamma\tau} - 2Be^{-\Gamma\tau/2}\,, \tag{3.49}$$

obtained from [Eq. 3.45] with $\phi = 0$ for $\Omega \ll \Gamma$ and B was included to account for the non-zero $g^{(2)}(0)$ (solid red line). The fit returned $g^{(2)}(0) = 0.08(5)$, which is only limited by the timing resolution of the two SPADs (0.707 ns). Again from the fit, it was estimated $\Gamma = 2.7(2)$ GHz, that is considerably greater than the $\Gamma = 1.63(4)$ GHz reported from the RF power spectrum measurements. This happens because the width of the central inelastic peak in the RF spectrum, from where the Γ is extracted, is more robust against the spectral fluctuations [Fig. 3.18] than the slope of the second-order correlation function [Fig. 3.26].

The data presented in [Fig. 3.27 (b)] (solid black line) is courtesy of Dr. Joanna Zajac, who performed the measurement in the PCA sample with strong spectral fluctuations (Sample 2) and deconvolved with a Gaussian function with width equal to the timing resolution of the combined detectors, which was ~ 50 ps each detector in this case. For the fit (dashed red line), the $g^{(2)}(\tau)$ function was reduced to the case where $\Omega \gg \Gamma$ with $\phi = 0$. So, from

[Eq. 3.45 and 3.46], it is given by

$$g^{(2)}(\tau) = 1 - e^{3\Gamma\tau/4}\cos(\Omega\tau)\ . \tag{3.50}$$

It returned $\Omega = 0.808(3)$ GHz in linear frequency unit, which is responsible for the Rabi oscillations, and a decay rate equal to $\Gamma = 2.17(3)$ GHz.

In this section, we have demonstrated that the QDs from the bulk sample with weak spectral fluctuations (Sample 1) and the PCA device with strong spectral fluctuations (Sample 2) are single-photon sources and that their TLS characteristics are preserved in the second-order correlation function.

Two-photon interference

Indistinguishable single photons are a resource in the development of new technologies [86, 87]. Several reports have been made in this direction exploiting a pair of indistinguishable photons. As examples we have the experimental demonstration of the basic version of the single mode teleportation [88] and a controlled NOT (CNOT) gate operating with indistinguishable single photons [89, 90]. Most research investigating the indistinguishability between two photon uses the HOM interference effect [91] as an indicator. The indistinguishability between photons emitted from semiconductor nanostructures has already been broadly analysed using the quasi-resonant excitation and RF techniques [63, 69, 38, 92, 93, 94, 95, 96, 97, 71]. It was demonstrated that the coherence time of the emission is very important for the degree of indistinguishability [92, 95, 38, 39]. A high degree of indistinguishability can also be achieved with Raman photons [96]. It has also reported that the charge noise can destroy the visibility of the HOM interference, but this obstacle could be overcome by using a weak non-resonant excitation combined with the resonant excitation to prevent the charge dynamics in the QD environment [63].

In this section, the HOM interference measurement from the 'noisy' PCA device (Sample 2) will be presented, showing that high degree of indistinguishability can be achieved in spite of the intrinsic charge noise.

The correlation function from the HOM interference is given by

$$g^2_{\perp}(\tau) = \frac{1}{2}g^2(\tau) + \frac{1}{4}g^2(\tau+\Delta\tau) + \frac{1}{4}g^2(\tau-\Delta\tau) \tag{3.51}$$

$$g^2_{\parallel}(\tau) = \frac{1}{2}g^2(\tau) + \frac{1}{4}g^2(\tau+\Delta\tau) + \frac{1}{4}g^2(\tau-\Delta\tau) - \frac{V_0}{2}\left|g^1(\tau)\right|^2 \tag{3.52}$$

for distinguishable and indistinguishable photons, respectively, under the assumption that the beam splitters are nearly perfect [38]. Here, $\Delta\tau$ is the optical delay and V_0 is a constant accounting for all the imperfection in the experiment, which makes the experimental curve deviate from the ideal situation ($V_0 = 1$). In this experiment, the indistinguishability of the photons was tuned by exploiting their polarisations [Sec. 2.6].

The experimental data is presented in [Fig. 3.28], where an external magnetic field equal to 1 T in the Faraday geometry (X^{1-} transition) was applied in order to minimize the effects of the Overhauser field [Sec. 4.2] and the bias voltage was tuned to bring the higher energy transition to resonance with the driving field. The Rabi frequency used was $\Omega = 0.45(1)\Omega_{sat}$.

One of the consequences of isolating a two-level transition using the Zeeman splitting is that, due to the in-plane Overhauser field, the spin pumping process may occur and its dynamics are also present in the second-order correlation function in the form of a bunching which decays slowly, with a rate inversely proportional to the spin coherence time [77]. The rate in this case is $0.051(4)$ GHz.

Another consequence is that the detuning between the two electron-spin states also contributes to the increase in the slope of $g^{(2)}(\tau)$ at $\tau < 1/\Gamma$, making these measurements more susceptible to the finite timing resolution of the SPADs, which strongly affects the visibility of the interference in the raw experimental data, represented by the red points in [Fig 3.28 (c)]. To take into account the finite resolution of the SPADs, it is necessary to deconvolve the signal with instrument response function, which here is approximated to a Gaussian function with width 0.707 ns for both detectors. The signal, in this work, is the fit of the correlation function (solid green line) and the deconvolved fit is represented by the dashed blue lines in [Fig. 3.28]. The curves for the visibility of the two-photon interference presented in [Fig. 3.28 (c)] are not a fit, but a direct calculation from the correlation functions using

$$\text{visibility}(\tau) = \frac{g_{\perp}^{(2)}(\tau) - g_{\parallel}^{(2)}(\tau)}{g_{\perp}^{(2)}(\tau)}\,, \tag{3.53}$$

from where we get $\text{visibility}(0) = 0.93$ for the deconvolved fit, which is comparable to the visibility achieved using the other samples where the QDs experience weaker spectral fluctuation ($\text{visibility}(0) \approx 0.99$)[77].

With an external magnetic field applied, there is no evidence of Raman photons [Fig. 3.20], therefore, the spectral fluctuations are mainly attributed to the charge noise. At the excita-

tion power where this data was acquired, the spectral fluctuations happen in a form similar to [Fig. 3.23 (a)], where the detuning caused by the QD's environment is much greater than the linewidth of the detuning spectrum and fluctuates in the millisecond timescale. During the correlation measurement, when the random detuning is present, the photon collection almost vanishes [Fig. 3.12 (d)] strongly affecting the number of counts in the histogram built by the TCSPC module, but with minor influence on the visibility of the two-photon interference [Fig. 3.28 (c)]. In this experiment the phonon sideband was not filtered, therefore, we expect that the imperfect deconvolved visibility is due to exciton-phonon interactions.

In summary, in this chapter we have discussed the statistics of photons emitted from an ideal TLS and from an ideal TLS under spectral fluctuations making direct comparisons with experimental data acquired from three different samples with different intensities of spectral fluctuations, but with similar characteristics, with an intriguing but not understood dependence on the excitation power. The quality of the photons was also investigated through RF power spectrum and two-photon interference measurements, from where it could be concluded that the spectral fluctuations increase the fraction of elastically scattered photons and do not affect the indistinguishability of the photons in the specific situation demonstrated here.

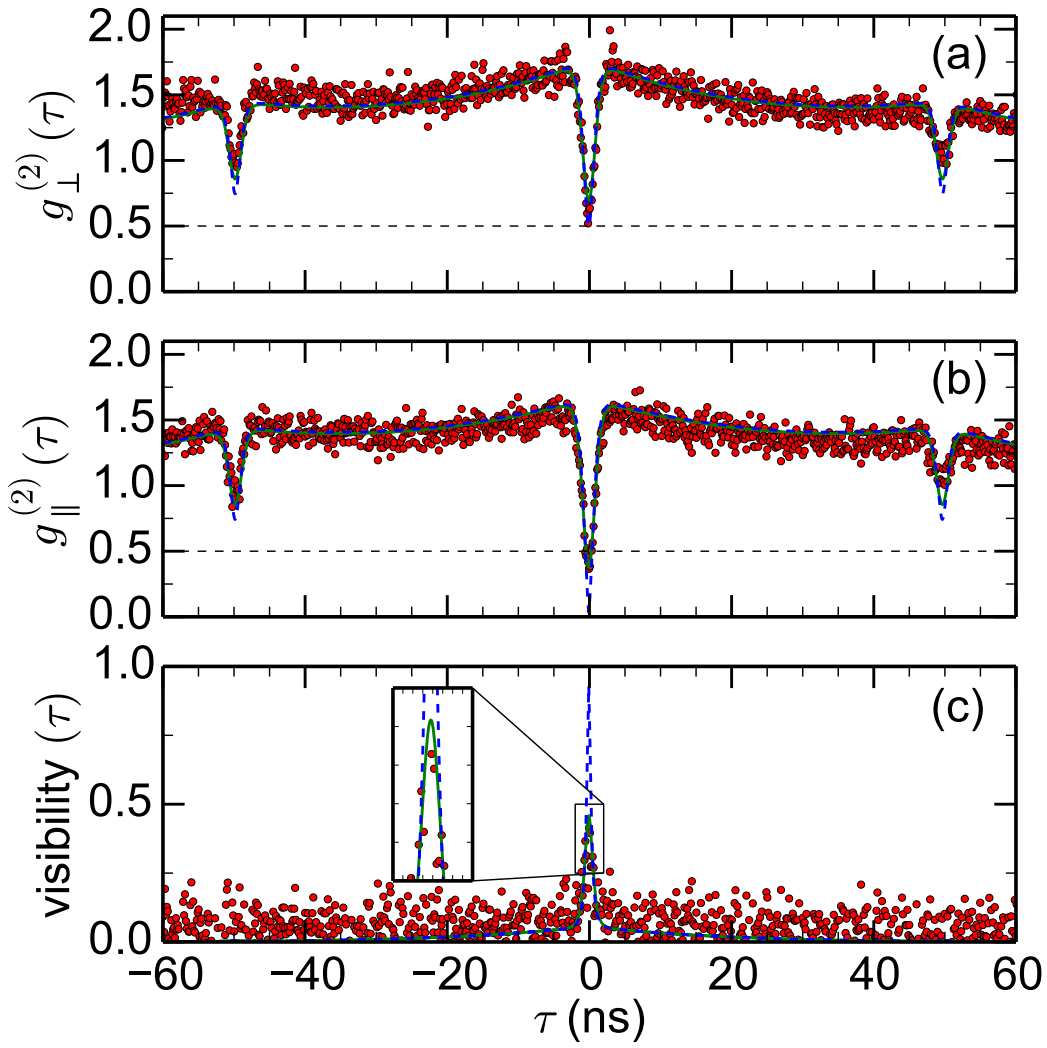

Figure 3.28: **HOM interference measurement using Sample 2.** The polarisation of the interfering photons were tuned to be (a) orthogonal (b) parallel to each other. (c) Visibility of the two-photon interference. In all plots, the red points representing the experimental data, the dashed blue lines are the fits using the equations for an ideal TLS, and the solid green lines are the results of the convolution of the fit with the instrument response function.

Chapter 4

Four-level systems

Optical properties of semiconductor quantum dots

The system studied here consists of a self-assembled QD initially charged with a single electron in the conduction band, which can be obtained through the application of a bias voltage in a charge-tunable device, as discussed in 2.2.

Using a driving EM field we can excite an electron-hole pair, forming an charged exciton also known as trion, with two electrons in the conduction band and a single hole in the valence band. The ability to create the additional electron-hole pair is governed by well defined selection rules, which can be used to manipulate the spin of the confined electron. Therefore, the knowledge of the selection rules is essential. Considering the band structure of a bulk semiconductor of direct gap like GaAs [Fig. 4.1] and InAs, we know that the bottom of the conduction band is composed of s-type states with angular momentum $l = 0$ and the top of the valence band has p-type states with $l = 1$ [98]. This description is a good approximation for semiconductors with direct gap with wave vector about zero, which is in general the case for this kind of material. In the QD case, even though it misses the spherical symmetry we can assume that angular momentum conservation will be satisfied and then we can describe its states in terms of the orbitals just as in an atom. In addition to the angular momentum $\mathbf{L}$, the spin momentum $\mathbf{S}$ of the charge carriers in the valence band and conduction band should be taken into account. Thus, for the valence band whose orbital angular momentum is $l = 1$, the total angular momentum $\mathbf{J} = \mathbf{L} + \mathbf{S}$ will have eigenvalues $j = 3/2$ and $j = 1/2$. For $j = 3/2$ we have the projection in the growth direction $\mathbf{J_z}$ with eigenvalues $m = \pm 3/2$ and $m = \pm 1/2$ which are known as the heavy hole (HH) band and light hole (LH) band, respectively. They have these names due to their effective mass close to the point $k \approx 0$ [98]. We also have $j = 1/2$, with eigenvalues of the projection $\mathbf{J_z}$

equal to $m = \pm 1/2$, forming the split-off band. About the point $k \approx 0$ these states are well separated from the other states due to the spin-orbit interaction, so it can be ignored, while the HH and LH states are degenerate. In self-assembled QDs the HH and LH degeneracy is broken by the stress between the layers of atoms with different lattice parameters [99]. The HH band is the one with higher energy and usually the LH band can be ignored. For the conduction band ($l = 0$) we have only $s = 1/2$ and projections $m = \pm 1/2$.

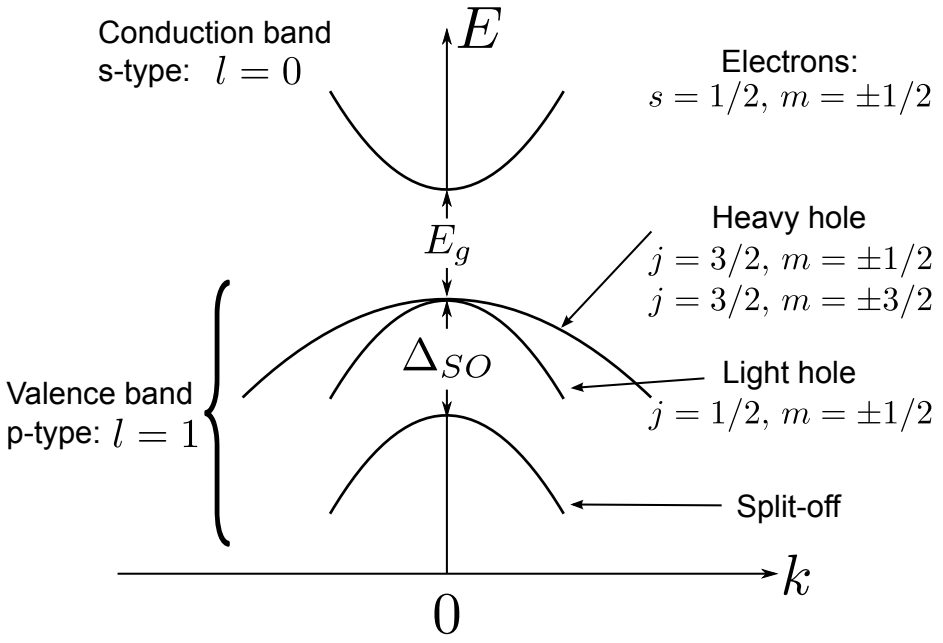

Figure 4.1: **Band structure.** Representation of the band structure of a bulk GaAs. E_g is the gap energy and Δ_{SO} is the energy of the spin-orbit interaction.

In this section we are going to consider only the HH band ($j = 3/2$ and $m = \pm 3/2$) and the conduction band ($s = 1/2$ and $m = \pm 1/2$). In this way, the trion state will be represented by $|\uparrow\downarrow, \Uparrow\rangle$ ($|\uparrow\downarrow, \Downarrow\rangle$) when the state corresponding to $m = 3/2$ ($m = -3/2$) of the HH band is occupied along with the two states of the conduction band ($m = \pm 1/2$). When only a single electron is in the conduction band we will represent it by $|\uparrow\rangle$ ($|\downarrow\rangle$) for $m = 1/2$ ($m = -1/2$).

Along with electric fields, magnetic fields are also very important in the manipulation of the QD states due to its influence in the selection rules, as we will describe in the next section.

Selection rules

Disregarding any band mixing due to the irregular shape of the QD and in the absence of a magnetic field, the two electron spin states are degenerate ($|\uparrow\rangle$ and $|\downarrow\rangle$), just like the two

trion states ($|\uparrow\downarrow,\Uparrow\rangle$ and $|\uparrow\downarrow,\Downarrow\rangle$) [Fig. 4.2] and they have well defined selection rules, associated with the conservation of the angular momentum and the Pauli exclusion principle.

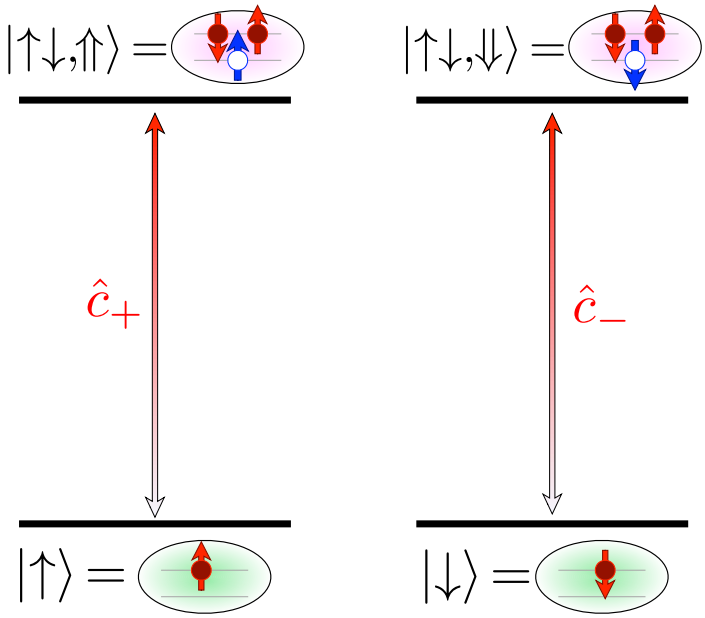

Figure 4.2: **Selection rules for $\tilde{\mathbf{B}} = \tilde{\mathbf{0}}$.** In the absence of a magnetic field the states of the QD are degenerate and the coupling with the EM driving field must follow the selection rules, where different trions can be created with the application of circularly polarised light.

In the dipole approximation the coupling is given by the potential $V = \hat{\epsilon} \cdot \vec{p}$ where $\hat{\epsilon}$ is the vector representing the polarisation of the field and $\vec{p}$ is the linear momentum operator of the electron [99]. Then we can determine the selection rules by calculating the matrix elements $\langle\Psi|\,\hat{\epsilon}\cdot\vec{p}\,|\Psi'\rangle$, which can be rewritten in the following form:

$$\begin{aligned}\langle\Psi|\,\hat{\epsilon}\cdot\vec{p}\,|\Psi'\rangle &\propto \hat{\epsilon}\cdot\langle\Psi|\,[H,\vec{r}]\,|\Psi'\rangle \\ &\propto \hat{\epsilon}\cdot\langle\Psi|\,\vec{r}\,|\Psi'\rangle \end{aligned} \tag{4.1}$$

with $\vec{r} = r\sin(\theta)[\cos(\phi)\hat{x} + \sin(\phi)\hat{y}] + \cos(\theta)\hat{z}$.

Here it is convenient to write the vector $\vec{r}$ as a function of the spherical harmonics $Y_l^m(\theta,\phi)$ which are given by

$$Y_1^{-1}(\theta,\phi) = \frac{1}{2}\sqrt{\frac{3}{2\pi}}\sin(\theta)[\cos(\phi) - i\sin(\phi)] \tag{4.2}$$

$$Y_1^{1}(\theta,\phi) = -\frac{1}{2}\sqrt{\frac{3}{2\pi}}\sin(\theta)[\cos(\phi) + i\sin(\phi)] \tag{4.3}$$

$$Y_1^{0}(\theta,\phi) = \frac{1}{2}\sqrt{\frac{3}{\pi}}\cos(\theta). \tag{4.4}$$

The unitary vector $\hat{r}$, can be written as

$$\hat{r} = \sqrt{\frac{2\pi}{3}}\left\{Y_1^{-1}(\theta,\phi)(\hat{x}+i\hat{y}) + Y_1^{1}(\theta,\phi)(-\hat{x}+i\hat{y})\right\} + 2\sqrt{\frac{\pi}{3}}Y_1^0(\theta,\phi)\hat{z}. \tag{4.5}$$

With

$$\sigma_+ = \frac{\hat{x} + i\hat{y}}{\sqrt{2}} \tag{4.6}$$

$$\sigma_- = \frac{\hat{x} - i\hat{y}}{\sqrt{2}}, \tag{4.7}$$

we have that (4.5) is

$$\hat{r} = 2\sqrt{\frac{\pi}{3}}\left(Y_1^{-1}\sigma_+ - Y_1^1\sigma_- + Y_1^0\hat{z}\right). \tag{4.8}$$

Charge carriers trapped in a QD are well described by a wave function Ψ composed by Bloch functions ψ, which determines the selection rules, along with envelope functions f, which can extend beyond the QD and take information about the geometry of the QD [100]:

$$\Psi_{n,l}^m = A_{n,l} f_{n,l} \psi_l^m \tag{4.9}$$

where A is the normalization constant and the index n corresponds to the possible bands. This approximation, known as the envelope function approximation, is valid for QDs where the effective potential of the specified band varies in a scale of length much greater than the lattice parameter. In this way, the matrix elements are given by

$$\langle \Psi_{n,l}^m | \vec{r} | \Psi_{n',l'}^{m'} \rangle = \langle f_{n,l} | f_{n',l'} \rangle \langle \psi_l^m | \vec{r} | \psi_{l'}^{m'} \rangle + \langle \psi_l^m | \psi_{l'}^{m'} \rangle \langle f_{n,l} | \vec{r} | f_{n',l'} \rangle. \tag{4.10}$$

For the interband transitions, going from one of the electron states to one of the trion states, only the first term of [Eq. 4.10] will contribute:

$$\langle \Psi_{n,l}^m | \vec{r} | \Psi_{n',l'}^{m'} \rangle = \langle f_{n,l} | f_{n',l'} \rangle \langle \psi_l^m | \vec{r} | \psi_{l'}^{m'} \rangle, \tag{4.11}$$

where the second inner product will determine the selection rules and the first term will determine its intensity.

The Bloch functions, for the electron in the conduction band and for the hole in the valence band, can be written in the following way [101]:

$$\psi_l^m = \frac{1}{\sqrt{2l+1}} \begin{pmatrix} \pm\sqrt{l \pm m + \frac{1}{2}}\, Y_l^{m-1/2} \\ \sqrt{l \mp m + \frac{1}{2}}\, Y_l^{m+1/2} \end{pmatrix}. \tag{4.12}$$

Using these functions we can calculate the matrix elements $\langle \Psi | \vec{r} | \Psi' \rangle$ for all possible transitions. Starting with the electron states in the conduction band $|\Psi'\rangle = |\uparrow\rangle$ and the HH in the valence band forming the trion state $\langle \Psi | = \langle \uparrow\downarrow, \Uparrow |$, we have to calculate

$$\langle \uparrow\downarrow, \Uparrow | \vec{r} | \uparrow \rangle = \langle \psi_1^{3/2,3/2} | \vec{r} | \psi_0^{1/2,1/2} \rangle, \tag{4.13}$$

which can be rewritten as:

$$\begin{aligned}\langle\uparrow\downarrow,\Uparrow|\,\vec{r}\,|\uparrow\rangle &= 2r\sqrt{\frac{\pi}{3}}\Bigg(\sigma_+\int_{\theta=0}^{\theta=\pi}\int_{\phi=0}^{\phi=2\pi}\left(Y_1^1\right)^* Y_1^{-1}Y_0^0\sin(\theta)d\theta d\phi + \\ &\quad -\sigma_-\int_{\theta=0}^{\theta=\pi}\int_{\phi=0}^{\phi=2\pi}\left(Y_1^1\right)^* Y_1^1 Y_0^0\sin(\theta)d\theta d\phi + \\ &\quad +\hat{z}\int_{\theta=0}^{\theta=\pi}\int_{\phi=0}^{\phi=2\pi}\left(Y_1^1\right)^* Y_1^0 Y_0^0\sin(\theta)d\theta d\phi\Bigg). \qquad (4.14)\end{aligned}$$

Only the second double integral is different from zero, giving us the result:

$$\langle\uparrow\downarrow,\Uparrow|\,\vec{r}\,|\uparrow\rangle = \frac{-r}{\sqrt{3}}\hat{c}_- \qquad (4.15)$$

Because of the inner product $\vec{r}\cdot\hat{\epsilon}$ that describes the potential responsible for the coupling between the states, we have that only the EM field with circular polarisation couples the states $|\uparrow\rangle$ and $|\uparrow\downarrow,\Uparrow\rangle$. It is important to emphasize that angular momentum must be conserved. Taking the example above, for an initial state with one electron in the conduction band with $m = 1/2$, one photon with angular momentum $m = 1$ can only be absorbed if the final state is a trion with $m = 3/2$, conserving angular momentum. Any other transition via radiation that does not respect the conservation of angular momentum is forbidden. In this case, in the absence of a magnetic field and taking as basis the states in the z-direction $\hat{z}$, we can obtain the coupling between $|\uparrow\rangle$ and $|\uparrow\downarrow,\Uparrow\rangle$ using light with $\hat{c}_+$ polarisation and between the states $|\downarrow\rangle$ and $|\uparrow\downarrow,\Downarrow\rangle$ via light with $\hat{c}_-$ polarisation [Fig. 4.2].

In the presence of a magnetic field, the degeneracy of the spin states is broken through the Zeeman effect and the energy separation for the electron states δ_e is different from the energy separation for the trion states δ_h due to distinct g-factors for electron (g_e) and hole (g_h). The spin states *up* and spin *down* of the electron and of the trion trapped in the QD can now be identified through their energies. The direction of the magnetic field is very important in this case. With the magnetic field applied in the growth direction we have the Faraday geometry, where the states $|\uparrow\rangle$ and $|\uparrow\downarrow,\Uparrow\rangle$ ($|\downarrow\rangle$ and $|\uparrow\downarrow,\Downarrow\rangle$) are separated in energy, but still preserving the selection rules described above, however, the states can now be identified through optical spectroscopy due to the energy difference among them. If we apply a magnetic field in a direction orthogonal to the growth direction (Voigt geometry), along with the broken degeneracy [Fig. 4.3] we also get a superposition of the states, and as a consequence we get a change in the selection rules. Defining

$$|0\rangle = \frac{1}{\sqrt{2}}\left(|\uparrow\rangle + |\downarrow\rangle\right) \qquad (4.16)$$

$$|1\rangle = \frac{1}{\sqrt{2}}\left(-|\uparrow\rangle + |\downarrow\rangle\right) \tag{4.17}$$

$$|2\rangle = \frac{1}{\sqrt{2}}\left(-|\uparrow\downarrow,\Uparrow\rangle + |\uparrow\downarrow,\Downarrow\rangle\right) \tag{4.18}$$

$$|3\rangle = \frac{1}{\sqrt{2}}\left(|\uparrow\downarrow,\Uparrow\rangle + |\uparrow\downarrow,\Downarrow\rangle\right), \tag{4.19}$$

the coupling with radiation can be obtained again by calculating the matrix elements, as in the following example:

$$\begin{aligned}\langle 2|\,\hat{r}\,|0\rangle &= \frac{1}{2}\left(-\langle\uparrow\downarrow,\Uparrow| + \langle\uparrow\downarrow,\Downarrow|\right)\hat{r}\left(|\uparrow\rangle + |\downarrow\rangle\right)\\ &= \frac{r}{2\sqrt{3}}\left(-\hat{c}_- + \hat{c}_+\right)\\ &= \frac{ir}{\sqrt{6}}\hat{y}.\end{aligned} \tag{4.20}$$

Other elements different from zero are:

$$\langle 3|\,\hat{r}\,|0\rangle = \frac{r}{\sqrt{6}}\hat{x} \tag{4.21}$$

$$\langle 2|\,\hat{r}\,|1\rangle = \frac{r}{\sqrt{6}}\hat{x} \tag{4.22}$$

$$\langle 3|\,\hat{r}\,|1\rangle = \frac{ir}{\sqrt{6}}\hat{y}. \tag{4.23}$$

In this way, the application of a magnetic field aligned in the direction $\hat{x}$ allows transitions in the diagonal direction, forbidden in the Faraday geometry, using linearly polarised light.

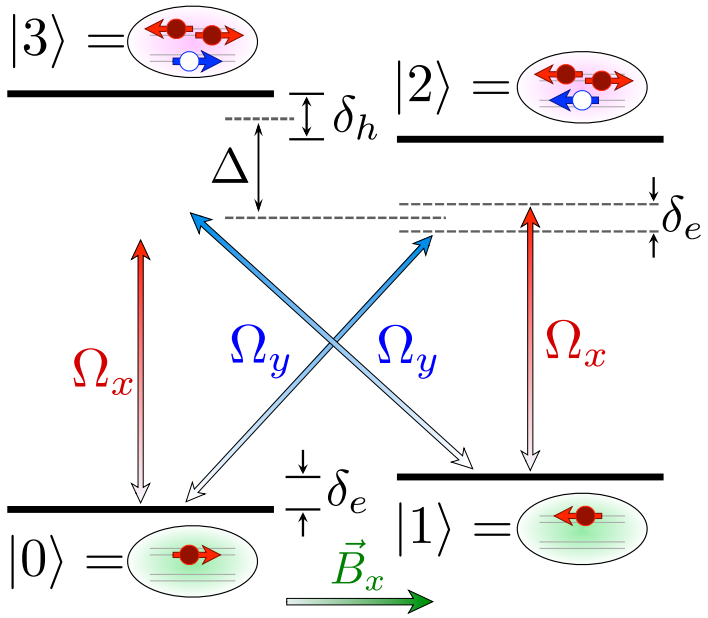

Figure 4.3: **Voigt geometry.** In the presence of magnetic field in the Voigt geometry the states of the QD are not degenerate and the selection rules allow the transitions from any of the lower energy states to any of the trion states by the application of a linearly polarised light.

Overhauser field effects on the X^{1-} transition

The electron and hole wavefunctions of self-assembled III-V quantum dots [2.2] extend over a large number of spin bearing nuclei. The nuclear spins generate an effective magnetic field, called the Overhauser field, that couple with the spins via the hyperfine interaction and can lead to relaxation and dephasing. In the context of the low temperature experiments performed in this manuscript, the "frozen-fluctuation model" [73], in which the nuclear spins are considered to be stationary for a timescale (≈ 1 μs) much greater than the optical transition lifetime (≈ 1 ns), is most relevant for self-assembled quantum dots [56, 74, 75]. In this picture, the electron spin precesses around the hyperfine field on a ns timescale. Here we are interested in changes to the energy levels and selection rules caused by the random Overhauser field orientation. In particular, we develop a theoretical model for predicting the resonance fluorescence spectrum of the photons scattered from the X^{1-} transition of the QD. Our model features four levels, two of those representing the electron spin of the QD's ground state, and the other two the unpaired (heavy) hole spin states of the first excited state.

We let the electron spin levels be Zeeman split by the total magnetic field, i.e. the sum of the externally applied field B_{ext} plus the effective Overhauser contribution B_N (in the frozen fluctuation regime). By contrast, we assume the hole spin only 'sees' the external field that is applied along the $\hat{z}$-direction. (Due to the reduced hole Bloch functions at the nuclear positions, the hyperfine interaction coupling coefficient between a hole and nuclear spins is only ≈ 10 % that of the electron spin coupling coefficient [102, 103]. Further, the hyperfine interaction for an ideal heavy hole takes on an Ising-like form such that heavy hole spin dephasing is greatly suppressed by an in-plane magnetic field [104]). As the basis for our model we adopt the Zeeman eigenstates of both electron and hole (but with respect to different magnetic fields as discussed above), see Fig. 4.4 for a schematic depiction of the relevant level structure.

Writing the total magnetic field $\vec{B} = B_{ext}\hat{z} + \vec{B}_N$ as

$$\vec{B} = B[\sin\theta\cos\phi\hat{x} + \sin\theta\sin\phi\hat{y} + \cos\theta\hat{z}] \tag{4.24}$$

the electron spin Zeeman eigenstates are

$$|+\rangle \;=\; \cos\left(\frac{\theta}{2}\right)|\uparrow\rangle + e^{i\phi}\sin\left(\frac{\theta}{2}\right)|\downarrow\rangle \;, \tag{4.25}$$

$$|-\rangle \;=\; \sin\left(\frac{\theta}{2}\right)|\Uparrow\rangle - e^{i\phi}\cos\left(\frac{\theta}{2}\right)|\Downarrow\rangle \;. \tag{4.26}$$

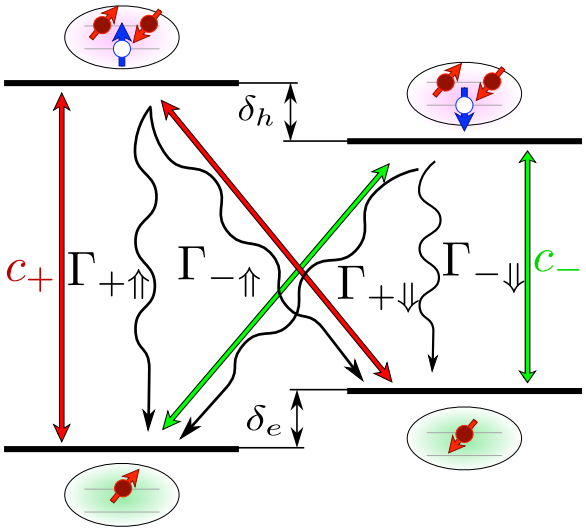

Figure 4.4: The X^{1-} transition under an Overhauser field with an in-plane component. When the total magnetic field is not completely parallel to the growth ($\hat{z}$) direction the electron spin-mixing alters the selection rules and all four transitions become dipole allowed.

Denoting the trion states with hole spin (anti)parallel to the $\hat{z}$-direction as $(|\Downarrow\rangle)$ $|\Uparrow\rangle$, we obtain the following optical dipole transition matrix elements:

$$\langle\Uparrow|\,\vec{r}\,|+\rangle \;\propto\; \cos\left(\frac{\theta}{2}\right)\hat{c}_- \;, \tag{4.27}$$

$$\langle\Downarrow|\,\vec{r}\,|+\rangle \;\propto\; e^{i\phi}\sin\left(\frac{\theta}{2}\right)\hat{c}_+ \;, \tag{4.28}$$

$$\langle\Uparrow|\,\vec{r}\,|-\rangle \;\propto\; \sin\left(\frac{\theta}{2}\right)\hat{c}_- \;, \tag{4.29}$$

$$\langle\Downarrow|\,\vec{r}\,|-\rangle \;\propto\; -e^{i\phi}\cos\left(\frac{\theta}{2}\right)\hat{c}_+ \;, \tag{4.30}$$

where $\hat{c}_\pm$ refers to the two possible circular polarisation states. Including the dependence of the selection rules on the magnetic field direction and under a rotating wave approximation, the system Hamiltonian is then given by

$$\begin{aligned}\frac{H}{\hbar} \;=\; & -\frac{B}{2}|+\rangle\langle+| + \frac{B}{2}|-\rangle\langle-| + \left(\Delta - \frac{B_{ext}}{2}\right)|\Downarrow\rangle\langle\Downarrow| + \left(\Delta + \frac{B_{ext}}{2}\right)|\Uparrow\rangle\langle\Uparrow| \\ & + \frac{\Omega}{2}\sin\left(\frac{\theta}{2}\right)\left(e^{i\phi}\hat{\epsilon}\cdot\hat{c}_+\,|+\rangle\langle\Downarrow| + H.c.\right) + \frac{\Omega}{2}\cos\left(\frac{\theta}{2}\right)\left(\hat{\epsilon}\cdot\hat{c}_-\,|+\rangle\langle\Uparrow| + H.c.\right) \\ & - \frac{\Omega}{2}\cos\left(\frac{\theta}{2}\right)\left(e^{i\phi}\hat{\epsilon}\cdot\hat{c}_+\,|-\rangle\langle\Downarrow| + H.c.\right) + \frac{\Omega}{2}\sin\left(\frac{\theta}{2}\right)\left(\hat{\epsilon}\cdot\hat{c}_-\,|-\rangle\langle\Uparrow| + H.c.\right),\end{aligned} \tag{4.31}$$

where $H.c.$ denotes the Hermitian conjugate, B and B_{ext} are in angular frequency units[1], Ω

[1]For simplicity, the g-factors for the electron and hole were made equal.

is the optical Rabi frequency and Δ the laser detuning from the QD transition in the absence of any magnetic field, and $\hat{\epsilon}$ is a unit vector in the direction of the polarization of the driving laser field.

The selection rules Eqs. (4.27-4.30) also imply spontaneous emission decay channels with polar angle θ dependence as follows

$$\Gamma_{+\Uparrow} = \Gamma \cos^2\left(\frac{\theta}{2}\right) , \tag{4.32}$$

$$\Gamma_{+\Downarrow} = \Gamma \sin^2\left(\frac{\theta}{2}\right) , \tag{4.33}$$

$$\Gamma_{-\Uparrow} = \Gamma \sin^2\left(\frac{\theta}{2}\right) , \tag{4.34}$$

$$\Gamma_{-\Downarrow} = \Gamma \cos^2\left(\frac{\theta}{2}\right) , \tag{4.35}$$

where $\Gamma = 1/T_1$ is the inverse lifetime of the QD. These processes are depicted schematically in Fig. 4.4. Further, we define a lowering operator for each circular polarisation

$$\sigma_-^{(\Downarrow)} = \left(\sqrt{\Gamma_{+\Downarrow}}\,|+\rangle\langle\Downarrow| + \sqrt{\Gamma_{-\Downarrow}}\,|-\rangle\langle\Downarrow|\right)\hat{c}_+ , \tag{4.36}$$

$$\sigma_-^{(\Uparrow)} = \left(\sqrt{\Gamma_{+\Uparrow}}\,|+\rangle\langle\Uparrow| + \sqrt{\Gamma_{-\Uparrow}}\,|-\rangle\langle\Uparrow|\right)\hat{c}_- . \tag{4.37}$$

Using these equations, we can obtain the temporal evolution of the density matrix, given by integrating the master equation

$$\frac{d\rho}{dt} = -\frac{i}{\hbar}[H,\rho] + L(\sigma_-^{(\Uparrow)})\rho + L(\sigma_-^{(\Downarrow)})\rho , \tag{4.38}$$

where $L(\circ)\rho = \circ\rho\,\circ^\dagger - (\circ^\dagger \circ \rho + \rho\,\circ^\dagger\,\circ)/2$ is the standard Lindbladian dissipator.

Writing every element of the master equation, we have

$$\begin{aligned}\frac{d\rho_{++}}{dt} &= -\Omega\left[\sin\left(\frac{\theta}{2}\right)\mathrm{Im}\left[\rho_{+\Downarrow}e^{-i(\phi+\alpha)}\right] + \cos\left(\frac{\theta}{2}\right)\mathrm{Im}\left[\rho_{+\Uparrow}e^{i\alpha}\right]\right] \\ &+ \Gamma_{+\Downarrow}\rho_{\Downarrow\Downarrow} + \Gamma_{+\Uparrow}\rho_{\Uparrow\Uparrow} \qquad (4.39)\\ \frac{d\rho_{--}}{dt} &= \Omega\left[\cos\left(\frac{\theta}{2}\right)\mathrm{Im}\left[\rho_{-\Downarrow}e^{-i(\phi+\alpha)}\right] - \sin\left(\frac{\theta}{2}\right)\mathrm{Im}\left[\rho_{-\Uparrow}e^{i\alpha}\right]\right] \\ &+ \Gamma_{-\Downarrow}\rho_{\Downarrow\Downarrow} + \Gamma_{-\Uparrow}\rho_{\Uparrow\Uparrow} \qquad (4.40)\\ \frac{d\rho_{\Downarrow\Downarrow}}{dt} &= \Omega\left[\sin\left(\frac{\theta}{2}\right)\mathrm{Im}\left[\rho_{+\Downarrow}e^{-i(\phi+\alpha)}\right] - \cos\left(\frac{\theta}{2}\right)\mathrm{Im}\left[\rho_{-\Downarrow}e^{-i(\phi+\alpha)}\right]\right] - \Gamma\rho_{\Downarrow\Downarrow} \qquad (4.41)\\ \frac{d\rho_{\Uparrow\Uparrow}}{dt} &= \Omega\left[\cos\left(\frac{\theta}{2}\right)\mathrm{Im}\left[\rho_{+\Uparrow}e^{i\alpha}\right] + \sin\left(\frac{\theta}{2}\right)\mathrm{Im}\left[\rho_{-\Uparrow}e^{i\alpha}\right]\right] - \Gamma\rho_{\Uparrow\Uparrow} \qquad (4.42)\\ \frac{d\rho_{+-}}{dt} &= -\frac{i\Omega}{2}\left[\cos\left(\frac{\theta}{2}\right)e^{-i\alpha}\left(\rho_{+\Downarrow}e^{-i\phi} + \rho_{\uparrow-}\right) - \sin\left(\frac{\theta}{2}\right)e^{i\alpha}\left(\rho_{+\Uparrow} - \rho_{\Downarrow-}e^{i\phi}\right)\right] \\ &+ iB\rho_{+-} + \sqrt{\Gamma_{+\Downarrow}\Gamma_{-\Downarrow}}\rho_{\Downarrow\Downarrow} + \sqrt{\Gamma_{+\Uparrow}\Gamma_{-\Uparrow}}\rho_{\Uparrow\Uparrow} \qquad (4.43)\end{aligned}$$

$$\frac{d\rho_{+\Downarrow}}{dt} = \frac{\rho_{+\Downarrow}}{2}[i(B - B_{ext} + 2\Delta) - \Gamma] + \frac{i\Omega}{2}e^{i(\phi+\alpha)}\sin\left(\frac{\theta}{2}\right)(\rho_{++} - \rho_{\Downarrow\Downarrow}) - \frac{i\Omega}{2}\cos\left(\frac{\theta}{2}\right)(\rho_{+-}e^{i(\phi+\alpha)} + \rho_{\Uparrow\Downarrow}e^{-i\alpha}) \quad (4.44)$$

$$\frac{d\rho_{+\Uparrow}}{dt} = \frac{\rho_{+\Uparrow}}{2}[i(B + B_{ext} + 2\Delta) - \Gamma] + \frac{i\Omega}{2}e^{-i\alpha}\cos\left(\frac{\theta}{2}\right)(\rho_{++} - \rho_{\Uparrow\Uparrow}) + \frac{i\Omega}{2}\sin\left(\frac{\theta}{2}\right)(\rho_{+-}e^{-i\alpha} - \rho_{\Downarrow\Uparrow}e^{i(\phi+\alpha)}) \quad (4.45)$$

$$\frac{d\rho_{-\Downarrow}}{dt} = \frac{\rho_{-\Downarrow}}{2}[i(2\Delta - B - B_{ext}) - \Gamma] + \frac{i\Omega}{2}e^{i(\phi+\alpha)}\cos\left(\frac{\theta}{2}\right)(\rho_{\Downarrow\Downarrow} - \rho_{--}) + \frac{i\Omega}{2}\sin\left(\frac{\theta}{2}\right)(\rho_{-+}e^{i(\phi+\alpha)} - \rho_{\Uparrow\Downarrow}e^{-i\alpha}) \quad (4.46)$$

$$\frac{d\rho_{-\Uparrow}}{dt} = \frac{\rho_{-\Uparrow}}{2}[i(2\Delta - B + B_{ext}) - \Gamma] + \frac{i\Omega}{2}e^{-i\alpha}\sin\left(\frac{\theta}{2}\right)(\rho_{--} - \rho_{\Uparrow\Uparrow}) + \frac{i\Omega}{2}\cos\left(\frac{\theta}{2}\right)(\rho_{-+}e^{-i\alpha} + \rho_{\Downarrow\Uparrow}e^{i(\phi+\alpha)}) \quad (4.47)$$

$$\frac{d\rho_{\Downarrow\Uparrow}}{dt} = \rho_{\Downarrow\Uparrow}[iB_{ext} - \Gamma] + \frac{i\Omega}{2}e^{-i\alpha}\sin\left(\frac{\theta}{2}\right)(\rho_{\Downarrow-} - \rho_{+\Uparrow}e^{-i\phi}) + \frac{i\Omega}{2}e^{-i\alpha}\cos\left(\frac{\theta}{2}\right)(\rho_{\Downarrow+} + \rho_{-\Uparrow}e^{-i\alpha}) \quad (4.48)$$

For $\Omega \ll \Omega_{sat}$, the diagonal elements of the density matrix are expected to be very small ($\propto \Omega^2$) and, therefore, have minor influence on the temporal evolution of the off-diagonal elements. Assuming $\rho_{\Downarrow\Downarrow}(0) = \rho_{\Uparrow\Uparrow}(0) = \rho_{\Downarrow\Uparrow}(0) = 0$, the solution of the density matrix in the low Rabi frequency regime is given by

$$\rho_{+-}(t) = \rho_{+-}(0)e^{iBt} \quad (4.49)$$

$$\rho_{+\Downarrow}(t) = \left[\rho_{+\Downarrow}(0) - \rho_{+\Downarrow}(\infty) - \rho_{-\Downarrow}(\infty)\frac{\rho_{+-}(0)}{\rho_{--}(0)}\right]\exp\left\{\frac{(iE_{+\Downarrow} - \Gamma)t}{2}\right\} + \rho_{-\Downarrow}(\infty)\frac{\rho_{+-}(0)}{\rho_{--}(0)}\exp\{iBt\} + \rho_{+\Downarrow}(\infty) \quad (4.50)$$

$$\rho_{+\Uparrow}(t) = \left[\rho_{+\Uparrow}(0) - \rho_{+\Uparrow}(\infty) - \rho_{-\Uparrow}(\infty)\frac{\rho_{+-}(0)}{\rho_{--}(0)}\right]\exp\left\{\frac{(iE_{+\Uparrow} - \Gamma)t}{2}\right\} + \rho_{-\Uparrow}(\infty)\frac{\rho_{+-}(0)}{\rho_{--}(0)}\exp\{iBt\} + \rho_{+\Uparrow}(\infty) \quad (4.51)$$

$$\rho_{-\Downarrow}(t) = \left[\rho_{-\Downarrow}(0) - \rho_{-\Downarrow}(\infty) - \rho_{+\Downarrow}(\infty)\frac{\rho_{-+}(0)}{\rho_{++}(0)}\right]\exp\left\{\frac{(iE_{-\Downarrow} - \Gamma)t}{2}\right\} + \rho_{+\Downarrow}(\infty)\frac{\rho_{-+}(0)}{\rho_{++}(0)}\exp\{-iBt\} + \rho_{-\Downarrow}(\infty) \quad (4.52)$$

$$\rho_{-\Uparrow}(t) = \left[\rho_{-\Uparrow}(0) - \rho_{-\Uparrow}(\infty) - \rho_{+\Uparrow}(\infty)\frac{\rho_{-+}(0)}{\rho_{++}(0)}\right]\exp\left\{\frac{(iE_{-\Uparrow} - \Gamma)t}{2}\right\} + \rho_{+\Uparrow}(\infty)\frac{\rho_{-+}(0)}{\rho_{++}(0)}\exp\{-iBt\} + \rho_{-\Uparrow}(\infty)\,, \quad (4.53)$$

where we have defined

$$E_{+\Downarrow} = B - B_{ext} + 2\Delta \tag{4.54}$$

$$E_{+\Uparrow} = B + B_{ext} + 2\Delta \tag{4.55}$$

$$E_{-\Downarrow} = -B - B_{ext} + 2\Delta \tag{4.56}$$

$$E_{-\Uparrow} = -B + B_{ext} + 2\Delta \tag{4.57}$$

and α is related to the direction of the polarisation vector of the driving field through

$$\hat{\epsilon} = \cos(\alpha)\hat{x} + \sin(\alpha)\hat{y}\ . \tag{4.58}$$

Although the initial assumption that the electron spin basis is always in the direction of the total magnetic field eliminates any chance of having $\rho_{+-}(0) \neq 0$, the Eq. [4.49] must not be ignored for the correlation function, where it plays an important role.

The steady state solution for the density matrix is

$$\rho_{+\Downarrow}(\infty) = -\frac{i\Omega e^{i(\alpha+\phi)}\rho_{++}(0)}{iE_{+\Downarrow} - \Gamma}\sin\left(\frac{\theta}{2}\right) \tag{4.59}$$

$$\rho_{+\Uparrow}(\infty) = -\frac{i\Omega e^{-i\alpha}\rho_{++}(0)}{iE_{+\Uparrow} - \Gamma}\cos\left(\frac{\theta}{2}\right) \tag{4.60}$$

$$\rho_{-\Downarrow}(\infty) = \frac{i\Omega e^{i(\alpha+\phi)}\rho_{--}(0)}{iE_{-\Downarrow} - \Gamma}\cos\left(\frac{\theta}{2}\right) \tag{4.61}$$

$$\rho_{-\Uparrow}(\infty) = -\frac{i\Omega e^{-i\alpha}\rho_{--}(0)}{iE_{-\Uparrow} - \Gamma}\sin\left(\frac{\theta}{2}\right) \tag{4.62}$$

$$\rho_{\Downarrow\Downarrow}(\infty) = \frac{\Omega^2\rho_{++}(0)\sin^2\left(\frac{\theta}{2}\right)}{E_{+\Downarrow}^2 + \Gamma^2} + \frac{\Omega^2\rho_{--}(0)\cos^2\left(\frac{\theta}{2}\right)}{E_{-\Downarrow}^2 + \Gamma^2} \tag{4.63}$$

$$\rho_{\Uparrow\Uparrow}(\infty) = \frac{\Omega^2\rho_{++}(0)\cos^2\left(\frac{\theta}{2}\right)}{E_{+\Uparrow}^2 + \Gamma^2} + \frac{\Omega^2\rho_{--}(0)\sin^2\left(\frac{\theta}{2}\right)}{E_{-\Uparrow}^2 + \Gamma^2} \tag{4.64}$$

Resonance fluorescence power spectrum

We proceed to calculate the first-order correlation function $G^{(1)}(\tau) = \langle\sigma_+(t+\tau)\sigma_-(t)\rangle$, which will give us access to the fluorescence spectrum of the photons scattered by this four-level system. In our case we have (due to the two orthogonal polarisations)

$$G^{(1)}(\tau) = \langle\sigma_+^{(\Uparrow)}(t+\tau)\sigma_-^{(\Uparrow)}(t)\rangle + \langle\sigma_+^{(\Downarrow)}(t+\tau)\sigma_-^{(\Downarrow)}(t)\rangle \tag{4.65}$$

$$= \mathrm{Tr}\left[U^-(\tau)\sigma_-^{(\Downarrow)}\rho(\infty)U(\tau)\sigma_+^{(\Downarrow)}\right] + \mathrm{Tr}\left[U^-(\tau)\sigma_-^{(\Uparrow)}\rho(\infty)U(\tau)\sigma_+^{(\Uparrow)}\right] \tag{4.66}$$

with

$$\sigma_-^{(\Downarrow)}\rho(\infty) = \sqrt{\Gamma_h}\left(\rho_{\Downarrow+}(\infty)\,|+\rangle\langle+| + \rho_{\Downarrow-}(\infty)\,|+\rangle\langle-|\right)$$

$$+ \quad \sqrt{\Gamma_v}\left(\rho_{\Downarrow+}(\infty)\,|-\rangle\langle+| + \rho_{\Downarrow-}(\infty)\,|-\rangle\langle-|\right) \tag{4.67}$$

$$\sigma_-^{(\Uparrow)}\rho(\infty) = \sqrt{\Gamma_v}\left(\rho_{\Uparrow+}(\infty)\,|+\rangle\langle+| + \rho_{\Uparrow-}(\infty)\,|+\rangle\langle-|\right)$$

$$+ \quad \sqrt{\Gamma_h}\left(\rho_{\Uparrow+}(\infty)\,|-\rangle\langle+| + \rho_{\Uparrow-}(\infty)\,|-\rangle\langle-|\right)\,, \tag{4.68}$$

where $\Gamma_v = \Gamma_{+\Uparrow} = \Gamma_{-\Downarrow}$ and $\Gamma_h = \Gamma_{+\Downarrow} = \Gamma_{-\Uparrow}$.

Defining

$$\rho^{(\Downarrow)}(\tau) = U^-(\tau)\sigma_-^{(\Downarrow)}\rho(\infty)U(\tau)\,, \tag{4.69}$$

$$\rho^{(\Uparrow)}(\tau) = U^-(\tau)\sigma_-^{(\Uparrow)}\rho(\infty)U(\tau)\,, \tag{4.70}$$

$$G^{(1)}(\tau) = \mathrm{Tr}\left[\rho^{(\Downarrow)}(\tau)\sigma_+^{(\Downarrow)}\right] + \mathrm{Tr}\left[\rho^{(\Uparrow)}(\tau)\sigma_+^{(\Uparrow)}\right] \tag{4.71}$$

$$= \sqrt{\Gamma_h}\rho_{+\Downarrow}^{(\Downarrow)}(\tau) + \sqrt{\Gamma_v}\rho_{-\Downarrow}^{(\Downarrow)}(\tau) + \sqrt{\Gamma_v}\rho_{+\Uparrow}^{(\Uparrow)}(\tau) + \sqrt{\Gamma_h}\rho_{-\Uparrow}^{(\Uparrow)}(\tau) \tag{4.72}$$

and $k_{nm} = \rho_{nm}(\infty)/\rho_{nn}(0)$, the first-order correlation function may be written as

$$\begin{aligned} G^{(1)}(\tau) &= \left[\rho_{\Downarrow\Downarrow}(\infty) - |k_{+\Downarrow}|^2\rho_{++}(0) - |k_{-\Downarrow}|^2\rho_{--}(0)\right]\left[\Gamma_h e^{(iE_{+\Downarrow}-\Gamma)\tau/2} + \Gamma_v e^{(iE_{-\Downarrow}-\Gamma)\tau/2}\right] \\ &+ \left[\rho_{\Uparrow\Uparrow}(\infty) - |k_{+\Uparrow}|^2\rho_{++}(0) - |k_{-\Uparrow}|^2\rho_{--}(0)\right]\left[\Gamma_v e^{(iE_{+\Uparrow}-\Gamma)\tau/2} + \Gamma_h e^{(iE_{-\Uparrow}-\Gamma)\tau/2}\right] \\ &+ \left(\Gamma_v|k_{+\Downarrow}|^2 + \Gamma_h|k_{+\Uparrow}|^2\right)\rho_{++}(0)e^{-iB\tau} + \left(\Gamma_h|k_{-\Downarrow}|^2 + \Gamma_v|k_{-\Uparrow}|^2\right)\rho_{--}(0)e^{iB\tau} \\ &+ \left(\Gamma_h|k_{+\Downarrow}|^2 + \Gamma_v|k_{+\Uparrow}|^2\right)\rho_{++}(0) + \left(\Gamma_v|k_{-\Downarrow}|^2 + \Gamma_h|k_{-\Uparrow}|^2\right)\rho_{--}(0)\,. \end{aligned} \tag{4.73}$$

The amplitude of the damped oscillations in Eq. [4.73] tends to zero for extremely low Rabi frequencies, which can be easily checked using Eqs [4.59-4.64], but, once the number of expected photons differs from the amount of coherently scattered photons, these damped oscillations in the first-order correlation function turn into two peaks located at their respective frequencies, which is relative to the driving field frequency in the present case, and with width completely determined by the decay rate Γ in the power spectrum.

For the purpose of this work, we may rewrite the $G^{(1)}(\tau)$ function as

$$\begin{aligned} G^{(1)}(\tau) &= \left(\Gamma_v|k_{+\Downarrow}|^2 + \Gamma_h|k_{+\Uparrow}|^2\right)\rho_{++}(0)e^{-iB\tau} + \left(\Gamma_h|k_{-\Downarrow}|^2 + \Gamma_v|k_{-\Uparrow}|^2\right)\rho_{--}(0)e^{iB\tau} \\ &+ \left(\Gamma_h|k_{+\Downarrow}|^2 + \Gamma_v|k_{+\Uparrow}|^2\right)\rho_{++}(0) + \left(\Gamma_v|k_{-\Downarrow}|^2 + \Gamma_h|k_{-\Uparrow}|^2\right)\rho_{--}(0)\,. \end{aligned} \tag{4.74}$$

The validity of this approximation, based on the small importance of the population of the excited states, can be analysed by comparing the approximated analytical $G^{(1)}(\tau)$ function [Eq. 4.74] with the numerical solution of the first-order correlation function, without

the approximation under investigation. The function F used for this comparison is given by

$$F = \frac{1}{N}\sum_{\tau}\sqrt{\left(G^{(1)}(\tau) - G_n^{(1)}(\tau)\right)^2} \tag{4.75}$$

where N is the number of points in the temporal evolution and the subscript was included to differentiate the analytical solution from the numerical solution. In [Fig. 4.5 (a)], F can be observed as a function of the Rabi frequency, where $B_N = 250$ MHz, $\theta = \pi/2$, $\Gamma = 1$ GHz and $\rho_{++}(0) = \rho_{--}(0) = 1/2$. The points marked with a green and blue dots are demonstrated in [Fig. 4.5 (b)] and [Fig. 4.5 (c)], respectively, with the dashed black line corresponding to the analytical solution presented in [Eq. 4.74].

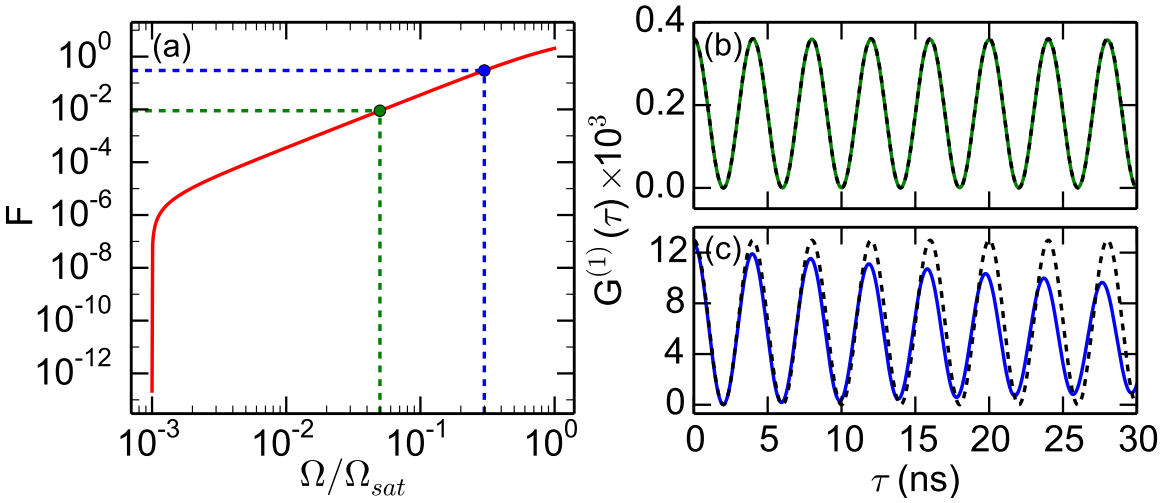

Figure 4.5: **Dependence of the approximation validity on the Rabi frequency.** (a) As the Rabi function increases, the analytical solution differs from the general solution presented by the numerical calculation and F increases. (b) At $\Omega = 0.05\Omega_{sat}$, the approximated solution (dashed black) agrees with the general numerical solution (solid green). (c) At $\Omega = 0.3\Omega_{sat}$ there is a reasonable discrepancy between the approximated solution (dashed black) and the numerical solution (solid blue). Here the parameters used were $\Gamma = 1$ GHz, $B_N = 250$ MHz, $\theta = \pi/2$ and $\rho_{++} = \rho_{--} = 1/2$, and the time resolution of the temporal evolution is 10 ps.

The power spectrum of the resonance fluorescence can be calculated by taking the double of the real part of the Fourier transform of the first-order correlation function

$$\begin{aligned}\frac{S(\omega)}{2} &= \left(\Gamma_v|k_{+\Downarrow}|^2 + \Gamma_h|k_{+\Uparrow}|^2\right)\rho_{++}(0)\delta(\omega + B) + \left(\Gamma_h|k_{-\Downarrow}|^2 + \Gamma_v|k_{-\Uparrow}|^2\right)\rho_{--}(0)\delta(\omega - B) \\ &+ \left(\Gamma_h|k_{+\Downarrow}|^2 + \Gamma_v|k_{+\Uparrow}|^2\right)\rho_{++}(0)\delta(\omega) + \left(\Gamma_v|k_{-\Downarrow}|^2 + \Gamma_h|k_{-\Uparrow}|^2\right)\rho_{--}(0)\delta(\omega)\,. \end{aligned} \tag{4.76}$$

In the absence of an external magnetic field and for $\Delta = 0$ MHz, the measurement of a single power spectrum at temperature $T \sim 4$ K can be simulated using $\rho_{++}(0) = \rho_{--}(0) =$

$1/2$. In these conditions, the power spectrum is given by

$$S(\omega) = \frac{\Omega^2\Gamma}{B_N^2 + \Gamma^2}\left\{\left[1+\cos^2\theta\right]\delta(\omega) + \frac{\sin^2(\theta)}{2}\left[\delta(\omega - B_N) + \delta(\omega + B_N)\right]\right\} . \quad (4.77)$$

In [Eq. 4.77], it can be observed that the Raman process is responsible for up to 50% of the photon scattering, with the maximal achieved at $\theta = \pi/2$, when all the transitions have equal intensity. From the same equation, it can also be observed that only the distribution of the photons over the frequency domain depends on the orientation of the Overhauser field, while the total number of photons remains constant, as expected.

In [Fig. 4.6], the normalised spectra for different values of θ are presented, where the delta peaks were converted into Lorentzian peaks with width equal to the spectral resolution of the instrument used in the experiments, which is ~ 27.5 MHz. In the Faraday geometry ($\theta = 0$), only the central peak is observed [Fig. 4.6 (a)], but as θ is increased, the Raman peaks, also converted into Lorentzian peaks, appear [Fig. 4.6 (b)], achieving their maximal intensity in the Voigt geometry ($\theta = \pi/2$) [Fig. 4.6 (c)].

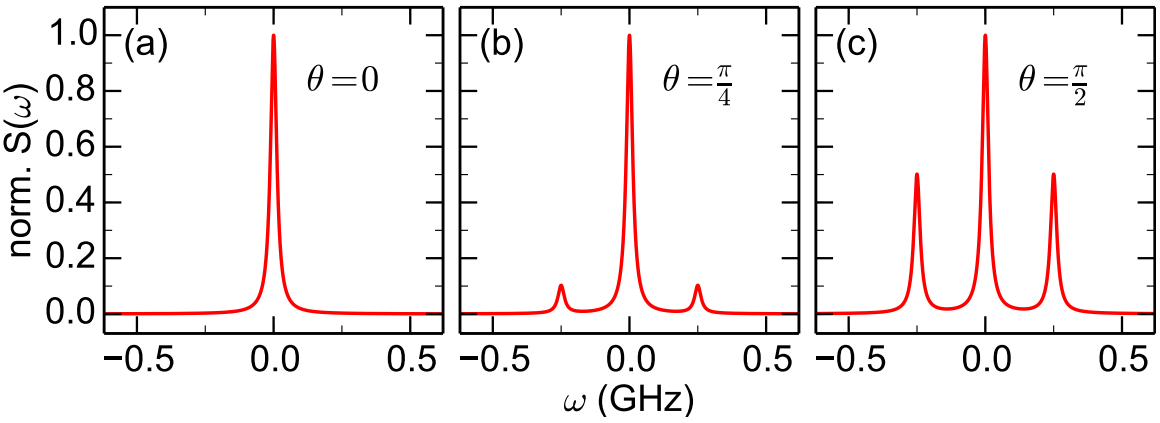

Figure 4.6: **Resonance fluorescence spectra with fixed Overhauser fields for $\mathbf{B_{ext} = \Delta = 0}$ MHz.** (a) In the Faraday geometry with low Rabi frequency $\Omega = 0.01\Omega_{sat}$, only elastically scattered photons are expected. (b) $\theta = \pi/4$ and $\Omega = 0.01\Omega_{sat}$. The two side peaks at $\pm\delta_e$ ($B_N = 250$ MHz) are due to Raman scattered photons (broadened to the interferometer resolution). (c) Voigt geometry with other parameters as in (b): the Raman transitions reach maximal intensity in this configuration.

To reproduce the long time measurements, it is necessary to average several spectra with different instantaneous nuclear fields $\vec{B}_N$. Considering that the Overhauser field has no preferential direction, we will realise $\langle\vec{B}_N\rangle = \vec{0}$ (as required) upon performing uniform averaging over the solid angle.

$$\langle S(\omega)\rangle_{\theta,\phi} = \int_0^{2\pi}\int_0^{\pi} S(\omega)\sin\theta d\theta d\phi \quad (4.78)$$

$$\langle S(\omega)\rangle_{\theta,\phi} = \frac{4\pi\Omega^2\Gamma}{3(B_N^2+\Gamma^2)}\left[4\delta(\omega)+\delta(\omega+B_N)+\delta(\omega-B_N)\right] . \tag{4.79}$$

It remains to specify a radial distribution of B_N to represent the magnitudes of the instantaneous Overhauser fields. We consider the case of a normal distribution with generally finite mean $\langle B_N\rangle$ and variance δB_N.

$$\langle S(\omega)\rangle_{B_N,\theta,\phi} = \int_0^\infty \langle S(\omega)\rangle_{\theta,\phi} N \exp\left(-\frac{(B_N-\langle B_N\rangle)^2}{2\delta B_N^2}\right) dB_N \tag{4.80}$$

$$\begin{aligned}\langle S(\omega)\rangle_{B_N,\theta,\phi} &= \frac{4\pi\Omega^2\Gamma N}{3}\left\{4\delta(\omega)\int_0^\infty \frac{1}{B_N^2+\Gamma^2}\exp\left(-\frac{(B_N-\langle B_N\rangle)^2}{2\delta B_N^2}\right) dB_N\right. \\ &+ \left.\int_0^\infty \frac{[\delta(\omega-B_N)+\delta(\omega+B_N)]}{B_N^2+\Gamma^2}\exp\left(-\frac{(B_N-\langle B_N\rangle)^2}{2\delta B_N^2}\right) dB_N\right\}\end{aligned} \tag{4.81}$$

$$\begin{aligned}\langle S(\omega)\rangle_{B_N,\theta,\phi} &= \frac{4\pi\Omega^2\Gamma N}{3}\left\{4\delta(\omega)\int_0^\infty \frac{1}{B_N^2+\Gamma^2}\exp\left(-\frac{(B_N-\langle B_N\rangle)^2}{2\delta B_N^2}\right) dB_N\right. \\ &+ \left.\frac{1}{\omega^2+\Gamma^2}\left[\exp\left(-\frac{(\omega-\langle B_N\rangle)^2}{2\delta B_N^2}\right)+\exp\left(-\frac{(\omega+\langle B_N\rangle)^2}{2\delta B_N^2}\right)\right]\right\}\end{aligned} \tag{4.82}$$

where N is the normalisation factor of the probability distribution.

For $\langle B_N\rangle = 0$ the difference between the energy of the Raman scattered and the Rayleigh photons is typically small, and consequently the average over the Raman peaks yields a single Gaussian envelope of width proportional to δB_N [Fig. 4.7 (a)]. By contrast a finite mean $\langle B_N\rangle > 0$ separates the Rayleigh from the Raman peaks, leading to two shifted Gaussian Raman envelopes either side of the central elastic peak [Fig. 4.7 (b)]. This latter case gives very close agreement with our measured spectra shown in [Fig. 4.7 (c)].

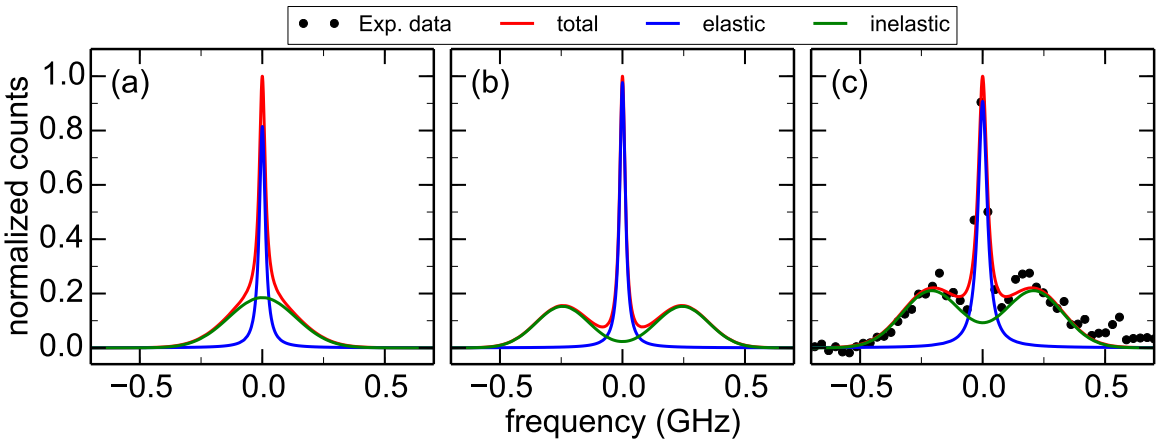

Figure 4.7: **Resonance fluorescence spectrum averaged over a fluctuating Overhauser field.** Here the parameters are $\Gamma = 1.33$ GHz, $\Omega = 0.01\Omega_{sat}$, $B_{ext} = 0$ MHz, and an isotropic angular distribution of the Overhauser field throughout. (a) $\langle B_N \rangle = 0$ MHz and $\delta B_N = 200$ MHz: the Raman peak envelope forms a single Gaussian with width proportional to δB_N. (b) $\langle B_N \rangle = 300$ MHz and $\delta B_N = 100$ MHz: the Raman peak envelopes can be resolved separately either side of the central elastic peak. (c) Our averaged full simulation of the spectrum with $\langle B_N \rangle = 264$ MHz and $\delta B_N = 113$ MHz provides an equally good fit to the experimental data as directly fitting (i.e. without underlying calculation of the spectrum) two Gaussian peaks with mean $0.208(5)$ MHz and standard deviation $0.114(6)$ MHz plus a Lorentzian peak with mean equal to 0 MHz and width equal to 27.5 MHz (FPI resolution).

Another relevant case to be analysed is when the external field is different from zero and the driving field is tuned on resonance with one of the optical transitions of the Faraday geometry. For example, if the driving field is on resonance with the transition from $|+\rangle$ to $|\Uparrow\rangle$, i.e., $\Delta = -(B_{ext} + B)/2$, the spectrum can be written as

$$\begin{aligned}
\frac{S(\omega)}{2} &= \left[\frac{\Gamma_v\Omega^2}{4B_{ext}^2+\Gamma^2} + \frac{\Gamma_h\Omega^2}{\Gamma^2}\right]\rho_{++}(0)\delta(\omega+B) \\
&+ \left[\frac{\Gamma_h\Omega^2}{4(B_{ext}+B)^2+\Gamma^2} + \frac{\Gamma_v\Omega^2}{4B^2+\Gamma^2}\right]\rho_{--}(0)\delta(\omega-B) \\
&+ \left[\frac{\Gamma_h\Omega^2}{4B_{ext}^2+\Gamma^2} + \frac{\Gamma_v\Omega^2}{\Gamma^2}\right]\rho_{++}(0)\delta(\omega) \\
&+ \left[\frac{\Gamma_v\Omega^2}{4(B_{ext}+B)^2+\Gamma^2} + \frac{\Gamma_v\Omega^2}{4B^2+\Gamma^2}\right]\rho_{--}(0)\delta(\omega)\,. \qquad (4.83)
\end{aligned}$$

For $B_{ext} \gg B_N$, we have that $B \sim B_{ext}$, $\theta \sim 0$ and, consequently, $\Gamma_h \sim 0$ and $\Gamma_v \sim \Gamma$, so,

$$\begin{aligned}
\frac{S(\omega)}{2} &= \frac{\Gamma\Omega^2\rho_{++}(0)}{4B^2+\Gamma^2}\delta(\omega+B) + \frac{\Gamma\Omega^2\rho_{--}(0)}{4B^2+\Gamma^2}\delta(\omega-B) \\
&+ \left[\frac{\Omega^2\rho_{++}(0)}{\Gamma} + \frac{\Gamma\Omega^2\rho_{--}(0)}{16B^2+\Gamma^2}\right]\delta(\omega)\,. \qquad (4.84)
\end{aligned}$$

If B_{ext} is also much greater than the decay rate, then

$$S(\omega) = \frac{2\Omega^2\rho_{++}(0)}{\Gamma}\delta(\omega) \qquad (4.85)$$

and the TLS behaviour is recovered. The recovery of the purely elastic scattering in spite of the presence of the nuclear field is important, since it is one of the reasons behind the degradation of the visibility of two-photon interference measurements [77].

Second-order correlation function

In this section, the effects of the Overhauser field and its fluctuation on the second-order correlation function in the low Rabi frequency regime will be investigated.

The un-normalised second-order correlation function $G^{(2)}(\tau)$ is written as

$$G^{(2)} = \langle \sigma_+(t)\sigma_+(t+\tau)\sigma_-(t+\tau)\sigma_-(t)\rangle \,, \tag{4.86}$$

with the normalised second-order correlation function $g^{(2)}(\tau)$ given by

$$g^{(2)}(\tau) = \frac{G^{(2)}(\tau)}{|G^{(1)}(0)|^2} \,. \tag{4.87}$$

Again due to the orthogonal polarisation of the optical transitions, this correlation function may be rewritten as

$$\begin{aligned} G^{(2)} &= \langle \sigma_+^{(\Uparrow)}(t)\sigma_+^{(\Downarrow)}(t+\tau)\sigma_-^{(\Uparrow)}(t+\tau)\sigma_-^{(\Downarrow)}(t)\rangle + \langle \sigma_+^{(\Uparrow)}(t)\sigma_+^{(\Downarrow)}(t+\tau)\sigma_-^{(\Downarrow)}(t+\tau)\sigma_-^{(\Uparrow)}(t)\rangle \\ &+ \langle \sigma_+^{(\Downarrow)}(t)\sigma_+^{(\Uparrow)}(t+\tau)\sigma_-^{(\Uparrow)}(t+\tau)\sigma_-^{(\Downarrow)}(t)\rangle + \langle \sigma_+^{(\Downarrow)}(t)\sigma_+^{(\Uparrow)}(t+\tau)\sigma_-^{(\Downarrow)}(t+\tau)\sigma_-^{(\Uparrow)}(t)\rangle \end{aligned} \tag{4.88}$$

$$\begin{aligned} G^{(2)} &= \mathrm{Tr}\left[U^-(\tau)\sigma_-^{(\Downarrow)}\rho(\infty)\sigma_+^{(\Uparrow)}U(\tau)\sigma_+^{(\Downarrow)}\sigma_-^{(\Uparrow)}\right] + \mathrm{Tr}\left[U^-(\tau)\sigma_-^{(\Uparrow)}\rho(\infty)\sigma_+^{(\Uparrow)}U(\tau)\sigma_+^{(\Downarrow)}\sigma_-^{(\Downarrow)}\right] \\ &+ \mathrm{Tr}\left[U^-(\tau)\sigma_-^{(\Downarrow)}\rho(\infty)\sigma_+^{(\Downarrow)}U(\tau)\sigma_+^{(\Uparrow)}\sigma_-^{(\Uparrow)}\right] + \mathrm{Tr}\left[U^-(\tau)\sigma_-^{(\Uparrow)}\rho(\infty)\sigma_+^{(\Downarrow)}U(\tau)\sigma_+^{(\Uparrow)}\sigma_-^{(\Downarrow)}\right] \end{aligned} \tag{4.89}$$

With $\rho_{\Downarrow\Uparrow}(\infty) = \rho_{\Uparrow\Downarrow}(\infty) = 0$, all the elements of $\sigma_-^{(\Downarrow)}\rho(\infty)\sigma_+^{(\Uparrow)}$ and $\sigma_-^{(\Uparrow)}\rho(\infty)\sigma_+^{(\Downarrow)}$ are zero. So,

$$G^{(2)} = \mathrm{Tr}\left[U^-(\tau)\sigma_-^{(\Uparrow)}\rho(\infty)\sigma_+^{(\Uparrow)}U(\tau)\sigma_+^{(\Downarrow)}\sigma_-^{(\Downarrow)}\right] + \mathrm{Tr}\left[U^-(\tau)\sigma_-^{(\Downarrow)}\rho(\infty)\sigma_+^{(\Downarrow)}U(\tau)\sigma_+^{(\Uparrow)}\sigma_-^{(\Uparrow)}\right] \tag{4.90}$$

with

$$\sigma_-^{(\Uparrow)}\rho(\infty)\sigma_+^{(\Uparrow)} = \rho_{\Uparrow\Uparrow}(\infty)\left[\Gamma_v\,|+\rangle\langle+| + \sqrt{\Gamma_v\Gamma_h}\,(|+\rangle\langle-| + |-\rangle\langle+|) + \Gamma_h\,|-\rangle\langle-|\right] \tag{4.91}$$

$$\sigma_-^{(\Downarrow)}\rho(\infty)\sigma_+^{(\Downarrow)} = \rho_{\Downarrow\Downarrow}(\infty)\left[\Gamma_h\,|+\rangle\langle+| + \sqrt{\Gamma_v\Gamma_h}\,(|+\rangle\langle-| + |-\rangle\langle+|) + \Gamma_v\,|-\rangle\langle-|\right] \tag{4.92}$$

Writing $\rho^{(a)}(\tau) = U^-(\tau)\sigma_-^{(a)}\rho(\infty)\sigma_+^{(a)}U(\tau)$, we have that

$$G^{(2)}(\tau) = \Gamma\left[\rho_{\Downarrow\Downarrow}^{(\Uparrow)}(\tau) + \rho_{\Uparrow\Uparrow}^{(\Downarrow)}(\tau)\right] \,. \tag{4.93}$$

The temporal evolution of the excited states can be calculated by replacing the off diagonal elements [Eqs. 4.50-4.53] in [Eqs. 4.41-4.42], as presented in [Appendix B].

For $\Delta = 0$ MHz, $\rho_{++}(0) = \rho_{--}(0) = 1/2$ and in the absence of an external magnetic field, the $g^{(2)}(\tau)$ function is

$$g^{(2)}(\tau) = 1 + e^{-\Gamma t} - 2\cos\left(\frac{B_N t}{2}\right) e^{-\Gamma t/2}\,, \tag{4.94}$$

from where it can be concluded that the intensity correlation function does not depend on the orientation of the Overhauser field, but only on the detuning it causes through the Zeeman splitting. As it can be easily checked in [Eq. 4.94], for $B_N = 0$ MHz and under the conditions already cited, the four-level system will present an intensity correlation function equal to the correlation of a TLS under the same conditions. But, if $B_N \neq 0$ MHz, the presence of the Overhauser field affects the slope of the curve and originates a bunching for modest values [Fig. 4.8 (a)].

To simulate long time measurements, it is necessary to integrate $g^{(2)}(\tau)$ over a normal distribution. So, it is given by

$$\langle g^{(2)}(\tau)\rangle_{B_N} = 1 + e^{-\Gamma t} - 2e^{-\Gamma t/2}\int_0^\infty \cos\left(\frac{B_N t}{2}\right) n(B_N, \langle B_N\rangle, \delta B_N) dB_N\,, \tag{4.95}$$

where $n(B_N, \langle B_N\rangle, \delta B_N)dB_N$ is the normal distribution with mean $\langle B_N\rangle$ and deviation δB_N.

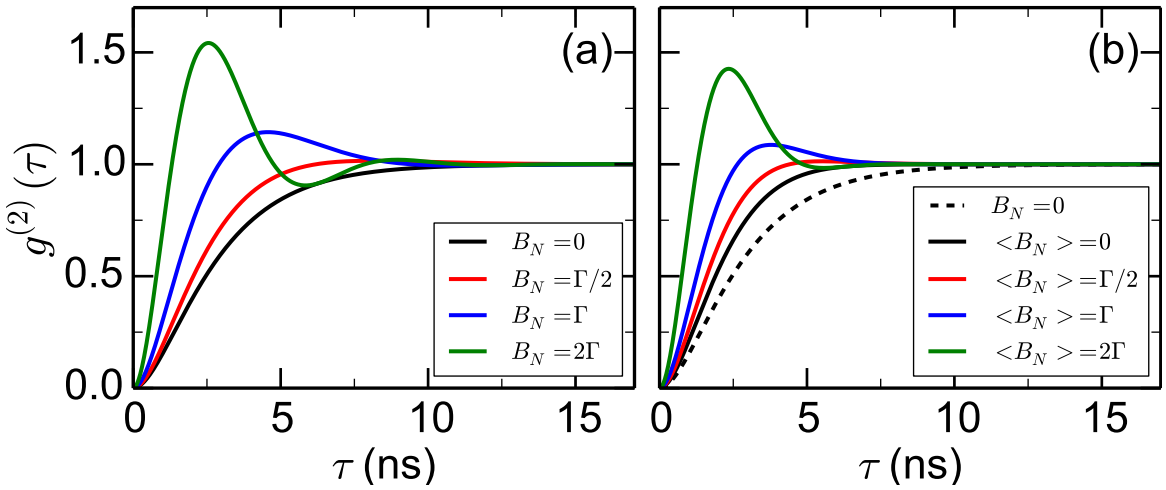

Figure 4.8: $\mathbf{g^{(2)}(\tau)}$ **function under the influence of the Overhauser field.** (a) With $\Gamma = 1$ GHz, a constant Overhauser field affects the slope of the curve and originates a bunching for modest values. (b) When the $g^{(2)}(\tau)$ function is averaged to simulate a long time measurement, the slope is affected even for $\langle B_N\rangle = 0$ MHz (black solid line) and the bunching is slightly decreased. The correlation with $B_N = 0$ MHz (black dashed line) was introduced for comparison and the standard deviation for the Overhauser field is $\delta B_N = 200\pi$ MHz in angular frequency unit.

In [Fig. 4.8 (b)] it is possible to observe that the slope of the curve deviates from the ideal (black dashed line) even with $\langle B_N \rangle = 0$ MHz (black solid line). In this sense, when there is a considerable interaction between the nuclear field and the quantum system, the second-order correlation function under low Rabi frequency cannot be used as a precise measurement of the decay rate.

In order to account for the non-zero $g^{(2)}(0)$ due to the response time of detection, it is necessary to include another parameter K in [Eq. 4.95], so that it reads

$$\langle g^{(2)}(\tau) \rangle_{B_N} = 1 + (1 - K) \left[e^{-\Gamma t} - 2e^{-\Gamma t/2} \int_0^\infty \cos\left(\frac{B_N t}{2}\right) n(B_N, \langle B_N \rangle, \delta B_N) dB_N \right] . \tag{4.96}$$

In [Fig. 4.9] it can be noticed that the slope of the simulated $g^{(2)}(\tau)$ function matches the slope of the experimental $g^{(2)}(\tau)$ function measured in the low Rabi frequency regime. In this case, the parameters used come from the fit in [Fig. 4.7 (c)], which are $\langle B_N \rangle = 1.659$ GHz and $\delta B_N = 0.754$ GHz, and the decay rate $\Gamma = 1.33$ GHz measured by Dr. Ralph N. E. Malein through the ratio between the elastically scattered photons and the total amount of photons under a modest external magnetic field in the growth direction (red solid line). The bunching at $\sim$ 2 ns is also present in both plots, but the decay from the bunching until $g^{(2)}(\tau) = 1$ is not covered by this model. Possible explanations are the not included incoherent spin flip and the not considered finite value of the laser coherence time. The expected $g^{(2)}(\tau)$ function without the effect of the Overhauser field can also be observed in [Fig. 4.9 (dashed blue line)].

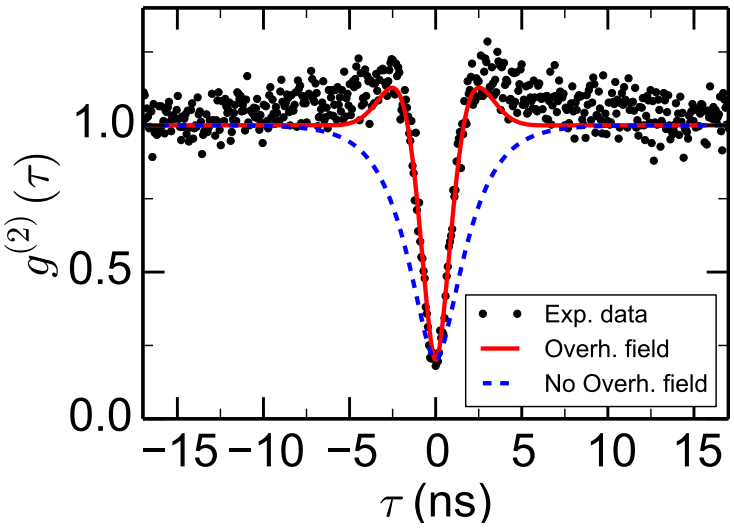

Figure 4.9: **Experimental $g^{(2)}(\tau)$ function and its correspondent simulation.** (black dots) The experimental $g^{(2)}(\tau)$ function acquired with no external field applied in the low Rabi frequency regime. (red solid line) Simulation of the $g^{(2)}(\tau)$ function using the parameters from the fit in [Fig. 4.7 (c)], which are $\langle B_N \rangle = 1.659$ GHz and $\delta B_N = 0.754$ GHz, and the decay rate $\Gamma = 1.33$ GHz measured by Dr. Ralph N. E. Malein through the ratio between the elastically scattered photons and the total amount of photons under a modest external magnetic field in the growth direction. (dashed blue line) The simulation of the $g^{(2)}(\tau)$ function not taking into account the effects of the Overhauser field for $\Gamma = 1.33$ GHz.

In this chapter, it was discussed the optical properties of semiconductor quantum dots, as well as the selection rules for the negatively charged exciton transition. The selection rules are crucial for the understanding of the effects of the Overhauser field on the resonance fluorescence signal from the X^{1-} optical transitions. The effects of the nuclear field on the first-order correlation function was investigated for the case of low excitation power ($\Omega \ll \Omega_{sat}$) and a comparison between the model and an experimental result was presented for the related power spectrum, from where it was concluded that the average magnitude of the nuclear field is ~ 264 MHz with a deviation of ~ 113 MHz. It was also concluded that the second-order correlation function is affected by the Overhauser field, which leads to a considerable change on the slope of the antibunching dip and the appearance of an oscillating term. As a continuity to this work, a theoretical study about the effects of the nuclear field on the two-photon interference measured using the HOM interferometer will be investigated.

Chapter 5

Quantum dots near a metal surface

This chapter describes the investigation of some effects of a metal surface (Au), present in both PCA devices (Sample 2 and Sample 3), in close proximity to the quantum dots. These effects are observed in resonant excitation and appear to be caused by an image dipole induced on the metal surface. I will present the experimental observations and discuss the possible cause of the effect with a theoretical model which leads to a good degree of quantitative agreement. Following these preliminary results, further experiments will be suggested that can lead to a complete understanding of the coupling between a quantum dot and nearby metal mirror. Here, the X^{1-} optical transitions of the QDs are considered TLSs, even in the absence of an external magnetic field and for linearly polarised excitation field. In the theoretical analysis, the effects of the charge noise and Overhauser field on the photon counting statistics and selection rules of the X^{1-} transition are put aside for simplicity.

As discussed in [Sec. 2.2], the Au mirror was introduced in the samples to reflect the fraction of photons that the QD emits in the direction opposite to the objective lens of the microscope and to shape the far-field radiation pattern for optimised collection efficiency [Fig. 2.1]. The distance between the metal surface and the QD layer d_{qd-i} was optimised by Dr. Yong Ma using FDTD simulations and an analytical analysis in order to get the best extraction efficiency possible, resulting in $d_{qd-i} = 176.6\ (196.6)$ nm for Sample 2 (3).

Experimental $\mathbf{g^{(2)}(\tau)}$ of a QD near a gold surface

In this section, we will discuss the experimental results of the second-order correlation function measured using the photons emitted by a QD and its image on a gold surface. In order to analyse the $g^{(2)}(\tau)$ at relatively long timescales (microseconds), the photon counting was performed in the time-tagged mode of PicoHarp [Appendix A], where the

arrival times of photons were recorded for post-processing.

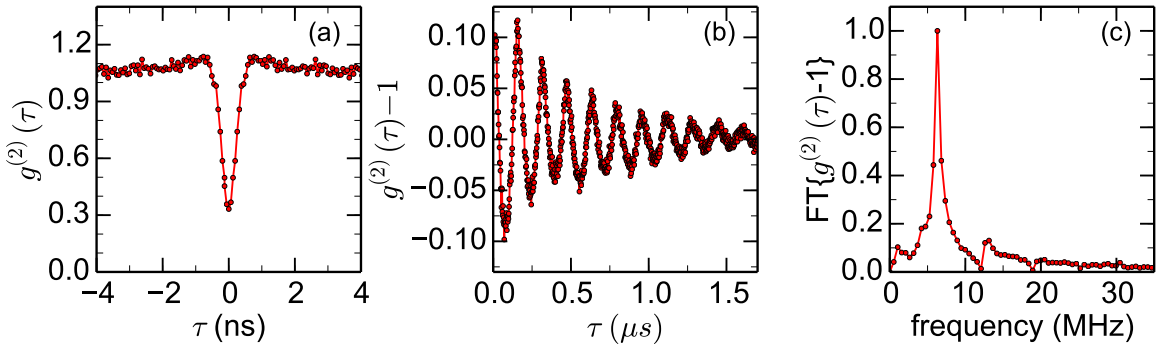

Figure 5.1: **Second-order correlation function of a TLS near a metal.** (a) The $g^{(2)}(\tau)$ for small τ is dominated by the photon emission of the QD, which has $\Gamma_{QD} = 1.5$ GHz, extracted from power spectrum measurements. In this case $\Omega_{QD} = 0.111(7)\Omega_{QD}^{sat}$. The small bunching observed is caused by the spectral fluctuations, similar to [Fig. 4.9]. (b) Oscillations caused by the interaction between the QD and the metal surface with frequency 12.8π MHz and decay rate of 2 MHz. (c) Fourier transform of $g^{(2)}(\tau) - 1$ presented in (b) used to facilitate the extraction of the frequency of oscillation and decay rate.

In [Fig. 5.1], we can observe the experimental data acquired using the 'noisy' PCA device with a gold mirror placed ~ 176.6 nm away from the QD layer (Sample 2) [Sec. 2.2] for a Rabi frequency equal to $0.111(7)\Omega_{QD}^{sat}$. The time bin of the experimental data is $T_{bin} = 0.064$ ns in [Fig. 5.1 (a)], where the usual antibunching curve is observed when τ is comparable to the QD lifetime. In [Fig. 5.1 (b)], the time bin used was $T_{bin} = 2$ ns and an oscillation with frequency $\Omega_i = 12.8\pi$ MHz and decay rate $\Gamma_i = 2$ MHz is observed due to the interaction between the QD and the mirror, which is not present in the second-order correlation function measurements performed using the bulk sample (Sample 1).

It was observed that the coherence time and frequency of the oscillations depend on the power of the driving field [Fig. 5.2], which is tuned using a neutral density filter [Sec. 2.1], so no change in the coherence time of the laser is expected. The coherence time has a linear dependence on the Rabi frequency [Fig 5.3 (a)], while the frequency of the oscillations exhibits a small alteration which, in the range measured, depends exponentially on Ω_{QD} [Fig 5.3 (b)]. The numbers presented were extracted from fits of the data presented in [Fig. 5.2] using

$$g^{(2)}(\tau) - 1 = B\cos(\Omega_i\tau)e^{-3\Gamma_i\tau/4}\,, \tag{5.1}$$

where the factor $3/4$ was included in the exponential term to make the equation identical to the intensity correlation function of a TLS for $\Omega_i >> \Gamma_i$, where B is a constant to account for the fact that $g^{(2)}(0) \neq 0$.

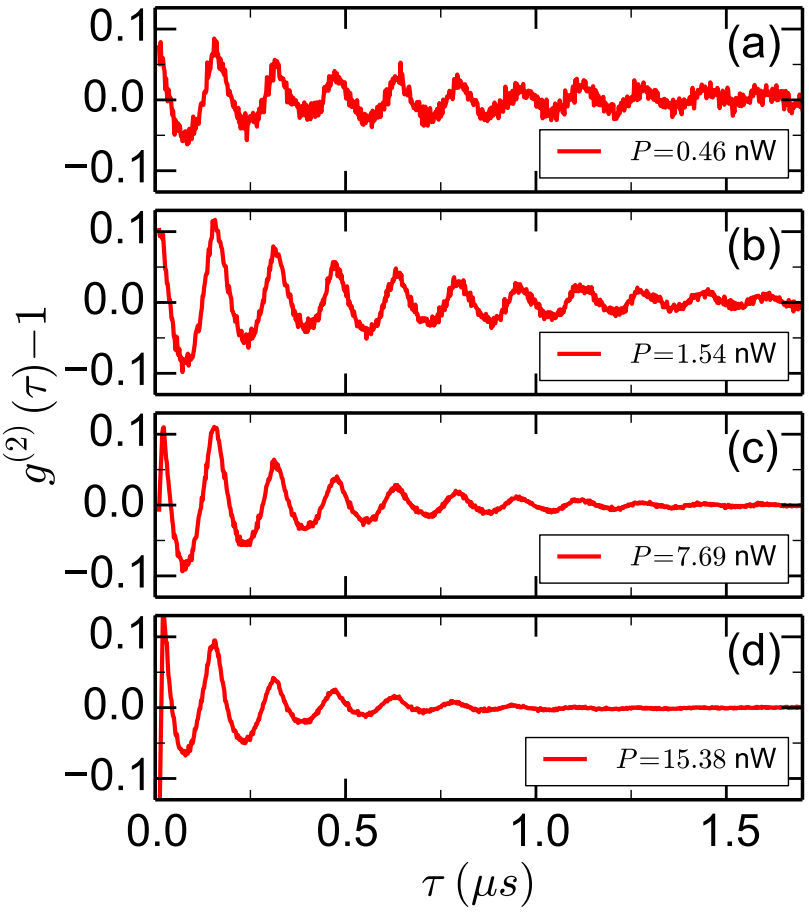

Figure 5.2: **Dependence of the image TLS decay rate Γ_i on the QD excitation power.** $g^{(2)}$ function displaying the image TLS Rabi oscillations for (a) $P = 0.46$ nW ($\Omega_{QD} = 85.85$ MHz, $\Gamma_i = 1.68(6)$ GHz) (b) $P = 1.54$ nW ($\Omega_{QD} = 157.08$ MHz, $\Gamma_i = 2.28(4)$ GHz) (c) $P = 7.69$ nW ($\Omega_{QD} = 351.01$ MHz, $\Gamma_i = 3.68(5)$ GHz) and (d) $P = 15.38$ nW ($\Omega_{QD} = 496.41$ MHz, $\Gamma_i = 4.67(7)$ GHz).

As the probability of collecting two photons with a time interval Δt between them decays exponentially (assuming a Poissonian distribution), the oscillations are expected to exponentially decay. To get rid of this undesired slope, we used an exponential function to fit the decay and the fitted function was subtracted from the data.

In summary, we have experimentally observed, through the second-order correlation function, the interaction between a QD and a metal surface separated by a distance shorter than the driving field wavelength. It was also shown that the decay rate and frequency of these oscillations depend on the excitation power, and that this dependence might be caused by alterations of the charges and currents confined on the conductor surface.

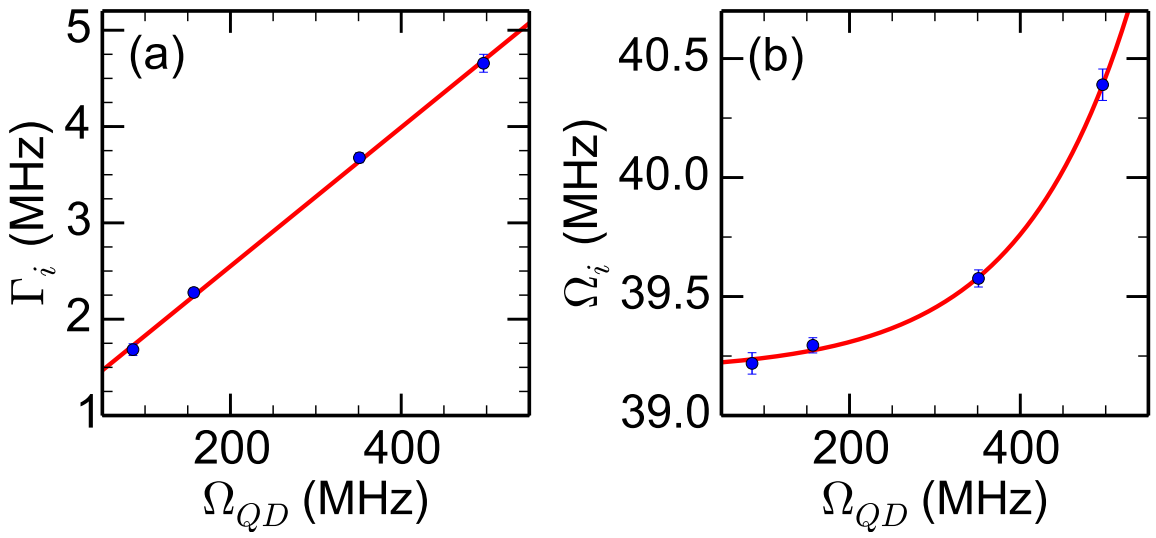

Figure 5.3: **Decay rate and frequency of the oscillations due to the presence of the metal surface as a function of the Rabi frequency.** (a) The decay rate of the oscillations depends linearly on the Rabi frequency Ω_{QD} with $\Gamma_i(\Omega_{QD}) = 0.0072(2)\ \Omega_{QD} + 1.11(5)$. (b) The frequency of the oscillations is also dependent on Ω_{QD} and its curve can be fitted using $\Omega_i(\Omega_{QD}) = 0.03(1)\exp[0.008(1)\Omega_{QD}] + 39.18(4)$.

Two QDs under the same laser spot near a metal surface

Some reports have been made about the nature of the light emitted by more than one source through correlation functions [105, 106], effective lifetime [107] and intensity [108, 109]. These results point to phenomena like superradiance and subradiance [107, 110, 111], which are the cooperative emission of photons from different single photon sources and a cooperative inhibition of this emission, respectively. A pair of two-level systems can also be very useful in the field of quantum information because they can be used to generate entangled states [110], which are key for quantum information processing. Here we report the dependence of the expected number of photons emitted by a set of two QDs under the same laser spot in the PCA device with moderate intrinsic charge noise (Sample 3), which has the Au mirror 196.6 nm away from the QD layer.

Initially, the bias voltage was tuned to a value where the X^{1-} transition is expected. Then the nano drives and the xy-scanner [Appendix A] were used to move the sample in the xy-plane while the PL signal was used to search for two QDs with transition energies close enough to be completely tuned to resonance by applying an external magnetic field smaller than 9 T, which was the maximal that the superconducting magnet installed in the cryostat could reach [Appendix A]. After two such QDs were identified, a PL map was acquired and the spectral separation can be observed in [Fig. 5.4].

The Stark coefficient for the X^{1-} transition of the QDs was measured by acquiring

detuning spectra for different wavelengths of the resonant excitation laser and recording the position of the peaks. From this measurement it was concluded that the Stark coefficient for $QD_{1(2)}$ is $1.641(1.735)$ μeV/mV and the wavelength chosen for the simultaneous excitation of the QDs was 960.595 nm, where the spectral separation is ~ 51 μeV [Fig. 5.5 (a)].

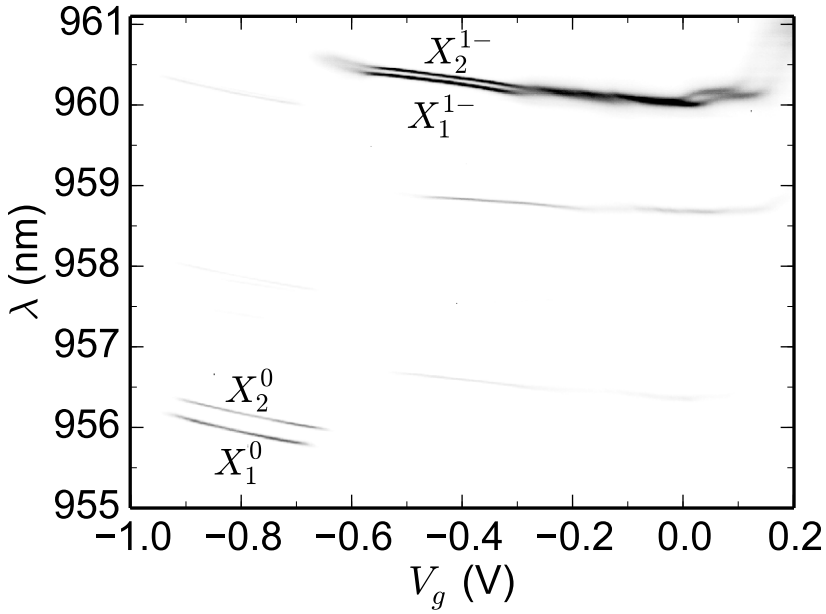

Figure 5.4: **PL map acquired to localise two spectrally close QDs.** PL map acquired from the excitation of QDs with a non-resonant driving field (830 nm) and analysing the signal using a spectrometer at 1800 g/mm.

A power dependence of the expected number of photons was also measured for simultaneous excitation of the transitions, from where the saturation powers $P_1^{sat} = 60.0$ nW and $P_2^{sat} = 39.1$ nW were extracted through the fit of a TLS model [Eq. 3.14], as presented in [Fig. 5.5 (b)].

The spatial separation between the two QDs also needs to be investigated because it is crucial for the estimation of the energy exchange between the QDs through dipole-dipole interaction [112] or even through an electronic coupling [113, 114].

The distance between the QDs was measured using by monitoring the RF signal of a single QD with a SPAD while moving the position of the sample relative to the laser spot using a xy-scanner [Appendix A]. The position map for QD_1 and QD_2 can be observed in [Fig. 5.6 (a) and (c)], respectively. The cross section of both maps (dashed lines) presents a Gaussian profile in both directions, as presented in [Fig. 5.6 (b) and (d)], in good agreement with the theory presented in [115].

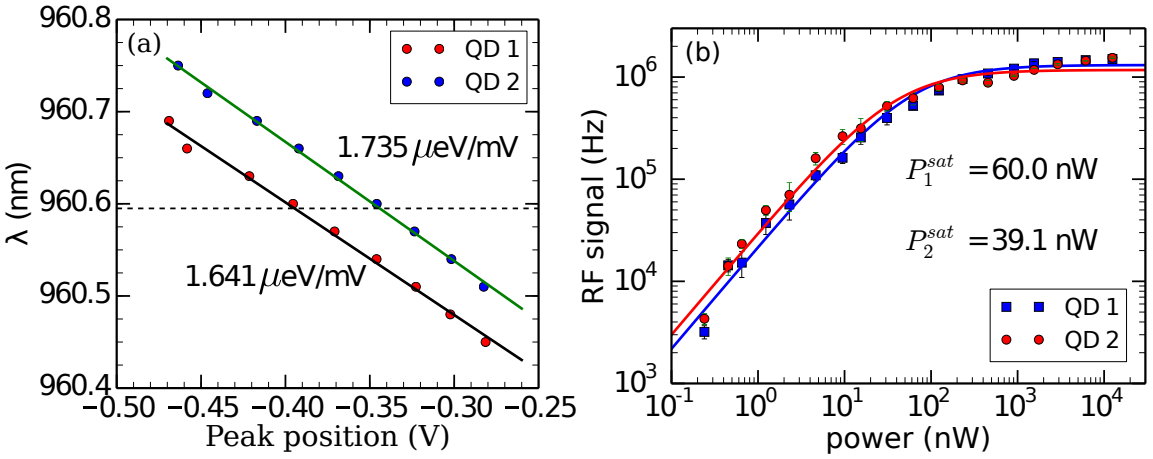

Figure 5.5: **Stark shift and saturation curve for two QDs under the same laser spot.** (a) Stark coefficient measured by recording the detuning spectrum position as a function of the wavelength of the excitation laser. The dashed horizontal line at 960.595 nm represents the wavelength chosen for the simultaneous excitation of the QDs, where the spectral separation is ~ 51 μeV. (b) Saturation curve of the two QDs for $\lambda = 960.595$ nm and their respective TLS fits [Eq. 3.14], from which the saturation powers $P_1^{sat} = 60.0$ nW and $P_2^{sat} = 39.1$ nW were extracted.

With the identification of the position of each QD in the xy-plane from the Gaussian curves it was possible to conclude that the spatial separation between the QDs is $\sim 158(4)$ nm, so with wavenumber $k \approx 0.0065$ nm^{-1} we have $kr \approx 1.03(3)$.

The application of an external magnetic field is needed to tune the transitions of the two QDs into resonance, as explained in [Fig. 5.14], and a few steps of this process can be observed in [Fig. 5.7 (a)], where the detuning spectra of both QDs are presented for an external magnetic field equal to 0.1 T, 0.4 T and 0.72 T. The excitation power used was about 1 nW in order to minimise the influence of the charge noise in the measurements, as presented in [Fig. 3.23]. The energy of the transitions as a function of B_{ext} was traced using the detuning spectrum [Fig. 5.7 (b)]. In the absence of a magnetic field, the difference between the transition energies is ~ 86 μeV. As the magnetic field is increased, the energy of the σ^+ transition of QD_1 (QD_2) increases with rate equal to $62(3)$ μeV/T ($51(4)$ μeV/T) while the σ^- transition energy decreases with rate equal to $69(4)$ μeV/T ($62(2)$ μeV/T), consequently the σ^+ transition of QD_1 and the σ^- of QD_2 are tuned into resonance at $0.70(2)$ T. With this information it is possible to calculate the combined Zeeman splitting (ZS) of the electron and HH as a function of B_{ext} for each QD, which is $131(2)$ μeV/T for QD_1 and $113(3)$ μeV/T for QD_2 [Fig. 5.7 (c)].

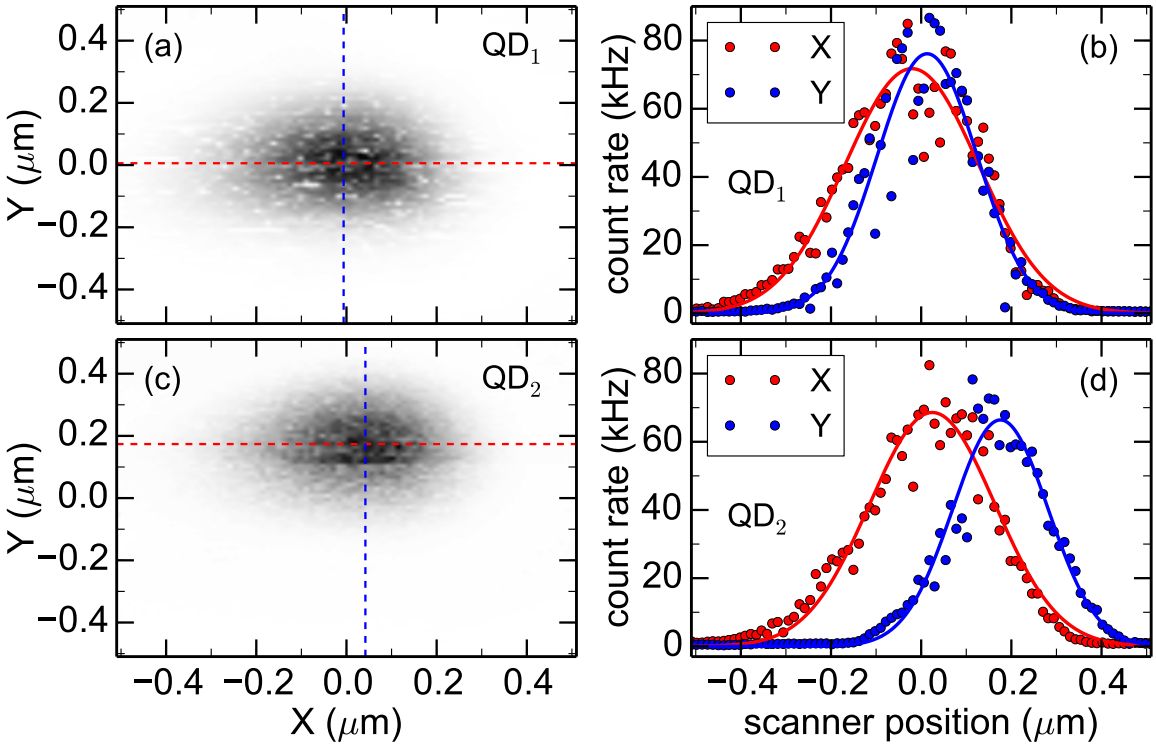

Figure 5.6: **Investigating the spatial separation between the two QDs.** (a) and (c) RF signal as a function of xy-scanner position for QD_1 and QD_2, respectively, with the dashed lines indicating the position where the cross sections in (b) and (d) were considered. (b) and (d) Cross sections of the RF signal as a function of xy-scanner position, as indicated by the dashed lines in the maps, fitted with a Gaussian curve. The width of the curve for QD_1 (QD_2) in the x-direction is $0.052(2)$ μm ($0.045(2)$ μm) and in the y-direction it is $0.03(1)$ μm ($0.026(2)$ μm), and the distance between the QDs is $158(4)$ nm.

To investigate the oscillations due to the interaction with the gold surface, the arrival time of emitted photons was recorded using the PicoHarp in time tagging mode after passing through the HBT interferometer. From this, it was possible to rebuild the coincidence histogram with a minimal time bin T_{bin} equal to 4 ps. Since the timescale of interest is in the microseconds range, no delay was utilised to shift the $\tau = 0$ point and the time bin T_{bin} was made equal to 50 ns.

To demonstrate that photons from both QDs are collected, the second-order correlation function was measured for the two bias voltages (-0.424 V and -0.322 V) where photons from only one of the QDs are expected [Fig. 5.8 (a-b)]] and for the bias voltage where photons are expected from both QDs (-0.367 V). The second-order correlation function of the tuned transitions has $g^{(2)}(0) = 0.6$, which is close to the value expected for two identical and uncorrelated emitters ($g^{(2)}(0) = 0.5$) [Fig. 5.8 (c)].

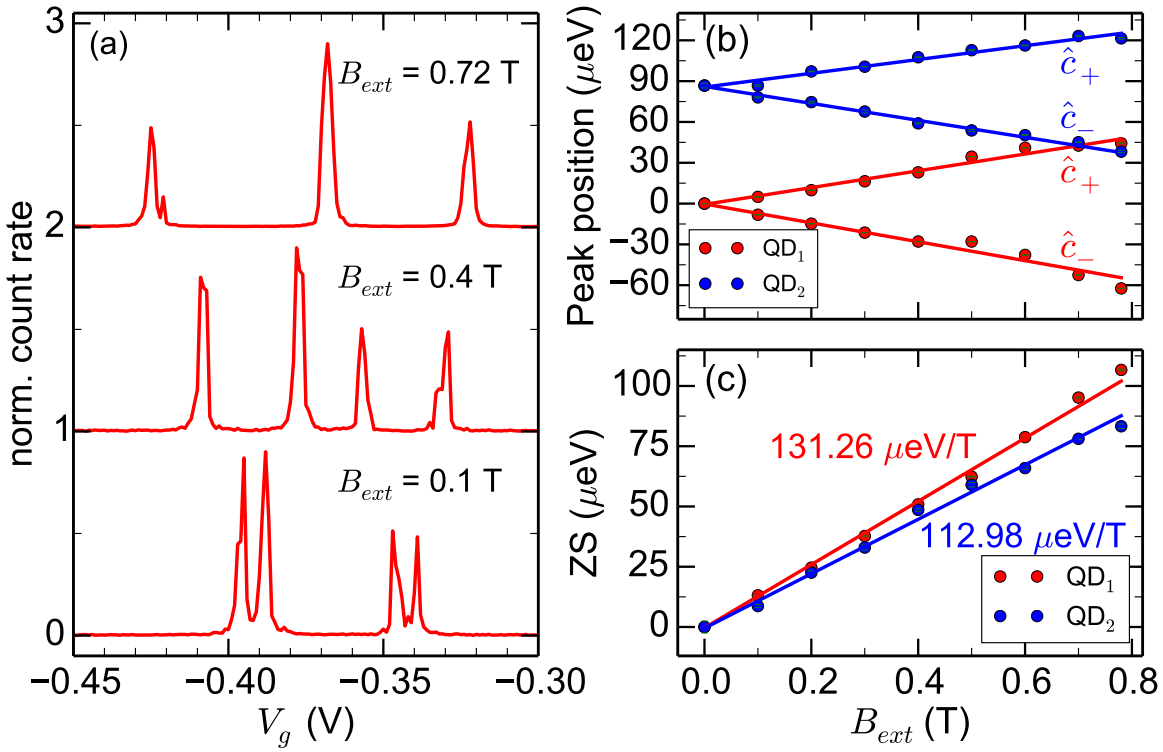

Figure 5.7: **Tuning QDs transitions using an external magnetic field in the Faraday geometry.** (a) Detuning spectra of two QDs under the same laser spot with $P \approx 1$ nW for $B_{ext} = 0.1$ T, 0.4 T and 0.72 T. (b) In the absence of a magnetic field, the difference between the transition energies is $\sim$ 86 μeV. As the magnetic field is increased, the σ^+ transition energy of QD$_1$ (QD$_2$) increases with rate equal to $62(3)$ μeV/T ($51(4)$ μeV/T) while the σ^- transition energy decreases with rate equal to $69(4)$ μeV/T ($62(2)$ μeV/T), consequently the σ^+ transition of QD$_1$ and the σ^- transition of QD$_2$ are tuned into resonance at $0.70(2)$ T. (c) The combined Zeeman splitting (ZS) of the electron and HH is $131(2)$ μeV/T for QD$_1$ and $113(3)$ μeV/T for QD$_2$.

With the two transitions of the QDs tuned into resonance using the external magnetic field, excitation power $P = 0.3$ nW and the laser wavelength set to be in the middle of the plateaus of both QDs, the second-order correlation function for a single emitter was acquired by tuning the $\hat{c}_-$ transition of QD$_1$ into resonance with the laser, and, as it was discussed in [Sec. 5.1], it was possible to observe the coherent oscillations at $\tau \gg 1/\Gamma$ for a single QD with frequency $\Omega_1 \approx 0.545$ MHz [Fig. 5.9 (a)]. Then the bias voltage was changed to bring the two tuned QD transitions into resonance with the laser and the second measurement was performed [Fig. 5.9 (b)]. In this case, it was observed that the oscillations are very similar to those obtained for a single QD [Fig. 5.9 (e)], confirming the resonance between the transitions of the two QDs.

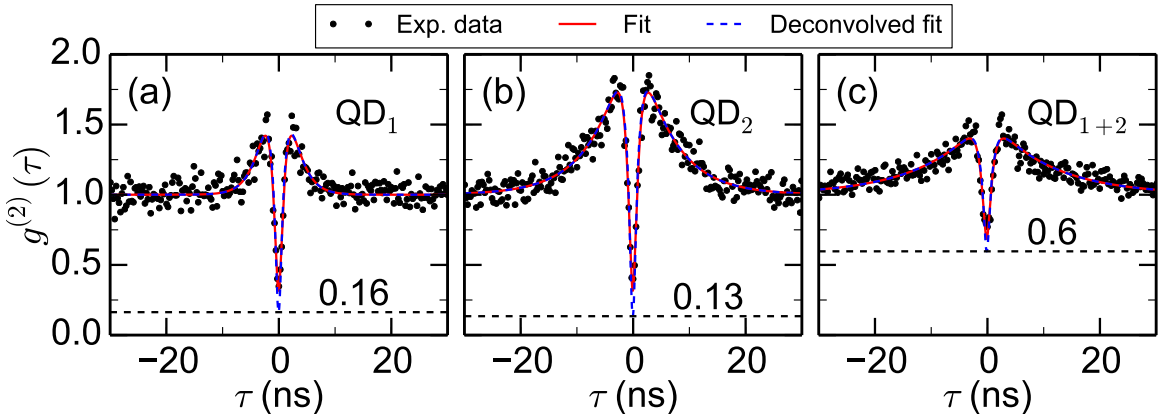

Figure 5.8: $\mathbf{g^{(2)}(\tau)}$ **function demonstrating the photon emission from two single photon sources.** The $g^{(2)}(\tau)$ function was acquired at $P = 0.77$ nW and for the deconvolved fit we have (a) $g^{(2)}(0) = 0.16$, (b) $g^{(2)}(0) = 0.13$, and (c) $g^{(2)}(0) = 0.6$, demonstrating the tuning between the two QDs.

A change in the frequencies composing the coherent oscillations was achieved by detuning the two QDs using the external magnetic field. With QD_1 detuned by -254 MHz and QD_2 detuned by 219 MHz, the two measured frequencies were separated by 0.071 MHz and a beating can be observed in [Fig. 5.9 (c)].

The symmetry of the oscillations around the detuning was also probed, by detuning QD_1 by 190 MHz and QD_2 by -164 MHz and comparing with the previous measurement [Fig. 5.9 (d)]. The confirmation of this symmetry can be observed in [Fig. 5.9 (f)], where the frequency of the oscillations matches surprisingly well in spite of a considerable discrepancy among the detuning values.

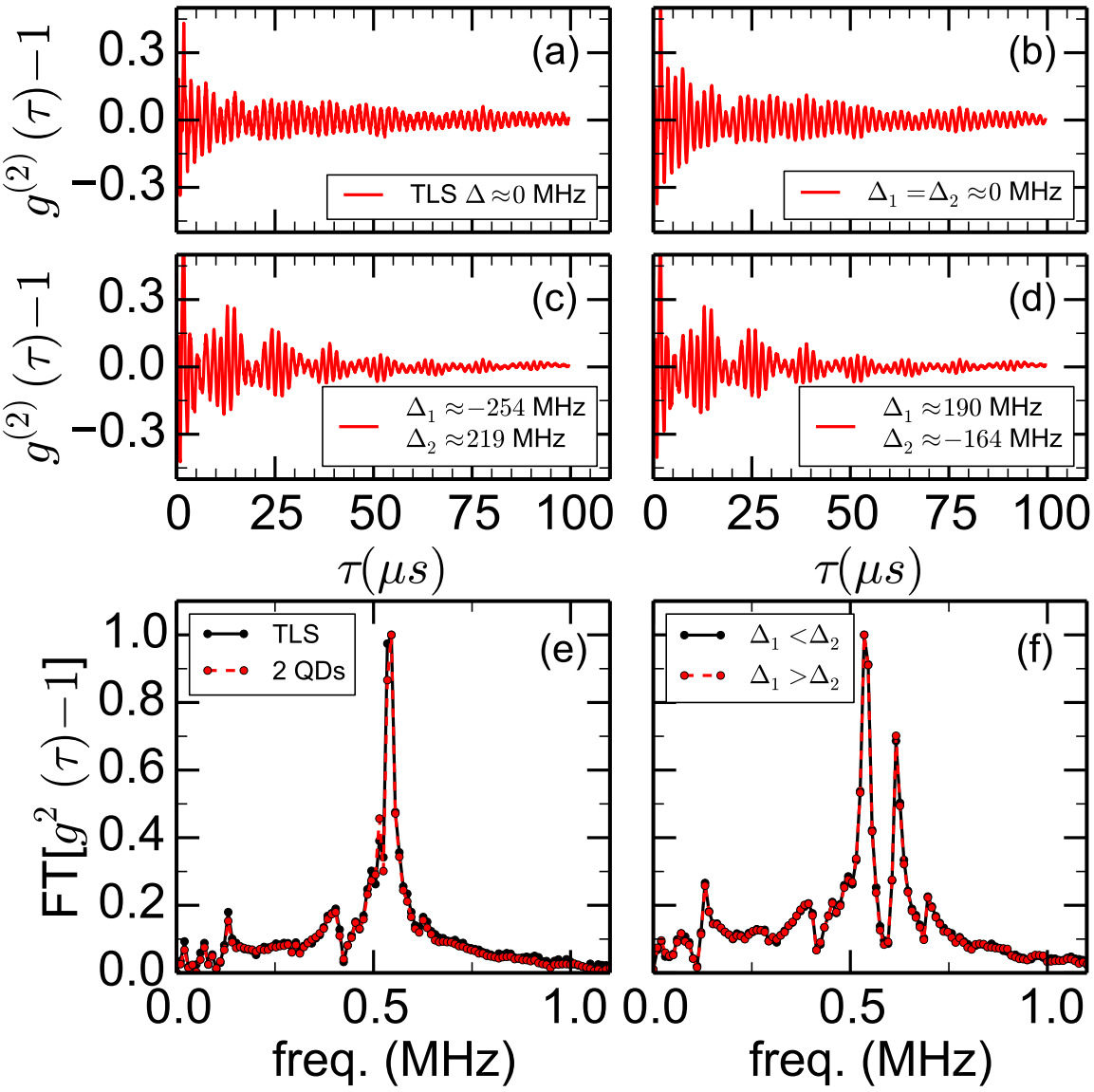

Figure 5.9: $g^{(2)}(\tau)$ **function of two QDs near a metal surface.** Oscillations measured with excitation power $P = 0.3$ nW for (a) a single emitter (QD_1) (b) two emitters with zero detuning (c) two emitters with $|\Delta_1|-|\Delta_2| = 35$ MHz (d) two emitters with $|\Delta_1|-|\Delta_2| = 26$ MHz. (e) Coherent oscillations in the frequency domain for (a) and (b). (f) Coherent oscillations in the frequency domain for (c) and (d).

A two-level system near a conducting surface

In this section, two possible approaches in the interaction between the TLS and a metal surface are discussed. In the first approach, the conducting surface is treated as a simple reflecting surface with reflectivity equal to 1 [116, 117, 118, 119]. In the second approach, the charges and currents induced in the metal surface by the electric field radiated from the QD [120] are considered as a second TLS with decay rate Γ_i and Rabi frequency Ω_i [121, 122, 123, 124, 125].

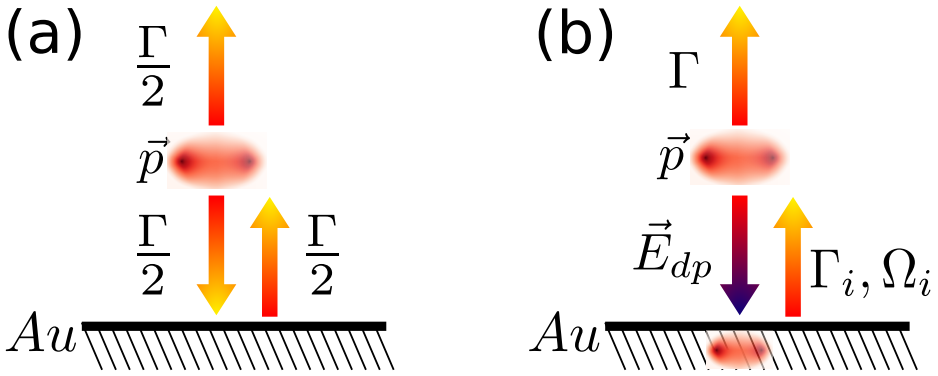

Figure 5.10: **Two possible approaches for the TLS-metal interaction.** (a) The QD with dipole moment $\vec{p}$ emits half of its radiation towards the detector and the other half towards the perfect mirror, which reflects towards the detector. The undetectable solid-angles are not considered. (b) The electric field radiated by the QD (dipole-approximation) confines oscillating charges and currents in the metal surface which then emit photons towards the detector.

Metal as a reflecting surface

To discuss the case depicted in [Fig. 5.10 (a)], any dynamics in the metal surface due to the original QD is neglected and the mirror is introduced in the TLS through the σ_- operator, which is given by

$$\sigma_- = \sqrt{\frac{\Gamma}{2}}\left(1 + e^{-i\omega_l \delta t}\right)|g\rangle\langle e| \ , \tag{5.2}$$

where ω_l is the laser frequency and δt is the travel time of the photon from the QD to the mirror and back to the QD layer [119].

Since the whole system still behaves like a single TLS with an effective decay rate $\Gamma_{eff}(\omega_l \delta t)$ with incorporated mirror effect, in this model, the photon statistics and correlation functions [Chapter 3] are also expected to have strong dependence on $\omega_l \delta t$. For example, from [Eq. 5.2], the expected number of photons collected in a hypothetical case of perfect collection efficiency is

$$\langle n \rangle = \Gamma[1 + \cos(\omega_l \delta t)]\rho_{ee}(\infty) \ , \tag{5.3}$$

with the periodic function accounting for the interference of the light emitted from the QD and reflected by the metal surface. Still on the steady state solution side of the analysis, alterations in the detuning spectrum, saturation curve, and width of the inelastic peaks are also expected, since it is expected that the decay rate changes by varying $\omega_l \delta t$ [Fig. 5.11]. The second-order correlation function has a slope ($\tau < 1/\Gamma$) [Fig. 5.11 (c)] and the damping of the Rabi oscillations dependent on the decay rate, so it would also suffer alterations with $\omega_l \delta t$.

In the present experimental situation, τ is a constant defined by FDTD simulations taking into account a more realistic picture of the gold layer, which is not a perfect conductor. In all PCA devices analysed here (Sample 2 and Sample 3), the photoluminescence map showed QDs in a wavelength range going from $\sim$ 930 nm to $\sim$ 980 nm and ω_l is determined by QD selection. In RF, ω_l is constant so the term $\cos(\omega_l \delta t)$ should be very small according to the simulated results, which could be confirmed by comparing the decay rate of these samples to other samples without the Au mirror, but with similar structure, like the bulk sample (Sample 1).

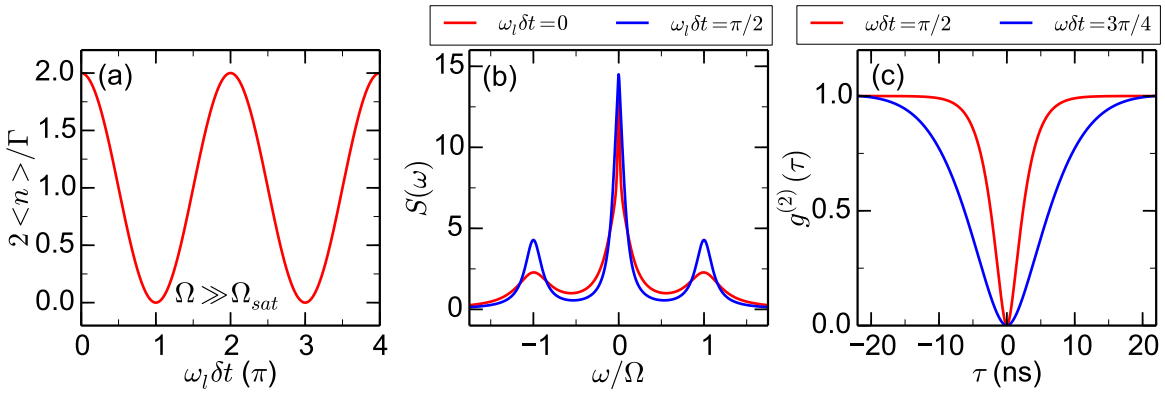

Figure 5.11: **Effects of $\omega_l\delta t$ on the photon statistics.** (a) Expected number of counts scattered from the system as a function of $\omega_l\delta t$ for $\Omega \gg \Omega_{sat}$. (b) The width of the inelastic peaks are defined by the decay rate of the TLS, so, they are strongly dependent on $\omega_l\delta t$. (c) At low Rabi frequency ($\Omega = 0.1\Omega_{sat}$), the slope at $\tau < 1/\Gamma$ is also sensitive to $\omega_l\delta t$.

QD and image dipole approach

A different approach, depicted by [Fig. 5.10 (b)], considers the oscillating charges and currents in the metal surface induced by the electric dipole field $\vec{E}_{dp}$ radiated by the QD [120] as a second TLS, with corresponding Rabi frequency Ω_i and decay rate Γ_i. In this model, the electric field of the dipole $\vec{E}_{dp}$ is considered constant, since the driving field is continuous and the collapse of the wavefunction due to the photon count is assumed to be faster than any other dynamic phenomenon in both TLSs. The optical transition of the original TLS is circularly polarised (X^{1-}) and photons coming from the image TLS are expected to have a π shift, having orthogonal polarisation relative to the photon emitted by original TLS. For simplicity, we neglect any possible dipole-dipole interaction between the QD and its image.

Under these assumptions, the Hamiltonian of the system can be written as

$$H = H_{QD} \otimes H_i \,, \tag{5.4}$$

which for $\Delta_{QD,i} = 0$ is

$$H = \frac{\Omega_{QD}}{2}\left(|0\rangle\langle 2| + |1\rangle\langle 3| + h.c.\right) + \frac{\Omega_i}{2}\left(|0\rangle\langle 1| + |2\rangle\langle 3| + h.c.\right) \ , \tag{5.5}$$

where the states were mapped as

$$|0\rangle = |g-\rangle \tag{5.6}$$

$$|1\rangle = |g+\rangle \tag{5.7}$$

$$|2\rangle = |e-\rangle \tag{5.8}$$

$$|3\rangle = |e+\rangle \ , \tag{5.9}$$

where $|-\rangle$ ($|+\rangle$) is the ground (excited) state of the image TLS [Fig. 5.12].

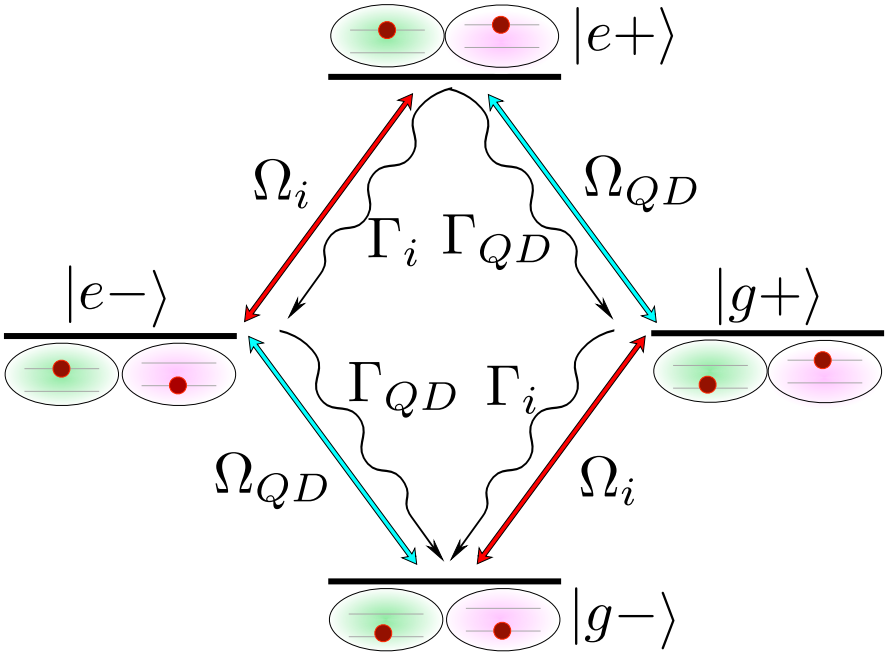

Figure 5.12: **Energy diagram of the system composed of two image quantum dots.** The ground state is composed of both QD and image TLS in the ground state, the second (third) level has the QD in the ground (excited) state while the image TLS is in the excited (ground) state, and the fourth level has the QD and the image TLS in the excited state.

Because the transitions are orthogonal, the Lindblad operators can be calculated separately as

$$L(\sigma_-)\rho = L\left(\sigma_-^{QD}\right)\rho + L\left(\sigma_-^{i}\right)\rho \ , \tag{5.10}$$

with

$$L(o)\rho = o\rho o^\dagger - \frac{o^\dagger o\rho}{2} - \frac{\rho o^\dagger o}{2} \ , \tag{5.11}$$

and the density matrix is calculated numerically using the master equation

$$\frac{d\rho}{dt} = -i[H,\rho] + L\left(\sigma_-^{QD}\right)\rho + L\left(\sigma_-^{i}\right)\rho \ . \tag{5.12}$$

The number of emitted photons is

$$\langle n \rangle = \langle n_{QD} \rangle + \langle n_i \rangle \tag{5.13}$$

and no interference term is expected, since the transitions are orthogonal [Fig. 5.13 (a)]. The first-order correlation functions can also be calculated separately due to the polarisation, but in the second-order correlation function, some expressions involving both TLSs are expected.

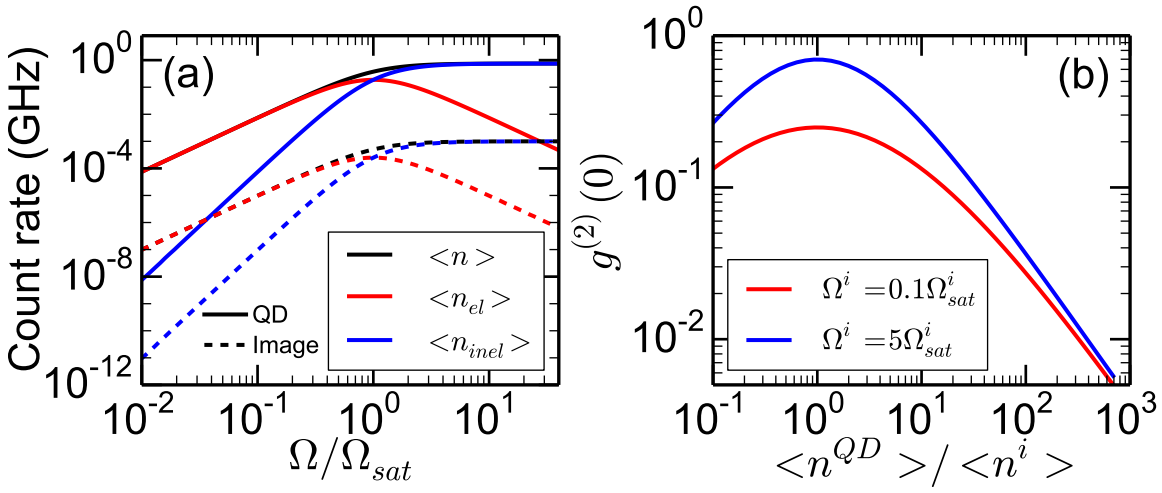

Figure 5.13: **Photon counting rate and expected degree of antibunching of a QD-image system.** For $\Gamma_{QD} = 1.5$ GHz and $\Gamma_i = 2$ MHz, (a) the expected number of photons (total, elastic and inelastic), assuming perfect collection and detection, was calculated as a function of the Rabi frequency for the TLS (solid lines) and its image (dashed lines) (b) the intensity correlation at $\tau = 0$ was calculated in terms of the ratio between the expected number of photons for the TLS and its image by keeping the Rabi frequency of the image TLS constant at $0.1\Omega^i_{sat}$ for the red curve and $5\Omega^i_{sat}$ for the blue curve, and varying the Rabi frequency of the original TLS.

Writing the annihilation operators as

$$\sigma_-^{QD} = \sqrt{\Gamma}\hat{c}_\pm \left(|0\rangle\langle 2| + |1\rangle\langle 3|\right) \tag{5.14}$$

$$\sigma_-^{i} = \sqrt{\Gamma_i}\hat{c}_\mp \left(|0\rangle\langle 1| + |2\rangle\langle 3|\right) \ , \tag{5.15}$$

where $\hat{c}_\pm$ refers to the circular polarisation of the transition, the system annihilation operator is

$$\sigma_- = \sigma_-^{QD} + \sigma_-^{i} \tag{5.16}$$

and the second-order correlation function can be calculated as

$$g^{(2)}(\tau) = \langle \sigma_+(t)\sigma_+(t+\tau)\sigma_-(t+\tau)\sigma_-(t)\rangle \tag{5.17}$$

$$g^{(2)}(\tau) = \mathrm{Tr}\left[U^-(\tau)\sigma_-\rho\sigma_+U(\tau)\sigma_+\sigma_-\right] \tag{5.18}$$

$$g^{(2)}(\tau) = g^{(2)}_{QD}(\tau) + g^{(2)}_{i}(\tau) + \mathrm{Tr}\left[U^{-}(\tau)\sigma^{QD}_{-}\rho(t)\sigma^{QD}_{+}U(\tau)\sigma^{i}_{+}\sigma^{i}_{-}\right] + \mathrm{Tr}\left[U^{-}(\tau)\sigma^{i}_{-}\rho(t)\sigma^{i}_{+}U(\tau)\sigma^{QD}_{+}\sigma^{QD}_{-}\right], \quad (5.19)$$

where U is the propagator. The last two terms in [Eq. 5.29] are responsible for the dependence of $g^{(2)}(0)$ on the properties of the TLS and its image [Fig. 5.13 (b)].

This model predicts a non-zero $g^{(2)}(0)$ and two different dynamics in the second-order correlation function, supporting the experimental result presented in [Fig. 5.1]. Explanations of the relatively small decay rate and coupling energy are still missing.

Two two-level systems near a metal surface

In this section, I will discuss the results of an experiment where two distinct QDs near a metal surface interact with the same linearly polarised driving field. We start from a simple model to explain the results. Two QDs, initially with different transition energies, have their transitions tuned on resonance through the application of an external magnetic field in the Faraday geometry [Fig. 5.14]. Then, using linearly polarised radiation, both transitions can be driven simultaneously and, for a particular magnetic field the energy diagram can be reduced to [Fig. 5.12] because of the large detuning between the on-resonance transitions and the two outer transitions.

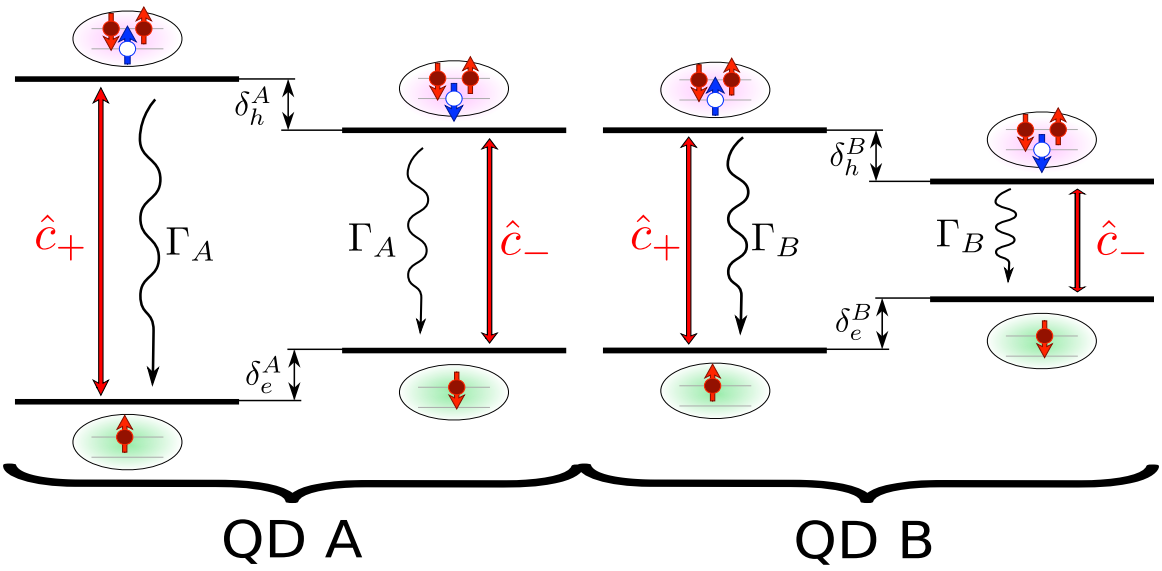

Figure 5.14: **Tuning two QDs transitions using an external magnetic field.** Although a difference in selection rules exists for the degenerate transitions, the degenerate transitions can be excited simultaneously using a linearly polarised light.

We are interested in studying the dynamics imposed by the metal surface, which was already demonstrated to have a timescale in the microsecond range [Sec. 5.1]. Here we

do not consider the original QDs' dynamics, which occur on the nanoseconds timescale. Because of the orthogonal polarisations of the two tuned transitions, the image transitions are also expected to be orthogonal to each other; consequently, their evolution is completely independent. Under these assumptions, we have a ground state composed of two image dipoles in the ground state, and the second and the third levels are composed of one of the image dipoles in the excited state and the other image dipole in the ground state. These states can be tuned on or off resonance with each other by tuning their energies with the applied magnetic field. The fourth level is composed of both image dipoles in the excited state [Fig. 5.12]. The Rabi frequencies and the decay rates of the image dipoles may not be equal, as they depend on the original QDs. For this reason, they are going to be labelled as A and B.

For convenience, the states can be written as

$$|gg\rangle = |0\rangle \tag{5.20}$$

$$|ge\rangle = |1\rangle \tag{5.21}$$

$$|eg\rangle = |2\rangle \tag{5.22}$$

$$|ee\rangle = |3\rangle \ . \tag{5.23}$$

It was assumed that the distance between the two image dipoles is large enough to neglect coupling between them. Therefore, the Hamiltonian of the system is

$$\begin{aligned} H &= -\frac{(\Delta_A+\Delta_B)}{2}|0\rangle\langle 0| - \frac{(\Delta_A-\Delta_B)}{2}|1\rangle\langle 1| + \frac{\Delta_A-\Delta_B}{2}|2\rangle\langle 2| + \frac{\Delta_A+\Delta_B}{2}|3\rangle\langle 3| \\ &+ \frac{\Omega_A}{2}(|0\rangle\langle 2| + |1\rangle\langle 3| + h.c.) + \frac{\Omega_B}{2}(|0\rangle\langle 1| + |2\rangle\langle 3| + h.c.) + \frac{\Omega_A\Omega_B}{4}(|0\rangle\langle 3| + h.c.) \ . \end{aligned} \tag{5.24}$$

The annihilation operators are

$$\sigma_-^A = \sqrt{\Gamma_A}\hat{c}_-(|0\rangle\langle 2| + |1\rangle\langle 3|) \tag{5.25}$$

$$\sigma_-^B = \sqrt{\Gamma_B}\hat{c}_+(|0\rangle\langle 1| + |2\rangle\langle 3|) \ , \tag{5.26}$$

where the unit vectors $\hat{c}_\pm$ represent the circular polarisation of the transition. Their radiative decay are described by the Lindblad operator

$$L(o)\rho = o\rho o^\dagger - \frac{o^\dagger o\rho}{2} - \frac{\rho o^\dagger o}{2} \ , \tag{5.27}$$

and the master equation

$$\frac{d\rho}{dt} = -\frac{i}{\hbar}[H,\rho] + L(\sigma_-^A)\rho + L(\sigma_-^B)\rho \tag{5.28}$$

was solved numerically in order to obtain the temporal evolution of the density matrix.

Second-order correlation function

The second-order correlation function $g^{(2)}(\tau)$ is calculated by taking into account the fact that the image dipoles are independent of each other, so it is similar to [Eq. 5.29], but with the original QD operators replaced by the operators corresponding to the second image dipole:

$$\begin{aligned} g^{(2)}(\tau) &= g_A^{(2)}(\tau) + g_B^{(2)}(\tau) + \mathrm{Tr}\left[U^-(\tau)\sigma_-^A\rho(t)\sigma_+^A U(\tau)\sigma_+^B\sigma_-^B\right] \\ &+ \mathrm{Tr}\left[U^-(\tau)\sigma_-^B\rho(t)\sigma_+^B U(\tau)\sigma_+^A\sigma_-^A\right] . \end{aligned} \tag{5.29}$$

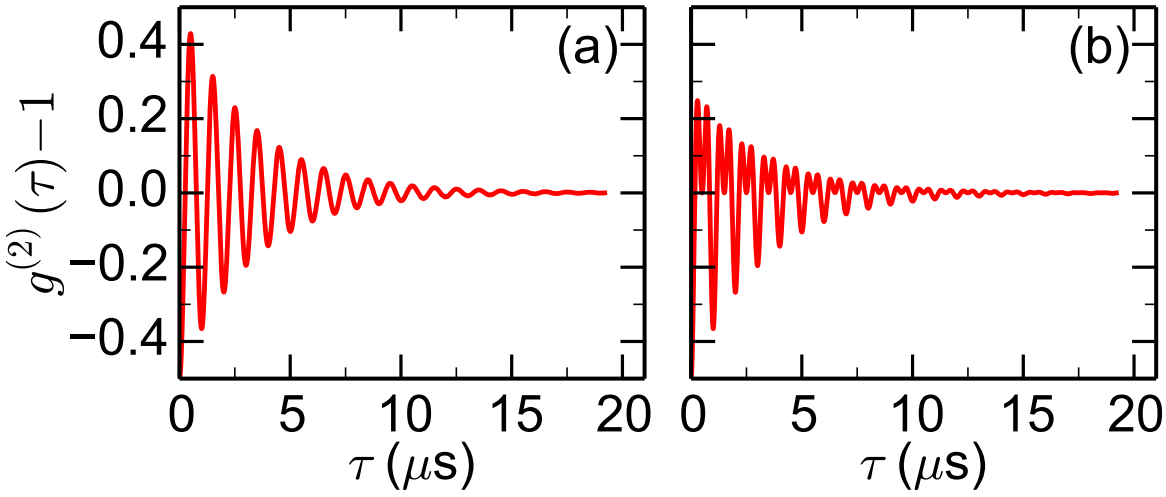

Figure 5.15: **Effect of the Rabi frequency mismatch between the two image dipoles in the $g^{(2)}(\tau)$ function.** Superposition of the Rabi oscillations of two image dipoles for $\Gamma = 0.5$ MHz, $\Delta = 0$ MHz and (a) $\Omega_{A,B} = 1$ MHz, (b) $\Omega_A = 1$ MHz and $\Omega_B = 2$ MHz.

If the image dipoles are identical, except for the polarisation, the $g^{(2)}(\tau)$ function will be similar to the one presented for a single image [Fig. 5.15 (a)], but if there is a mismatch between their Rabi frequencies, it is expected that the $g^{(2)}(\tau)$ function will be affected by the superposition of two distinct Rabi oscillations [Fig. 5.15 (b)].

For a single ideal TLS, the detuning between the driving field and the transition energy increases the frequency of the damped oscillations presented in the $g^{(2)}(\tau)$ function with $\sqrt{\Omega^2 + \Delta^2}$. The same is true of two independent TLSs. If the absolute values of Δ_A and Δ_B are equal, then only one frequency should be present in the oscillation (assuming same Rabi frequency for both image dipoles) [Fig. 5.16 (a) and (c)]. If $\Omega_A = \Omega_B$ and $|\Delta_A| \neq |\Delta_B|$, there will be two different frequencies superimposed in the Rabi oscillations [Fig. 5.16 (b) and (d)].

In this section, the second-order correlation function of a pair of QD-image dipole was discussed taking into account the different timescales expected for their dynamics. Due to the selection rules of the original QDs transitions tuned into resonance using an external magnetic field in the Faraday geometry, the analysis could be simplified to the case where the temporal evolution of the pairs are completely independent. Under these circumstances, the model supports the experimental data presented in [Fig. 5.9], but it cannot explain the timescale of the oscillations.

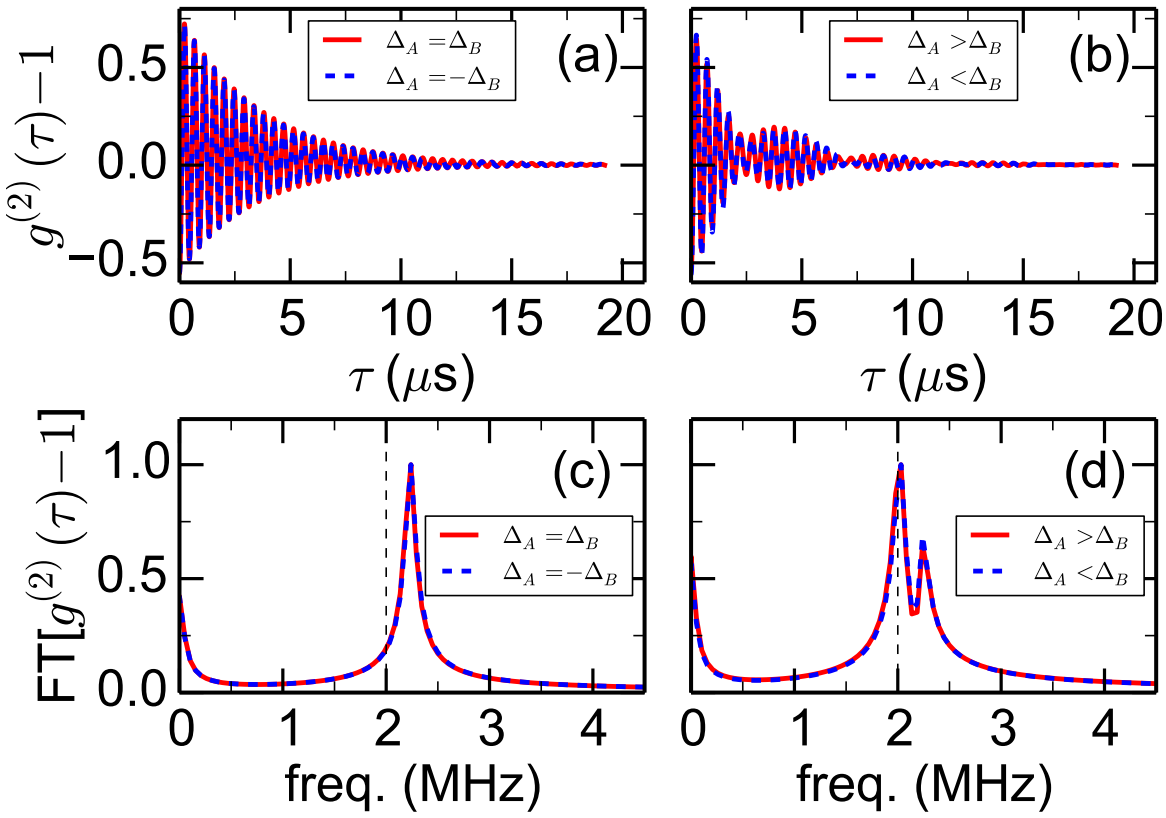

Figure 5.16: **Effect of the detuning mismatch between the two image dipoles on the $g^{(2)}(\tau)$ function.** Superposition of the Rabi oscillations of two image dipoles for $\Gamma_{A,B} = 0.5$ MHz, $\Omega_{A,B} = 2$ MHz and (a) $|\Delta_{A,B}| = 1$ MHz (b) $\Delta_A = 1$ MHz and $\Delta_B = -0.3$ MHz (red solid line) or $\Delta_A = -1$ MHz and $\Delta_B = 0.3$ MHz (blue dashed line). (c) and (d) are the normalised Fourier transform of (a) and (b), respectively, with the dashed black line corresponding to the Rabi frequency used.

Summary

In this chapter, experimental observation of the interaction between QDs and a metal surface was presented along with a simplified model which agrees qualitatively with the experimental data. Here, it is suggested that a fraction of the photons detected are from an image dipole based on the following characteristics: different coherence time of the image dipole while the emission rate of the original QD is conserved, the dependence of the image

dipole properties (Γ_i, Ω_i) on the Rabi frequency of the QD and the sensitivity of the these photons to the detuning between the driving field and the original transition.

Chapter 6

Conclusion

An experimental setup was constructed to perform resonance fluorescence experiments on devices containing a single QD layer in the Laboratory of Quantum Photonics at Heriot-Watt University. The confocal dark-field microscope built was able to suppress the light reflected by the sample surface by $> 10^7$ using two linear polarisers in orthogonal positions and exploiting the difference between the polarisation of the photons reflected and the photons emitted by the QD.

Using this experimental setup, the properties of the X^{1-} transition of single QDs were investigated using the resonance fluorescence technique and one of the characteristics of the photon emission by the QDs for all the samples analysed was the fluctuation of the RF signal due to a dynamic density of charges in the QD environment and Overhauser field. For one of the PCA devices (Samples 2) it was demonstrated that the timescale of the spectral fluctuations happens mainly is in the milliseconds range, evidencing the domination of the charge noise over the nuclear field, while for the bulk sample (Sample 1), the experimental RF power spectrum demonstrated that the Overhauser field was dominant. The spectral fluctuations affect the photon counting statistics, the RF power spectrum and the second-order correlation function of the QD emission. In the photon counting statistics the spectral fluctuations affect the saturation curve at low excitation powers and the elastic to inelastic ratio, which are useful to extract information about the QD as lifetime and dephasing rate. The charge noise affects the Mollow triplet by increasing the width of both central peak and side peaks, decreasing the height of the side peaks relative to the central peak and shifts the side peaks to higher frequencies. Nevertheless, it was also demonstrated that it is possible to achieve a good degree of indistinguishability between two photons emitted from the same QD if the spectral fluctuations timescale is much longer than the life time of the emitter.

The RF technique is also used to measure extraction efficiency of planar cavity antenna

devices. The bulk samples with a SIL on its top have an estimated extraction efficiency of $\sim 2\%$, while the PCA device reaches $\sim 10\%$, leading to cw count rates at saturation of $0.38(1)$ MHz and $3.0(1)$ MHz, respectively.

In this work, analytical results about the effects of the Overhauser field on the power spectrum and second-order correlation of the QD emission was also presented. The Overhauser field splits the electron spin states through the Zeeman effect, which can be neglected for the heavy hole because of its weak interaction with the nuclear spin, and then Raman scattering happens, generating photons detuned by the Zeeman splitting for the ground states which give rise to two symmetric side bands ~ 200 MHz away from the central peak and with width of about ~ 200 MHz as a consequence of the Overhauser field dynamics. It affects the second-order correlation function through the detuning imposed by the Zeeman splitting.

Finally, experimental observations of the interaction between QDs and a gold mirror was presented. A simple model based on the presence of an image dipole was used to analyse the results, but the coherence time of the oscillations is still not understood.

Bibliography

[1] P. W. Shor, SIAM J. Sci. Statist. Comput. **26**, 1484 (1997), quant-ph/9508027.

[2] L. K. Grover, A fast quantum mechanical algorithm for database search, in *Proceedings of the Twenty-eighth Annual ACM Symposium on Theory of Computing*, STOC '96, pp. 212–219, New York, NY, USA, 1996, ACM.

[3] D. Loss and D. DiVincenzo, Phys. Rev. A **57**, 120 (1998).

[4] M. Bayer, O. Stern, P. Hawrylak, S. Fafard, and A. Forchel, Nature **405**, 923 (2000).

[5] P. M. Petroff, A. Lorke, and A. Imamoglu, Physics Today **54**, 46 (2001).

[6] A. N. Vamivakas, Y. Zha, C.-Y. Lu, and M. Atatüre, Nat. Phys. **5**, 198 (2009).

[7] D. Brunner, *Laser spectroscopy of coherent quantum states in single quantum dots*, PhD thesis, School of Engineering and Physical Sciences - Heriot-Watt University, 2010.

[8] A. Y. Cho and J. R. Arthur, Prog. Solid State Chem. **10**, 157 (1975).

[9] P. M. Petroff and S. P. DenBaars, Superlattices and Microstruct **15**, 15 (1994).

[10] R. Nötzel, Semicond. Sci. Technol. **11**, 1365 (1996).

[11] D. Granados and J. M. García, Appl. Phys. Lett. **82**, 2401 (2003).

[12] Y. Ma, P. E. Kremer, and B. D. Gerardot, J. Appl. Phys. **115**, 023106 (2014).

[13] A. V. Kuhlmann *et al.*, Rev. Sci. Instrum. **84**, (2013).

[14] H. J. Kimble, Nature **453**, 1023 (2008).

[15] M. Atature, Science **312**, 551 (2006).

[16] B. D. Gerardot, Nature **451**, 441 (2008).

[17] D. Press and et al, Nature **456**, 218 (2008).

[18] A. N. Vamivakas *et al.*, Nature **467**, 297 (2010).

[19] J. R. Schaibley, *Spin-photon entanglement and quantum optics with single quantum dots*, PhD thesis, University of Michigan, 2013.

[20] R. C. Ashoori *et al.*, Phys. Rev. Lett. **71**, 613 (1993).

[21] T. Schmidt *et al.*, Phys. Rev. B **51**, 5570 (1995).

[22] S. Tarucha, D. G. Austing, T. Honda, R. J. van der Hage, and L. P. Kouwenhoven, Phys. Rev. Lett. **77**, 3613 (1996).

[23] B. T. Miller *et al.*, Phys. Rev. B **56**, 6764 (1997).

[24] R. J. Warburton *et al.*, Phys. Rev. B **58**, 16221 (1998).

[25] R. J. Warburton *et al.*, Nature **405**, 926 (2000).

[26] S. Seidl *et al.*, Phys. Rev. B **72**, 195339 (2005).

[27] B. Gerardot *et al.*, Appl. Phys. Lett. **99**, 243112 (2011).

[28] E. D. Kim *et al.*, Phys. Rev. Lett. **104**, 167401 (2010).

[29] A. S. Bracker *et al.*, Phys. Rev. Lett. **94**, 047402 (2005).

[30] D. A. B. Miller *et al.*, Phys. Rev. Lett. **53**, 2173 (1984).

[31] Y. Ma, G. Ballesteros, J. M. Zajac, J. Sun, and B. D. Gerardot, Opt. Lett. **40**, 2373.

[32] S. M. Mansfield, W. R. Studenmund, G. S. Kino, and K. Osato, Opt. Lett. **18**, 305 (1993).

[33] K. Koyama, M. Yoshita, M. Baba, T. Suemoto, and H. Akiyama, Appl. Phys. Lett. **75**, 1667 (1999).

[34] V. Zwiller and G. Bjork, J. Appl. Phys. **92**, 660 (2002).

[35] S. Moehl, H. Zhao, B. D. Don, S. Wachter, and H. Kalt, J. Appl. Phys. **93**, 6265 (2003).

[36] J. P. Hadden *et al.*, Appl. Phys. Lett. **97**, (2010).

[37] P. Siyushev *et al.*, Appl. Phys. Lett. **97**, 241902 (2010).

[38] R. Proux *et al.*, Phys. Rev. Lett. **114**, 067401 (2015).

[39] R. Patel *et al.*, Phys. Rev. Lett. **100**, 207405 (2008).

[40] Y. Tokura, W. G. van der Wiel, T. Obata, and S. Tarucha, Phys. Rev. Lett. **96**, 047202 (2006).

[41] J. M. Elzerman *et al.*, Nature **430**, 431 (2004).

[42] I. I. Rabi, J. R. Zacharias, S. Millman, and P. Kusch, Phys. Rev. **53**, 318 (1938).

[43] N. B. Manson, C. Wei, and J. P. D. Martin, Phys. Rev. Lett. **76**, 3943 (1996).

[44] B. R. Mollow, Phys. Rev. **188**, 1969 (1969).

[45] J. L. Carlsten, A. Szöke, and M. G. Raymer, Phys. Rev. A **15**, 1029 (1977).

[46] H. Kimble, M. Dagenais, and L. Mandel, Phys. Rev. Lett. **39**, 691 (1977).

[47] F. Arecchi and R. Bonifacio, IEEE Journal of Quantum Electronics **1**, 169 (1965).

[48] Y. Wu and X. Yang, Phys. Rev. Lett. **98**, 013601 (2007).

[49] G. Wrigge, *Coherent and Incoherent Light Scattering in the Resonance Fluorescence of a Single Molecule*, PhD thesis, ETH Zurich, 2008.

[50] M. L. Citron, H. R. Gray, C. W. Gabel, and C. R. Stroud, Phys. Rev. A **16**, 1507 (1977).

[51] K. Konthasinghe *et al.*, Phys. Rev. B **85**, 235315 (2012).

[52] H. S. Nguyen *et al.*, Appl. Phys. Lett. **99**, 261904 (2011).

[53] C. Matthiesen, A. N. Vamivakas, and M. Atatüre, Phys. Rev. Lett. **108**, 093602 (2012).

[54] Loudon, *The quantum theory of light.* (OUP, 2000., 2000).

[55] J. Houel *et al.*, Phys. Rev. Lett. **108**, 107401 (2012).

[56] A. V. Kuhlmann *et al.*, Nat. Phys. **9**, 570 (2013).

[57] C. Matthiesen, M. J. Stanley, M. Hugues, E. Clarke, and M. Atatüre, Sci. Rep. **4** (2014).

[58] J. H. Prechtel *et al.*, Phys. Rev. X **3**, 041006 (2013).

[59] J. Hansom, C. H. H. Schulte, C. Matthiesen, M. J. Stanley, and M. Atatüre, Appl. Phys. Lett. **105**, 172107 (2014).

[60] M. J. Stanley *et al.*, Phys. Rev. B **90**, 195305 (2014).

[61] H. Robinson and B. Goldberg, Phys. Rev. B **61**, R5086 (2000).

[62] A. Berthelot *et al.*, Nat. Phys. **2**, 759 (2006).

[63] O. Gazzano *et al.*, Nat. Commun. **4**, 1425 (2013).

[64] M. Hauck *et al.*, Phys. Rev. B **90**, 235306 (2014).

[65] Z. M. Wang, S. Seydmohamadi, J. Lee, and G. Salamo, Appl. Phys. Lett. **85**, 5031 (2004).

[66] A. Majumdar, E. D. Kim, and J. Vučković, Phys. Rev. B **84**, 195304 (2011).

[67] M. Davanço, C. S. Hellberg, S. Ates, A. Badolato, and K. Srinivasan, Phys. Rev. B **89**, 161303 (2014).

[68] H. S. Nguyen *et al.*, Phys. Rev. B **87**, 115305 (2013).

[69] C. Santori, D. Fattal, J. Vučković, G. S. Solomon, and Y. Yamamoto, Nature **419**, 594 (2002).

[70] K. H. Madsen *et al.*, Phys. Rev. B **90**, 155303 (2014).

[71] L. Monniello *et al.*, Phys. Rev. B **90**, 041303 (2014).

[72] A. V. Khaetskii, D. Loss, and L. Glazman, Phys. Rev. Lett. **88**, 186802 (2002).

[73] I. Merkulov, A. L. Efros, and M. Rosen, Phys. Rev. B **65**, 205309 (2002).

[74] B. Urbaszek *et al.*, Rev. Mod. Phys. **85**, 79 (2013).

[75] R. J. Warburton, Nat. Mater. **12**, 483 (2013).

[76] Z.-X. Gong, Z.-q. Yin, and L.-M. Duan, New J. Phys. **13**, 033036 (2011).

[77] R. N. E. Malein *et al.*, Screening nuclear field fluctuations in quantum dots for indistinguishable photon generation, Submitted, 2015.

[78] C. Latta *et al.*, Nat. Phys. **5**, 758 (2009).

[79] A. Högele *et al.*, Phys. Rev. Lett. **108**, 197403 (2012).

[80] X. Xu *et al.*, Nature **459**, 1105 (2009).

[81] B. Gerardot *et al.*, Appl. Phys. Lett. **90**, 221106 (2007).

[82] H. Paul, Rev. Mod. Phys. **54**, 1061 (1982).

[83] X. T. Zou and L. Mandel, Phys. Rev. A **41**, 475 (1990).

[84] P. Michler *et al.*, Science **290**, 2282 (2000).

[85] M. Eisaman, J. Fan, A. Migdall, and S. Polyakov, Rev. Sci. Instrum. **82**, 071101 (2011).

[86] P. Kok *et al.*, Rev. Mod. Phys. **79**, 135 (2007).

[87] J. L. O'Brien, A. Furusawa, and J. Vučković, Nat. Photonics **3**, 687 (2009).

[88] D. Fattal *et al.*, Phys. Rev. Lett. **92**, 037903 (2004).

[89] M. Pooley *et al.*, Appl. Phys. Lett. **100**, 211103 (2012).

[90] O. Gazzano *et al.*, Phys. Rev. Lett. **110**, 250501 (2013).

[91] C. K. Hong, Z. Y. Ou, and L. Mandel, Phys. Rev. Lett. **59**, 2044 (1987).

[92] A. Bennett, D. Unitt, A. Shields, P. Atkinson, and D. Ritchie, Opt. Express **13**, 7772 (2005).

[93] S. Laurent *et al.*, Appl. Phys. Lett. **87**, 163107 (2005).

[94] S. Ates *et al.*, Phys. Rev. Lett. **103**, 167402 (2009).

[95] C. Matthiesen *et al.*, Nat. Commun. **4**, 1600 (2013).

[96] Y. He *et al.*, Phys. Rev. Lett. **111**, 237403 (2013).

[97] S. Kalliakos *et al.*, Appl. Phys. Lett. **104**, 221109 (2014).

[98] J. Singh, *Physics of semiconductors and their heterostructures* (McGraw-Hill, New York, 1993).

[99] O. Gywat, H. Krenner, and J. Berezovsky, *Spin in optically active quantum dots: Concepts and methods* (Wiley-VCH, Weinheim, 2010).

[100] S. J. Prado, *Propriedades ópticas e magneto-ópticas em pontos quânticos esféricos e semi-esféricos*, PhD thesis, Departamento de física - Universidade Federal de São Carlos, 2003.

[101] J. J. Sakurai, *Modern quantum mechanics*, Revised ed. (Addison-Wesley Publishing Company, 1994).

[102] P. Fallahi, S. Yılmaz, and A. Imamoğlu, Phys. Rev. Lett. **105**, 257402 (2010).

[103] E. Chekhovich *et al.*, Phys. Rev. Lett. **104**, 066804 (2010).

[104] J. Fischer, W. Coish, D. Bulaev, and D. Loss, Phys. Rev. B **78**, 155329 (2008).

[105] M. Hennrich, A. Kuhn, and G. Rempe, Phys. Rev. Lett. **94**, 053604 (2005).

[106] F. Miftasani and P. Machnikowski, Photon-photon correlation statistics in the collective emission from ensembles of self-assembled quantum dots, arXiv:1407.4603v2, 2014.

[107] R. G. DeVoe and R. G. Brewer, Phys. Rev. Lett. **76**, 2049 (1996).

[108] R. Reimann *et al.*, Phys. Rev. Lett. **114**, 023601 (2015).

[109] U. Eichmann *et al.*, Phys. Rev. Lett. **70**, 2359 (1993).

[110] Z. Ficek and Tanaś, Phys. Rep. **372**, 369 (2002).

[111] Z. Ficek, R. Tanaś, and S. Kielich, Physica A **146**, 452 (1987).

[112] B. D. Gerardot *et al.*, Phys. Rev. Lett. **95**, 137403 (2005).

[113] G. Muñoz Matutano *et al.*, Phys. Rev. B **84**, 041308 (2011).

[114] M. Royo, J. I. Climente, and J. Planelles, Phys. Rev. B **84**, 235312 (2011).

[115] K. Jacobs and D. A. Steck, Contemp. Phys. **47**, 279 (2006).

[116] H. Morawitz, Phys. Rev. **187**, 1792 (1969).

[117] W. Lukosz and R. Kunz, JOSA **67**, 1607 (1977).

[118] H. Benisty, H. De Neve, and C. Weisbuch, Quantum Electronics, IEEE Journal of **34**, 1612 (1998).

[119] J. Eschner, C. Raab, F. Schmidt-Kaler, and R. Blatt, Nature **413**, 495 (2001).

[120] H. F. Arnoldus, D. Jelski, and T. F. George, J. Math. Phys. **28**, 1069 (1987).

[121] K. C. Liu and T. F. George, Phys. Rev. B **32**, 3622 (1985).

[122] C.-r. Fu and C.-d. Gong, Phys. Rev. A **40**, 207 (1989).

[123] S. M. Barnett, N. Harris, and J. J. Baumberg, PCCP **16**, 6544 (2014).

[124] C. M. Teodorescu, PCCP **17**, 21302 (2015).

[125] C. Ropp *et al.*, Nat. Commun. **6** (2015).

Appendices

Appendix A

Equipment list

Label	Company/Part number	Quick description
Laser 950 nm	Toptica/DL pro	Tunable diode laser
Laser controller	Toptica/DC 110	Diode laser supply and control rack
Wavemeter	HighFinesse/WS-U	Wavelength meter for high speed measurement of lasers
Laser 830 nm	Thorlabs/LPS-PM830-FC	Diode laser supported by compatibles temperature controller and current controller
ND filter	Thorlabs/NDC-100C-4M	Mounted continuously variable ND filter
$\lambda/4$	Thorlabs/AQWP10M-980	Mounted achromatic quarter-wave plate
$\lambda/2$	Thorlabs/AHWP10M-980	Mounted achromatic half-wave plate
Lens - 0.15NA	Thorlabs/C280TM-B	Mounted geltech aspheric lens
SMF	Font Canada/Unknown	Single-mode fibre with central wavelength equal to 980 nm
LP_1	Thorlabs/LPVIS050-MP2	Mounted linear polariser
TUGP	Unknown	Thick uncoated glass plate
PD	Thorlabs/SM1PD1A	Mounted silicon photodiode
Opt. window	Thorlabs/WG11050	Broadband precision window
Lens - 0.68NA	Thorlabs/C390TM-B	Mounted geltech aspheric lens
SIL	Unknown	2 mm diameter solid immersion lens
XY scanner	Attocube/ANSxy100	Compact open loop xy-scanner
X-motor	Attocube/ANPx100	Nano drive to move the sample horizontally
Y-motor	Attocube/ANPx100	Nano drive to move the sample horizontally
Z-motor	Attocube/ANPz100	Nano drive to move the sample vertically
Microscope tube	Attocube/Unknown	Customized vacuum tube for attocube microscope
Cryostat	Attocube/AttoDry1000	cryogen-free cryostat with superconducting magnets
CCD	Watec/WAT 120N	Monochrome camera
LP_2	Laser physics/COD-CUST-950	Customised ultra high extinction ratio polariser for use at 950 nm

FFC	Thorlabs/ADAFC3	FC/APC to FC/APC Mating Sleeve
FPI	Micron optics/FFP-SI	Fibre Fabry-Perot Tunable Filter
SPAD	Excelitas/SPCM-900-14-FC	Single Photon Counting Modules
NI Box	NI/782251-01	Data Acquisition Device
$g^2(\tau)$	HWU-QPL	[Fig. 2.10]
HOM	HWU-QPL	[Fig. 2.11]
PicoHarp	PicoQuant/PicoHarp 300	Stand-alone TCSPC Module
Spectrometer	Princeton instruments/unknown	Spectrograph
MFPC	Thorlabs/FPC560	Manual fibre polarisation controller

Appendix B

Temporal evolution of the X^{1-} excited states

By replacing the off diagonal elements [Eqs. 4.50-4.53] in [Eqs. 4.41-4.42], the temporal evolution of the excited states are

$$\begin{aligned}
\rho_{\Downarrow\Downarrow}(t) &= \frac{\Omega^2\rho_{+-}(0)\sin(\theta)}{2(B^2+\Gamma^2)}\left[\frac{-BE_{+\Downarrow}+\Gamma^2}{E_{+\Downarrow}^2+\Gamma^2}+\frac{BE_{-\Downarrow}+\Gamma^2}{E_{-\Downarrow}^2+\Gamma^2}\right]\left[e^{-\Gamma t}-\cos(Bt)\right] \\
&+ \frac{\Gamma\Omega^2\rho_{+-}(0)\sin(\theta)}{2(B^2+\Gamma^2)}\left[\frac{E_{-\Downarrow}-B}{E_{-\Downarrow}^2+\Gamma^2}-\frac{E_{+\Downarrow}+B}{E_{+\Downarrow}^2+\Gamma^2}\right]\sin(Bt) \\
&+ \frac{(E_{+\Downarrow}E_{-\Downarrow}+\Gamma^2)\Omega^2\rho_{+-}(0)\sin(\theta)}{(E_{+\Downarrow}^2+\Gamma^2)(E_{-\Downarrow}^2+\Gamma^2)}\left\{-2e^{-\Gamma t}+e^{-\Gamma t/2}\left[\cos\left(\frac{E_{+\Downarrow}t}{2}\right)+\cos\left(\frac{E_{-\Downarrow}t}{2}\right)\right]\right\} \\
&+ \frac{(E_{+\Downarrow}-E_{-\Downarrow})\Gamma\Omega^2\rho_{+-}(0)\sin(\theta)e^{-\Gamma t/2}}{(E_{+\Downarrow}^2+\Gamma^2)(E_{-\Downarrow}^2+\Gamma^2)}\left[\sin\left(\frac{E_{+\Downarrow}t}{2}\right)-\sin\left(\frac{E_{-\Downarrow}t}{2}\right)\right] \\
&- 2\Omega^2\left[\frac{\rho_{++}(0)\sin^2\left(\frac{\theta}{2}\right)}{E_{+\Downarrow}^2+\Gamma^2}\cos\left(\frac{E_{+\Downarrow}t}{2}\right)+\frac{\rho_{--}(0)\cos^2\left(\frac{\theta}{2}\right)}{E_{-\Downarrow}^2+\Gamma^2}\cos\left(\frac{E_{-\Downarrow}t}{2}\right)\right]e^{-\Gamma t/2} \\
&+ \left[\frac{\Omega^2\rho_{++}(0)\sin^2\left(\frac{\theta}{2}\right)}{E_{+\Downarrow}^2+\Gamma^2}+\frac{\Omega^2\rho_{--}(0)\cos^2\left(\frac{\theta}{2}\right)}{(E_{-\Downarrow}^2+\Gamma^2)}\right]\left(1+e^{-\Gamma t}\right) \qquad \text{(B.1)}
\end{aligned}$$

and

$$\begin{aligned}
\rho_{\Uparrow\Uparrow} &= \frac{\Omega^2\rho_{+-}(0)\sin(\theta)}{2(B^2+\Gamma^2)}\left[\frac{BE_{+\Uparrow}-\Gamma^2}{E_{+\Uparrow}^2+\Gamma^2}-\frac{BE_{-\Uparrow}+\Gamma^2}{E_{-\Uparrow}^2+\Gamma^2}\right]\left[e^{-\Gamma t}-\cos(Bt)\right] \\
&+ \frac{\Gamma\Omega^2\rho_{+-}(0)\sin(\theta)}{2(B^2+\Gamma^2)}\left[\frac{B+E_{+\Uparrow}}{E_{+\Uparrow}^2+\Gamma^2}+\frac{B-E_{-\Uparrow}}{E_{-\Uparrow}^2+\Gamma^2}\right]\sin(Bt) \\
&+ \frac{(E_{+\Uparrow}E_{-\Uparrow}+\Gamma^2)\Omega^2\rho_{+-}(0)\sin(\theta)}{(E_{+\Uparrow}^2+\Gamma^2)(E_{-\Uparrow}^2+\Gamma^2)}\left\{2e^{-\Gamma t}-e^{-\Gamma t/2}\left[\cos\left(\frac{E_{+\Uparrow}t}{2}\right)+\cos\left(\frac{E_{-\Uparrow}t}{2}\right)\right]\right\} \\
&+ \frac{(E_{+\Uparrow}-E_{-\Uparrow})\Gamma\Omega^2\rho_{+-}(0)\sin(\theta)}{(E_{+\Uparrow}^2+\Gamma^2)(E_{-\Uparrow}^2+\Gamma^2)}e^{-\Gamma t/2}\left[\sin\left(\frac{E_{-\Uparrow}t}{2}\right)-\sin\left(\frac{E_{+\Uparrow}t}{2}\right)\right] \\
&- 2\Omega^2\left[\frac{\rho_{++}(0)\cos^2\left(\frac{\theta}{2}\right)}{E_{+\Uparrow}^2+\Gamma^2}\cos\left(\frac{E_{+\Uparrow}t}{2}\right)+\frac{\rho_{--}(0)\sin^2\left(\frac{\theta}{2}\right)}{E_{-\Uparrow}^2+\Gamma^2}\cos\left(\frac{E_{-\Uparrow}t}{2}\right)\right]e^{-\Gamma t/2} \\
&+ \left[\frac{\Omega^2\rho_{++}(0)\cos^2\left(\frac{\theta}{2}\right)}{E_{+\Uparrow}^2+\Gamma^2}+\frac{\Omega^2\rho_{--}(0)\sin^2\left(\frac{\theta}{2}\right)}{E_{-\Uparrow}^2+\Gamma^2}\right]\left(1+e^{-\Gamma t}\right). \qquad \text{(B.2)}
\end{aligned}$$